University of Alberta

Investigation of the relationship between the electron work function (EWF), adhesion and friction

by

Yanping Li

A thesis submitted to the Faculty of Graduate Studies and Research
in partial fulfillment of the requirements for the degree of

Doctor of Philosophy

in

Materials Engineering

Department of Chemical and Materials Engineering

Edmonton, Alberta
Spring 2008

Library and Archives Canada

Published Heritage Branch

395 Wellington Street
Ottawa ON K1A 0N4
Canada

Bibliothèque et Archives Canada

Direction du Patrimoine de l'édition

395, rue Wellington
Ottawa ON K1A 0N4
Canada

Your file Votre référence
ISBN: 978-0-494-45554-8
Our file Notre référence
ISBN: 978-0-494-45554-8

NOTICE:
The author has granted a non-exclusive license allowing Library and Archives Canada to reproduce, publish, archive, preserve, conserve, communicate to the public by telecommunication or on the Internet, loan, distribute and sell theses worldwide, for commercial or non-commercial purposes, in microform, paper, electronic and/or any other formats.

The author retains copyright ownership and moral rights in this thesis. Neither the thesis nor substantial extracts from it may be printed or otherwise reproduced without the author's permission.

AVIS:
L'auteur a accordé une licence non exclusive permettant à la Bibliothèque et Archives Canada de reproduire, publier, archiver, sauvegarder, conserver, transmettre au public par télécommunication ou par l'Internet, prêter, distribuer et vendre des thèses partout dans le monde, à des fins commerciales ou autres, sur support microforme, papier, électronique et/ou autres formats.

L'auteur conserve la propriété du droit d'auteur et des droits moraux qui protège cette thèse. Ni la thèse ni des extraits substantiels de celle-ci ne doivent être imprimés ou autrement reproduits sans son autorisation.

In compliance with the Canadian Privacy Act some supporting forms may have been removed from this thesis.

While these forms may be included in the document page count, their removal does not represent any loss of content from the thesis.

Conformément à la loi canadienne sur la protection de la vie privée, quelques formulaires secondaires ont été enlevés de cette thèse.

Bien que ces formulaires aient inclus dans la pagination, il n'y aura aucun contenu manquant.

Canada

Abstract

Adhesion and friction are of great theoretical interest and huge practical significance. The mechanisms of adhesion and friction are still subjects under investigation. Under light loads, friction is mainly dependent on the adhesion between two surfaces in contact, which is largely determined by the surface electron behavior. Electron work function (EWF) is a fundamental property of metals which characterizes their electron behavior and can be determined experimentally using a Kelvin probe.

In this study, attempts were made to establish relationships among EWF, adhesion and friction. For metal-ceramic contact, higher EWF corresponds to lower adhesive force and thus lower friction when measured under light loads using the AFM/LFM. Under higher loads involving plastic deformation, the friction of a target metal is mainly determined by its mechanical behavior. For metal-metal contact (mainly elastic contact) under light loads, an energy consumption friction (ECF) model was proposed to calculate friction coefficient. This model assumes elastic contact between two metals in contact and the calculation includes adhesion energy and deformation energy when the two metals slide on each other. Friction coefficient

is thus expressed as a function of EWF and mechanical properties of the metals. Further study has established a correlation between EWF and elastic behavior which makes it possible to predict adhesion and elastic-contact friction mainly based on the EWF. Such a relationship between material's property and performance is important for materials selection and optimization of nano/micro devices.

Dedicated to my parents and
my husband who have provided me with support and love at all times

&

To my son

Acknowledgements

I especially want to thank my supervisor, Professor Dongyang Li. His guidance, insightful criticisms, and patient encouragement aided my research and the writing of this thesis in innumerable ways.

I would like to thank the Professors who were in my committee and made helpful comments on my thesis.

I would like to thank my colleagues at the surface/tribology group with whom I had the pleasure of working over the years.

Financial support provided to this project by the Alberta Science and Research Authority (ASRA) and the Natural Science and Engineering Research Council of Canada (NSERC) is gratefully acknowledged.

Table of Contents

Chapter 1 : Introduction **1**

1.1 Importance of friction and adhesion 1

1.2 Motivation 4

1.3 Objectives 5

1.4 Overview of the thesis 6

Chapter 2 : Literature Review **9**

2.1 Surface 9

2.1.1 Surface topography and structure 9

2.1.2 Contact area 13

2.2 Theories of friction 17

2.3 Research of Friction and Adhesion 22

2.3.1 Research at macroscopic scale 22

2.3.2 Research at microscopic to atomic scale 28

2.4 Electron work function (EWF) 33

2.4.1 Definition 33

2.4.2 Measurements 35

2.4.3 Theoretical Analysis 43

2.4.4 Correlation with other properties 45

2.4.5 Application of EWF 57

Chapter 3 : Metal-Ceramic contact: adhesion and friction between 3d transition metals and ceramics **68**

3.1 Introduction and objective 69

3.2 Experimental Procedure 73

3.2.1 Samples preparation 73

3.2.2 EWF measurement 74

3.2.3 Adhesion and light-loaded friction measurement 75

3.2.4 Friction under higher loads 78
3.2.5 Hardness measurement 79
3.3 Results and discussion 81
3.3.1 Electron work function 81
3.3.2 Adhesion measurement using AFM 82
3.3.3 Friction measurement using AFM/LFM 85
3.3.4 Friction behavior under larger loads 87
3.4 Summary 90
Chapter 4 : Metal-Metal contact: adhesion and friction between 3d transition metals 91
4.1 Introduction and objective 91
4.2 Friction measurement 94
4.2.1 Samples preparation 94
4.2.2 Friction measurement 95
4.3 Results and Discussion 97
4.3.1 Friction measurement under light loads 97
4.3.2 Theoretical consideration 100
4.3.3 Further discussion 104
4.4 Summary 107
Chapter 5 : An energy consumption model for metal-metal adhesion and friction 109
5.1 Introduction and objective 109
5.2 Experimental procedure 111
5.3 Experimental observations 113
5.4 An energy consumption model 114
5.4.1 Concept 114
5.4.2 Adhesion energy 117
5.4.3 Elastic strain energy 125

5.5 Theoretical prediction of friction under light loads 130
5.6 Conclusions 132
Chapter 6 : Prediction of light-load friction solely based on EWF 133
6.1 Introduction and objective 133
6.2 Relationship between EWF and mechanical properties 134
6.3 Further discussion 142
6.4 Conclusions 144
Chapter 7 : Conclusions and future studies 145
7.1 Conclusions 146
7.2 Future studies 148
7.2.1. Using improved contact model 148
7.2.2 More fundamental studies 149
7.2.3 The dependence of friction coefficient on load 149
References 151

List of Tables

Table 2.1 Typical average roughness values of engineering surfaces 12

Table 2.2 Compatibility Parameter C_m of Clean Metals 25

Table 2.3 EWFs (eV)(bottom row) and Ionization energies (eV)(upper row) of polycrystalline specimens 47

Table 2.4 Interface barriers and work function of metals at large separation 48

Table 2.5 EWF and adhesion force of single crystal copper with different crystallographic planes 53

Table 3.1 Composition of the metals 73

Table 3.2 Annealing Temperature 73

Table 3.3 Surface roughness 86

Table 5.1 Numbers of neighbors of a bulk (N) and a surface atom (N-M) on a (100) plane of typical metallic lattices (BCC,FCC and Simple Cubic) 122

List of Figures

Figure 1.1 (a) A polysilicon micromotor. (b) A magnetically driven micromotor. The rotor diameter is 150μm, and the gears have diameters of 77, 100, and 150 μm [4]. 3
Figure 1.2 (a) Stiction of a microcantilever to the substrate. (b) adhesion between the fingers of a comb structure in a micromachined accelerometer [7]. 3

Figure 2.1 Profiles of three different mild steel surfaces, prepared by (a) Surface grinding only, (b) Surface grinding and lightly polishing, (c) Surface grinding and then light abrasion [4]. 10
Figure 2.2 AFM topography of a Mn Surface after fine polishing. 11
Figure 2.3 Schematic representation of the surface layer composition of a metal surface [3]. 13
Figure 2.4 a) Hertzian contact, b) JKR contact, c) DMT contact [20,23]. 15
Figure 2.5 Asperity deformation mode and plasticity factor of aluminium surfaces with different roughness values [2]. 17
Figure 2.6 Model for the deformation component of friction. α is the semi-angle of a rigid conical asperity which indents and slides through the surface of a plastically deforming material [2]. 21
Figure 2.7 Friction coefficients measured in vacuum as a function of d-bond character of the metals. (a) Metals in contact with themselves. (b) Metals in contact with single-crystal SiC [11]. 23
Figure 2.8 Friction coefficients for clean similar metals. Except for hexagonal latticed metals, the friction coefficient and the W_a/p ratio increase together [13]. 24

Figure 2.9 Friction coefficient of 3d transition metals in contact with copper [12]. 26
Figure 2.10 Schematic of a cross section through the cylindrical UHV chamber housing the UHV tribometer [37]. 27
Figure 2.11 Adhesive energy versus separation for interfaces between Al, Zn, Mg and Na [57]. 30
Figure 2.12 Atomic configurations predicted by theoretical modeling of the contact between a nickel tip and an initially plane gold surface. It shows adhesion of gold atoms to the nickel tip as the tip is raised from the surface [18]. 32
Figure 2.13 The original apparatus used by Lord Kelvin [84]. 36
Figure 2.14 Energy diagrams for electrons in two metal plates (M_1 and M_2) separated by a small vacuum gap, E_{F_1} and E_{F_2} are the Fermi energy levels, E_{vac} is the surface potential barrier, (a) metal plates are isolated, and (b) plates are connected electrically and charged [79]. 38
Figure 2.15 Scanning Kelvin probe arrangement [84]. 40
Figure 2.16 (a) Topography measurement in tapping mode. (b) Surface potential measurement in lift mode [86]. 41
Figure 2.17 The calculated work function for the 3d, 4d and 5d series metals compared to available experimental polycrystalline data (open circles), and single-surface data (solid circles). All calculations are performed at the most close-packed surface of the experimentally observed crystal structure. The solid line connecting the theoretical values is a guide to the eye [81,89]. 43
Figure 2.18 Plots of work function, first ionization potential, and standard electrode potential versus atomic number [87]. 46

Figure 2.19 Correlations between ν (110, $1\bar{1}0$) and ν (110, 001) of B.C.C metals and the polycrystalline work functions. The unfilled squares denote ν (110, $1\bar{1}0$) and filled diamonds for ν (110, 001) [94]. 49

Figure 2.20 Correlations between ν (110, $1\bar{1}0$) and ν (110, 001) and polycrystalline work function for F.C.C. phases of the non-ferromagnetic elemental metals. The lines are least-squares fits to the experimental results. The unfilled squares denote ν (110, $1\bar{1}0$) and filled diamonds for ν (110, 001) [94]. 50

Figure 2.21 (a) Solid electrolyte cell consisting of a YSZ disk with working (Pt), reference (Au, Ag) and counter electrodes (Au). 56
(b)Electrochemical reactor with two Kelvin probes [106].

Figure 2.22 Kelvin probe combined with friction testing machine [120]. 58

Figure 2.23 EWF, torque and surface temperature vs. normal load curves for the surface of a bronze sample [74]. 60

Figure 2.24 Example of power metallurgy material optimization (tin content) [74]. 61

Figure 2.25 Example of powder metallurgy material optimization (porosity) [74]. 61

Figure 2.26 Surface height and surface potential maps of wear regions on a single crystal aluminum sample at 1μN. Included are cross-section analyses for each map [86]. 63

Figure 2.27 Comparison of the sensitivities of the three methods to wear: weight loss measurement, morphological variation, and the EWF measurement [111]. 64

Figure 2.28 EWF of yttrium(Y)-free and yttrium (Y)-containing 304 stainless steel after passivation treatment in a 35% HNO_3 solution for 12 h [117]. 65
Figure 2.29 Variations in the EWF of copper with respect to elastic and plastic deformations [124]. 66
Figure 2.30 Results of simultaneous measurements of the regular stress-strain diagram and the EWF for medium carbon steel [113]. 67

Figure 3.1 Distortion of cantilever measured by laser beam deflection technique in AFM. 76
Figure 3.2 The curve of deflection versus displacement (Z) of cantilever when the AFM tip is approaching and leaving a sample surface. A recorded deflection vs. Z curve is also presented in the same figure. 76
Figure 3.3 Friction trace and retrace, determined by AFM. 77
Figure 3.4 CETR universal micro-tribometer (UMT) system. 79
Figure 3.5 A typical load-depth curve from micro-hardness test [137]. 80
Figure 3.6 Electron work function of 3d transition metals [127]. 82
Figure 3.7 Adhesion force between 3d transition metals and a Si_3N_4 tip in AFM [127]. 84
Figure 3.8 Friction of 3d transition metals under a light load 86
Figure 3.9 Friction coefficient of 3d transition metals under 1 mN load [127]. 89
Figure 3.10 Micro-hardness of 3d transition metals [127]. 89

Figure 4.1 Contact phenomena of two metal plates (a) Fermi energies are different before equilibrium (b) Fermi energies are equal after equilibrium [74]. 93

Figure 4.2 Schematic illustration of the friction apparatus. The iron plate was glued to the sample holder [151]. 96
Figure 4.3 Friction coefficient of Fe-Fe pairs (polished) measured with and without pre-rubbing, respectively [151]. 98
Figure 4.4 Friction coefficients of 3d transition metals in contact with iron (under 30 mN) [147]. 99
Figure 4.5 EWFs of 3d transition metals from ref.95 (Miedema's data) [95]. 100
Figure 4.6 Surface energy calculated using equation (4.1). 101
Figure 4.7 Adhesion energy for 3d transition metals in contact with Fe calculated using equations (4.1) to (4.5). 103

Figure 5.1 Experimentally measured friction coefficients of 3d transition metals in contact with Zn under 1mN. 114
Figure 5.2 Schematic diagram for the density of states (D(E)) of a transition metal [162]. 120
Figure 5.3 Paths contributes to the second moment of a two-dimensional simple cubic crystal [162]. 122
Figure 5.4 Surface energy calculated using equations (5.7)-(5.12). 123
Figure 5.5 Adhesion energies for metals in contact with Zn, calculated using equations (5.6)-(5.15) [151]. 125
Figure 5.6 (a) Contours represent constant values of one of the two principle stresses in xz-plane.(b) Contours represent constant values of one of the two principle stresses in xz-plane. (c) Contours of principle stresses in Y-direction [167]. 129
Figure 5.7 Calculated friction coefficients of 3d transition metals in contact with Zn using the proposed ECF model. Contact condition: a

semi-spherical ball with its radius equal to 4 mm slid on a flat counter-face under a light load of 0.1 mN [151]. 131

Figure 6.1 The EWF [127]and bulk modulus [168] of 3d transition metals. 137

Figure 6.2 Friction coefficients of 3d transition metals in contact with Zn under 1mN [151]. Nominal contact area is 4×4 mm^2. 139

Figure 6.3 Calculated friction coefficients of 3d transition metals in contact with Zn using the proposed ECF model described in Chapter 5 with EWF as the main parameter. Contact condition: a semi-spherical ball with its radius equal to 4 mm slid on a flat counter-face under a light load of 0.1 mN. 141

List of Symbols

a	Radius of the contact area
A	Interface area
A_r	Real contact area
b	Lattice parameter
B	Bulk modulus
C_M	Compatibility coefficient
d	Diameter of contact area
$D(E)$	Density of states
d_{ac}	Vibration amplitude
E	Young's modulus
E^*	Reduced Young's modulus
E_C	Cohesive energy per atom
E_F	Fermi energy
E^M	Electrode potential
F	Friction force
H	Hardness
I	Current flow onto and off the probe of Kelvin probe
K	Displacement along the direction of normal contact force
L	Normal load
l	Distance between two metals at atomic level
l'	Distance between the probe and the surface
n	Second moment of density of states of a bulk atom
N	Number of nearest neighbors of a bulk atom
n'	Second moment of density of states of a Surface atom
n^*	Second moment of density of states of an interface atom
$N-M$	Number of nearest neighbors of a surface atom

N_S	Number of surface atoms
n_{ws}	Electron density at the boundary of Wigner-Seitz cell
R	Radius of asperity
R_a	Average roughness
r	Interatomic separation
r_s	Electron density parameter
S	Total sliding distance, Overall length of the profile under examination
s	Shear strength
U_{CPD}	Contact potential difference
U_{O_2}	Absolute electrode potential
U_{WR}	Potential difference between the working and reference electrodes
V_P	DC bias potential applied to the probe
V_S	Potential of the surface
W	Surface potential barrier
W_a	Adhesion energy
W_e	Elastic strain energy per unit area
W_{EV}	Elastic strain energy per unit volume
x	Depth of penetration, Distance from the origin
Y	Yield stress
y	Height of the surface above the mean line
Z	Number of valence electron
α	Semi-angle of a rigid conical asperity
α^*	Scalling factor
β	Hopping integrals between first nearest bulk neighbors
β'	Hopping integrals between interface atoms

γ_{12}	Interfacial energy
γ_i	Surface energy
∇n	Difference in the second moment between an interfacial atom and a bulk atom
ε	Elastic Strain
ε'	Dielectic constant
ε^*	Interatomic spacing
λ	Tabor number
μ	Friction coefficient
ν	Poisson's ratio
σ	Stress
σ^*	Standard deviation of the distribution of asperity heights
ϕ	Sum of nearest-neighbor central force interaction
φ	Electron work function
ψ	Plastic index
$\sum E_g^{AV}$	Average energy gap
$\bar{n}$	Average valence electron density in the bulk

List of Abbreviations

AFM	Atomic force microscope
ECF	Energy consumption friction
EWF	Electron work function
FFM	Friction force microscope
LEED	Low energy electron diffraction
MD	Molecular dynamics
MEMS	Microelectromechanical systems
RMS	Root mean square
SKP	Scanning Kelvin probe
TBA	Tight binding approximation
UHV	Ultrahigh vacuum

Chapter 1 : Introduction

The present chapter provides introduction of the importance of adhesion and friction. The motivation and objective of this study are also discussed. In the end, the structure of this thesis is described to give an overview of the thesis.

1.1 Importance of friction and adhesion

Friction is the resistance encountered by a solid object when it moves tangentially with respect to the surface of another contacting object, or when an attempt is made to produce such motion. The movement could be sliding, rolling or rubbing [1,2]. Friction is inevitably associated with almost all mechanical systems and is important to our daily life. In some cases, friction may be desirable such as brakes and belt drives. In other cases, friction may be deleterious such as bearings and gears [1-3]. It has been estimated that in the United States 10% of oil consumption is used simply to overcome friction, and friction takes away 6% of the gross national product, that is around $420 billion per year. In this work, discussion would be limited to kinetic (dynamic) sliding friction between two solids [1,4].

When two solid surfaces are brought into contact, adhesion or bonding across the interface may occur. When two solids approach one another they experience attractive forces, i.e. long-range van der Waals forces followed by short-range forces [5]. Short-range forces come form various interfacial bonds, such as ionic, covalent, metallic, hydrogen bonds. These short-range forces are largely determined by the surface electronic configuration and behavior [6].

Nano/micro devices (Fig. 1.1[4]) have large surface-to-volume ratio because of the small dimensions. This makes strong adhesion induced by surface effects dictate the dynamic behavior of the system[7]. The components used in micro/nanostructures and some biological systems [8] are light and operate under very light loads [9]. As a result, friction between lightly loaded micro/nano components is largely dominated by adhesion and mechanical plowing becomes less important [8,9].

Magnetic storage devices and microelectromechanical systems (MEMS) are two examples where the adhesion between the surfaces would strongly affect their performances [9]. Fig. 1.2 illustrates two examples of adhesion in MEMS [7].

Adhesion and friction are major problems limiting both the fabrication output and operation lifetime of many MEMS devices, e.g. electromechanical switchers fail because of the permanent adhesion

of their moving components [7,8]. In some cases, adhesion is beneficial e.g. thin films used as protective coatings, the manufacturing of multilayered wafer structure, or in bio-films for orthopedic implants [7-9].

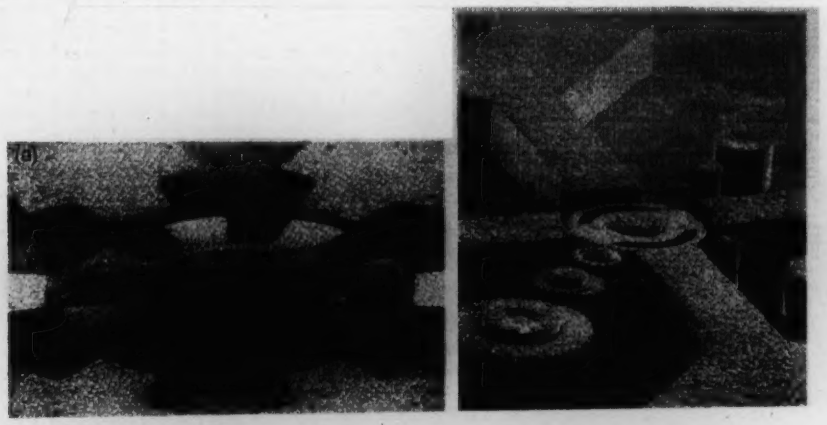

Figure 1.1 (a) A polysilicon micromotor. (b) A magnetically driven micromotor. The rotor diameter is 150μm, and the gears have diameters of 77, 100, and 150 μm [4].

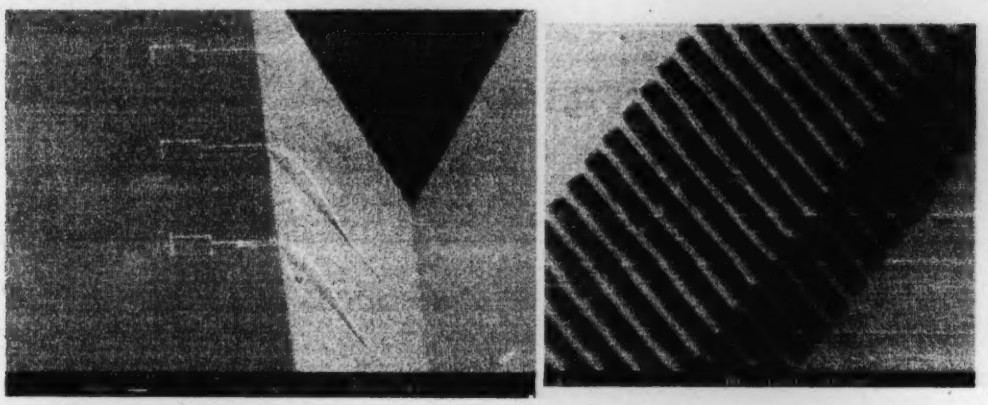

Figure 1.2 (a) Stiction of a microcantilever to the substrate. (b) adhesion between the fingers of a comb structure in a micromachined accelerometer [7].

1.2 Motivation

Adhesion and friction play significant roles in industrial processes and our daily life [1]. Sliding friction is one of the oldest problems in physics and certainly one of the most important from practical perspective [4]. Adhesion could be particularly important for nano/micro devices because of the smooth contact area and light-loaded condition [9]. With the rapid advance in nanotechnology, adhesion and adhesive friction have become important issues.

Friction has been studied and debated for several hundred years [4,9,10]. The laws of friction provides useful summaries of empirical observations [2]. Considerable experimental and theoretical studies have been conducted to understand the mechanisms responsible for adhesion and friction. Many researches studied adhesion and friction at macroscopic scale and tried to correlate experimental data to various materials properties such as chemical reactivity, metallurgical compatibility, crystal structure, d-valence bond character, etc [1,11-13]. The development of new experimental techniques especially AFM (atomic force microscope) and FFM (friction force microscope) made it possible to study adhesion and friction at microscopic to atomic scale. At the same

time, computer simulation and analytical studies of model system have resulted in a better understanding of the fundamental atomistic origin of friction [14,15].

These numerous efforts shed light on the origins of adhesion and friction. However, the fundamental mechanisms involved have not yet been fully clarified. Adhesion and friction are still intriguing areas which attract the interests of many researches.

An easy to use but fundamental model for quantitative prediction of adhesion and friction under light loads is demanded to support the development of nano/micro devices or machines. In order to develop such a model, it is important to establish the correlation between fundamental material properties and tribological behavior of materials.

1.3 Objectives

My dissertation research is focused on studies of adhesion and friction from a fundamental yet practical point of view. The purposes of the study were to (1) identify the relationship, if any, between fundamental material properties and adhesion as well as friction under light loads; (2) develop a simple but fundamental model for quantitative prediction of adhesion and friction under light loads,

which will be beneficial to design and optimization of nano/micro devices or machines.

Since intrinsic adhesion comes from short-range forces which are largely dependent on the surface electronic behavior, the electron work function (EWF) is chosen as a fundamental material property to predict adhesion and friction. EWF is the minimum energy required for an electron to escape from the Fermi level to a point just outside the bulk metal. It is one of fundamental electronic properties of a metallic surface and can be used to characterize electron behavior of metals [16]. In addition, EWF can be measured easily using a Kelvin probe.

3d-transition metals were chosen as sample materials for this study because they are basic metallic elements for a wide range of industrial alloys.

1.4 Overview of the thesis

There are seven chapters contained in this thesis.

Chapter 2 provides a review of the research done worldwide on adhesion, friction and related issues. Literature review of EWF regarding its definition, measurements, theoretical analysis, correlation with other material's properties and applications is also included in this chapter.

The rest of this thesis reports the experimental results and theoretical analysis of light load adhesion and friction of 3d-transition metals.

Chapter 3 presents the study of adhesion and friction between ceramic and metal. The adhesion and friction under light loads between a silicon nitride tip and 3d transition metal were first studied using AFM/LFM (lateral force microscope). Friction of the samples with a sharp tip under higher loads was also measured using a microtribometer to get a better understanding of the frictional behavior of the transition metals.

Chapter 4 presents studies on metal-metal adhesion and friction under light loads. Due to the difficulty in direct determination of adhesion between the metals, friction under a light contact force was used as a parameter to evaluate the adhesion behavior, which is acceptable as the contact load is light. A semi-empirical theory was used to calculate the adhesion energy between two metals, which is expressed as a function of EWF.

Chapter 5 reconsiders metal-metal adhesion and friction under light load from energy balance perspective. An energy consumption friction (ECF) model was proposed to calculate friction coefficients of different metals in contact. This model assumes elastic contact between two metals and the calculation includes adhesion energy

and deformation energy when two metals slide on each other. In this model, the adhesion energy between two contacting metals is also calculated based on more concrete physical concepts.

Chapter 6 describes the study of the relationship between EWF and elastic properties of metals. Such a correlation could make it possible to predict adhesion and elastic-contact friction mainly based on the EWF.

Chapter 7 presents a summary of conclusions and areas for future research.

Chapter 2 : Literature Review

The present chapter provides a review of the literature regarding solid surfaces, adhesion, friction, and EWF. The purpose is to provide a comprehensive overview of the current studies conducted worldwide on adhesion, friction and related areas. Chapter two comprises four sections: the first section presents general concepts of solid surface and contact area between two surfaces; the second section describes the general theories of friction; the third section provides a review on research of adhesion and friction; the fourth section deals with EWF including its definition, measurement techniques, theoretical calculation, correlation with other properties and applications in tribological study.

2.1 Surface

Friction and adhesion are surface phenomena so it is important to understand surfaces of solids.

2.1.1 Surface topography and structure

Most surfaces are rough on a microscopic scale [2-4,11]. The surface topography is determined by surface preparation process and materials properties [2].

Surface topography may be assessed by several different techniques [2,4]. The stylus profilometer is one of the most widely used instruments, which employs a stylus that moves across the surface under examination. The vertical movements of the stylus are amplified electrically. Fig. 2.1 shows the surface topographies of steel after three different kinds of surface treatments. Optical interferometry is a non-contacting optical method for surface roughness measurement, during which surface profiles can be determined without generating distortion or damage to the surface. However, this technique is not suitable for examining coarse surface [2,4].

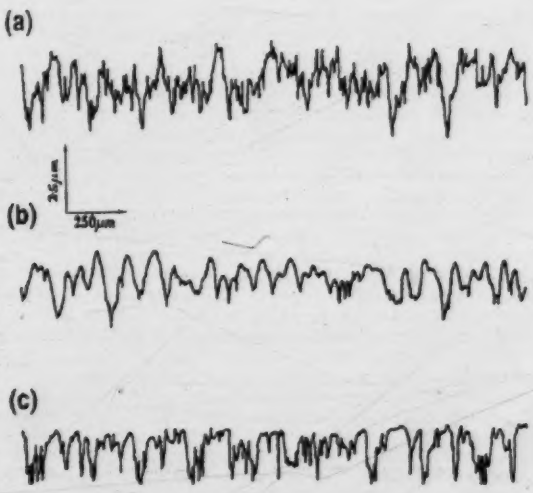

Figure 2.1 Profiles of three different mild steel surfaces, prepared by (a) Surface grinding only, (b) Surface grinding and lightly polishing, (c) Surface grinding and then light abrasion [4].

Scanning tunneling microscopy (STM) and (AFM) allow studies of surfaces on an atomic level. Fig. 2.2 shows an AFM image of a Mn sample after fine polishing using slurry containing aluminum oxide powder of 0.05 μm.

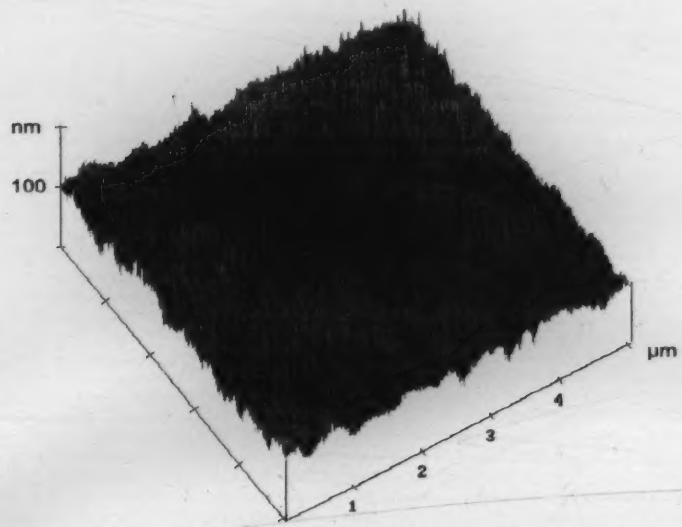

Figure 2.2 AFM topography of a Mn Surface after fine polishing.

The roughness of engineering surfaces are usually specified by average roughness (R_a) values, which is defined by

$$R_a = \frac{1}{S}\int_0^S |\, y(x)\,|\, dx \qquad \textbf{(2.1)}$$

Where y is the height of the surface above the mean line at a distance x from the origin, and S is the overall length of the profile

under examination [2,17,18]. Table 2.1 lists typical ranges of R_a values for engineering surfaces.

Table 2.1 Typical average roughness values of engineering surfaces [2]

	R_a (μm)
Planing, shaping	1-25
Milling	1-6
Drawing, extrusion	1-3
Turning, boring	0.4-6
Grinding	0.1-2
Honing	0.1-1
Polishing	0.1-0.4
Lapping	0.05-0.4

Surfaces of metals represent an abrupt termination of the periodicity of the crystalline lattice. A metal surface is very reactive because of the broken bonds on the surface [3,11,19]. The composition of a surface varies, depending on the properties of the material, preparation and the environment [3,4,11,19]. Generally speaking, a metal surface is covered by several layers including contaminant, adsorbed gas, oxide and work-hardened layers. Fig. 2.3 illustrates these surface films on a metal surface.

The main constitutes of the adsorbed layer are water and oxygen molecules, which may have condensed and become physically adsorbed to the solid surface. Contaminant layer is usually grease or oil films [3,4,11,13].

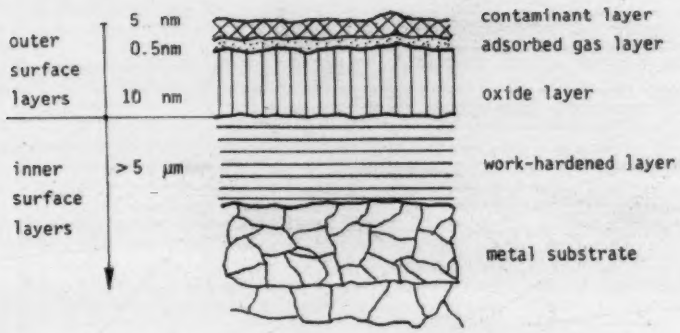

Figure 2.3 Schematic representation of the surface layer composition of a metal surface [3].

2.1.2 Contact area

Intimate contact occurs only at locations where the asperities on one surface touch the other. Strong adhesion only takes place in these regions [3,4,11,19]. So the area of real contact is an important factor in determining adhesion and friction behavior. There are different models for calculating contact area depending on the mode of deformation.

2.1.2.1 Plastic contact

Plastic deformation initiates at a mean contact pressure of $1.1Y$ where Y is the uniaxial yield stress of the material. As the normal load is further increased, the plastic deformation zone extends from beneath the indenter until it eventually reaches the surface. At this point, the normal stress over the asperity would be close to the indentation hardness (H) of the softer material, which

is about $3Y$. The resulting area of contact is $A_r = L/H$ which is independent of the geometrical area of contact and proportional to the normal load (L) [2,20].

2.1.2.2 Elastic contact

It is convenient to consider the contact between a loaded single asperity and a plane surface. It is a simple idealized case and the results derived for this geometry can be used in discussing more complex cases. There are mainly three single asperity models.

Hertz model

The classical Hertz theory gives an equation of the contact area for purely elastic contact, but neglects the adhesion force. Fig. 2.4 (a) illustrates this model [2,20]. According to Hertz model, the contact area between two semi-spheres is expressed as:

$$A_{r-Hertz} = 2.60\left(\frac{LR}{E^*}\right)^{2/3} \qquad \textbf{(2.2)}$$

$$\frac{1}{R} = \frac{1}{R_1} + \frac{1}{R_2} \qquad \textbf{(2.3)}$$

where R_1 and R_2 are the radius of the small and big semi-spheres, respectively. L is the normal load. E^* is the reduced Young's modulus of the two contacting metals, which is expressed as:

$$\frac{1}{E^*} = \frac{1-\nu_1^2}{E_1} + \frac{1-\nu_2^2}{E_2} \qquad \textbf{(2.4)}$$

where E_1, E_2, ν_1 and ν_2 are the Young's moduli and Poisson's ratios of the small and big semi-spheres, respectively [2,20].

JKR and DMT model

There are two competing models that include the effect of adhesion force on the deformation of the contact bodies. Johnson-Kendall-Roberts (1971) developed the JKR model, which suggests that the attractive intermolecular surface forces result in elastic deformation of the sphere and thus contact area increases beyond that predicted by the Hertzian equation. The adhesion is assumed to be limited to the contact area [21-23]. Derjaguin-Muller-Toporov (1975) established DMT model, which assumes that the attractive forces are exerted outside the contact area and do not change the deformed profile predicted by the Hertzian equation [21-23]. Fig. 2.4 (b and c) presents the two models respectively [20]. Equation 2.5 and 2.6 give the contact area for the DMT and JKR models, respectively.

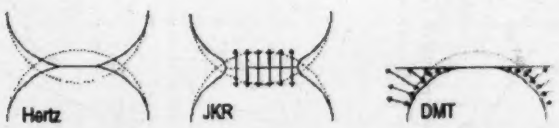

Figure 2.4 a) Hertzian contact, b) JKR contact, c) DMT contact [20,23].

$$A_{r-DMT} = \pi\left(\frac{3\pi W_a R^2}{2E^*}\right)^{2/3}\left(1+\frac{L}{2\pi W_a R}\right)^{2/3} \quad \textbf{(2.5)}$$

$$A_{r-JKR} = \pi\left(\frac{3R}{4E^*}\right)^{2/3}\left(L+3\pi W_a R+\left[6\pi W_a RL+(3\pi W_a R)^2\right]^{1/2}\right)^{2/3} \quad \textbf{(2.6)}$$

where W_a is adhesion energy between the two surfaces in contact and L is the normal load. JKR and DMT models apply to the opposite ends of a non-dimensional parameter called Tabor number (λ) which is a function of the elastic moduli of the two surfaces, their equilibrium spacing, asperity dimension and adhesion energy [7,22,24,25].

$$\lambda = \left(\frac{RW_a^{\ 2}}{E^{*2}\varepsilon^{*3}}\right)^{1/3} \quad \textbf{(2.7)}$$

where ε^* is the interatomic spacing. A low value of λ (λ <1) corresponds to a regime where the DMT model applies. High values of λ (λ >>1) corresponds to the JKR model [7,22,24,25]. Roughly speaking, the DMT model is applicable to hard materials while the JKR model is more suitable for soft materials [26].

Greenwood and Williamson proposed a parameter named plastic index (ψ), which indicates the average deformation mode of the rough surface [7,27,28]

$$\psi = \frac{E^*}{H}\sqrt{\frac{\sigma^*}{R}} \quad \textbf{(2.8)}$$

where σ^* is the standard deviation of the distribution of asperity heights, R is the radius of curvature of the asperity tips, which are assumed to be spherical, and H is the hardness. The deformation is elastic for ψ <0.6 and plastic for ψ >1 and elastic-plastic for 0.6< ψ <1 [7,27,28]. Plastic index is typically in the range of 0.1-100 for metal surfaces produced by normal engineering methods. Fig. 2.5 presents plastic index for aluminium surfaces with different engineering finishing [2].

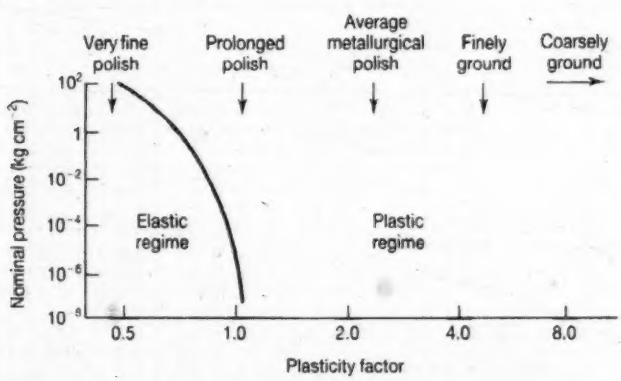

Figure 2.5 Asperity deformation mode and plasticity factor of aluminium surfaces with different roughness values [2].

2.2 Theories of friction

Friction is usually represented by the friction coefficient, which is the ratio between the frictional force (F) and the normal load (L) [1-3].

$$\mu = \frac{F}{L} \qquad (2.9)$$

Study of frictional behavior dates back to prehistoric times, when humankind took advantage of the frictional behavior of materials [29]. Amontons's work is often considered as the first comprehensive scientific investigation of frictional behavior [29]. There are three general laws of friction derived from experiments. The first and second friction laws were summarized by Amontons in 1699 [1,2,4,17,30], which were, however, described by Leonardo da Vinci about 200 years earlier than Amontons. Coulomb added the third law in 1758 [2].

The laws of friction are stated as follows:

1. The friction force is proportional to the normal load
2. The friction force is independent of the apparent area of contact
3. The friction force is independent of the sliding velocity

Although the laws of friction are applicable in many cases and can be regarded as the general guide to friction, there are also conditions under which the laws do not work [1,3,31].

The causes of friction have been investigated for many years. Many early investigators, including Amontons and Coulomb, suggested that friction was caused by mechanical interaction of

surface roughness or asperities. However, Bowden and Tabor's work showed that adhesion also contributed to friction [1,2,32].

Bowden and Tabor's model of sliding friction assumes that the frictional force results from two main sources. One is the adhesive force (F_{adh}) from the chemical interaction developed at the area of real contact between the surfaces, and the other is the deformation force (F_{def}) involving asperity-plowing and deformation. This dual molecular-mechanical concept has been generally accepted although these two contributions cannot be treated as strictly independent and their ratio in certain circumstance is usually difficult to define [1-3,31].

Friction force due to adhesion is expressed as

$$F_{adh} = A_r s \qquad \textbf{(2.10)}$$

where s is the shear strength of the material, A_r is the true area of contact which is the sum of the cross-sectional areas of all the asperity junctions.

The normal load is equal to the total area of asperity junctions multiplied by the average pressure of contact. The average pressure of contact is close to the indentation hardness of the softer material if the asperities deform plastically.

$$L \approx AH \qquad \textbf{(2.11)}$$

where H is the indentation hardness of the softer material.

Therefore the contribution to the coefficient of friction from the adhesion force is [1,2]

$$\mu_{adh} = F_{adh} / L \approx s / H \qquad \textbf{(2.12)}$$

Both shear strength and hardness are properties of materials. For metals, shear strength is roughly equal to 0.5 to 0.6 times yield strength while hardness is about three times the yield strength. As a result, for metals in air the friction coefficient due to adhesion is usually between 0.17 and 0.2 [2].

The tangential force needed to move a rigid conical asperity of semi-angle α on a plane surface may be expressed as the indentation hardness of the surface material multiplied by the cross-section area of the groove (Fig. 2.6) [2,13]:

$$F_{def} = Hax = Hx^2 \tan\alpha \qquad \textbf{(2.13)}$$

The normal load supported by the asperity is:

$$L = H\pi a^2 = H\pi x^2 \tan^2\alpha \qquad \textbf{(2.14)}$$

The coefficient of friction due to the ploughing term is therefore [2,13]

$$\mu_{def} = F_{def} / L = \cot\alpha / \pi \qquad \textbf{(2.15)}$$

where α is the semi-angle of a rigid conical asperity (Fig. 2.6).

The slopes of real surfaces are nearly always less than 10° (i.e. α >80°) which leads to μ_{def} to be less than about 0.1.

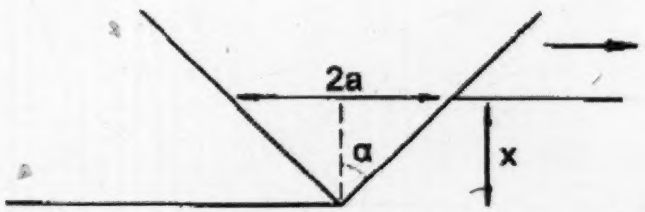

Figure 2.6 Model for the deformation component of friction. α is the semi-angle of a rigid conical asperity which indents and slides through the surface of a plastically deforming material [2].

The total friction coefficient representing the contributions from both adhesion and ploughing is therefore less than about 0.3. The values of measured friction coefficient are typically several times higher than the estimate. The discrepancy is explained by two effects: work-hardening and junction growth. Work-hardening of the asperity junctions will increase the relative value of shear strength in comparison with that of hardness and therefore will increase μ_{adh}. Junction growth takes into account tangential force which makes the real contact area increases.

The ratio of the adhesion and deformation contributions varies with the contact condition especially the contact force [1-3]. Under high loads, F_{def} plays the main role in generating the frictional force, while under low loads, F_{adh}, becomes predominant. For nano/micro devices, the small scale contacts and very smooth surfaces associated with information storage devices result in adhesive forces that play a more significant role than in conventional tribological applications [9].

2.3 Research of Friction and Adhesion

Considerable efforts have been made to fundamentally investigate adhesion and friction using experimental and theoretical approaches. The advance of experimental techniques, the development of analytical calculation and computer simulation deepened our understandings of friction and adhesion between two solids. Despite the numerous efforts, the mechanism involved is still not well clarified.

2.3.1 Research at macroscopic scale

Adhesion has been studied extensively by Buckley. He used ultrahigh vacuum apparatus and incorporated low energy electron

diffraction (LEED) and Auger spectroscopy into the system, so the surfaces could be characterized *in situ* [11,33].

Buckley has demonstrated that the adhesion and friction between two surfaces are related to the degree of matching between the crystal planes. For matched planes and directions, the planes with the highest atomic density and lowest surface energy have the lowest values of friction coefficient [1,11].

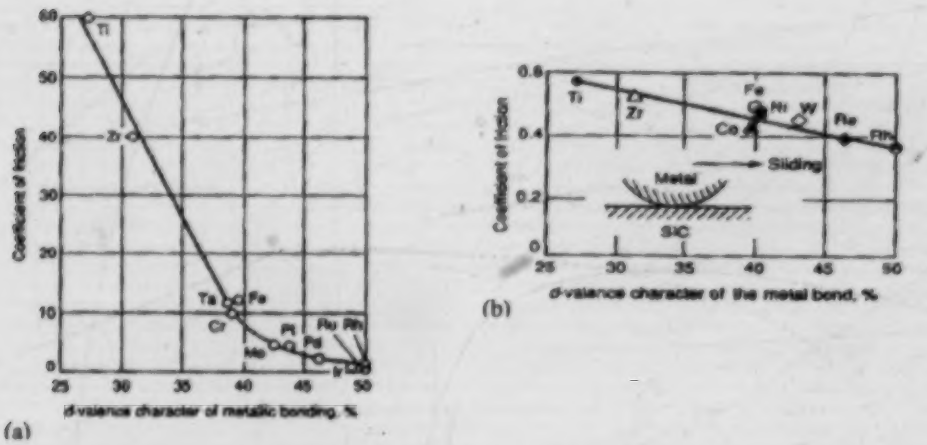

Figure 2.7 Friction coefficients measured in vacuum as a function of d-bond character of the metals. (a) Metals in contact with themselves. (b) Metals in contact with single-crystal SiC [11].

He also showed that adhesion is related to other fundamental properties of materials such as the degree of d-valence bond character of transition metals. As the degree of d-bond character

increases, the friction coefficients decrease no matter whether the metals are in contact with themselves (Fig. 2.7a) or with a ceramic material (Fig. 2.7b). The possible reason is that the greater the degree of bonding of a metal to itself, the less the bonding across the interface [1,11].

Other researchers made efforts to correlate experimental data of adhesion and friction with various intrinsic materials properties. Rabinowicz [13] correlated friction coefficients of clean metals with their ratios of adhesion energy to hardness (Fig. 2.8).

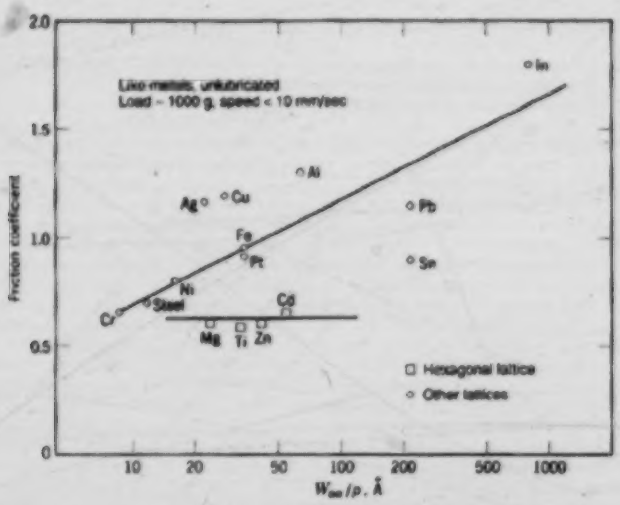

Figure 2.8 Friction coefficients for clean similar metals. Except for hexagonal latticed metals, the friction coefficient and the W_a/p ratio increase together [13].

Rabinowicz expressed Adhesion energy (W_a) as

$$W_a = \gamma_1 + \gamma_2 - \gamma_{12} = C_m(\gamma_1 + \gamma_2) \quad \textbf{(2.16)}$$

Where C_m is the compatibility parameter for the metals A and B, and always lies in the range 1 to 0. γ_1 and γ_2 are surface energies of the two contacting materials. The value of C_m is determined primarily by the metallurgical compatibility of the metals, and it is best evaluated from their binary phase diagram. Table 2.2 shows the compatibility parameter C_m of metals [13].

Table 2.2 Compatibility Parameter C_m of Clean Metals

	Identical Metals	Compatible Metals	Partially Compatible Metals	Partially Incompatible Metals	Incompatible Metals
Compatibility parameter c_m	1.00	0.50	0.32	0.20	0.12

Sikorski [34] investigated the adhesion of different metals by applying the twist-compression bonding method under normal atmospheric conditions and showed that high friction was always accompanied by strong adhesion, which was influenced by melting point, crystal structure, mutual solubility and hardness etc. Miyoshi [35] investigated the adhesion and friction of metals-ceramic contacts in vacuum and drew the conclusion that the adhesion and friction decreased with increasing Young's or shear modulus of the metal, which had a marked dependence on the metal's electron configuration. Vijh [36] correlated metal-metal bond strength with adhesion and friction between metals.

Ohmae [12] measured friction of 3d transition metals in contact with copper in vacuum and showed that the electronic structure of the metals is a better indication of the frictional behavior than compatibility ratings. Fig. 2.9 shows measured friction coefficients, percent filling of d-bands and the compatibility rating of the 3d transition metals with copper. The monotonic increase in friction coefficient for the metals can be explained by the filling of d-bands, not by the compatibility ratings as illustrated on the upper abscissa of the figure.

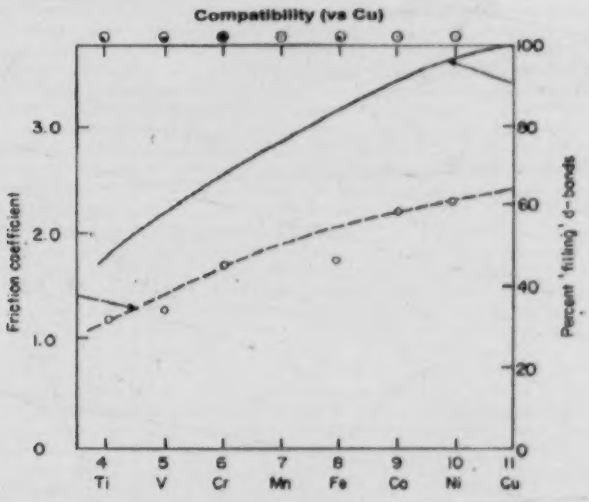

Figure 2.9 Friction coefficient of 3d transition metals in contact with copper [12].

Gellman et al. [37] combined surface science instrumentation with an ultrahigh vacuum (UHV) tribometer to study tribological

phenomena. This technique provides reproducible preparation of surfaces and atomic scale surface characterization. Friction anisotropy and the effects of the coverage of adsorbed species on friction between metal surfaces were investigated. Fig. 2.10 illustrates the instrument used for the UHV tribological study.

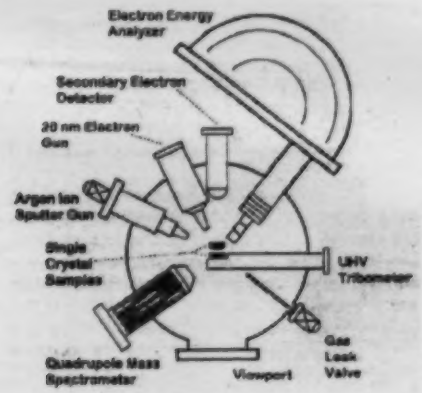

Figure 2.10 Schematic of a cross section through the cylindrical UHV chamber housing the UHV tribometer [37].

The apparatus contains two single crystal samples that are positioned at the focal point of the surface analysis instrumentation in the UHV chamber. The upper sample is mounted to an UHV manipulator that allows free motion within the chamber. The other sample is fixed to the tribometer, which measures the shear and normal forces between the two surfaces when they are in contact.

Both surfaces can be cooled to T <120K and heated to T>1000K. The sample surfaces can be cleaned using the Ar^+ sputter gun and annealing treatment. The clean surfaces of the samples can be analyzed using scanning Auger microscopy (SAM) and scanning electron microscopy (SEM). One of the samples, which can move freely on the UHV manipulator, can be analyzed using low energy electron diffraction (LEED). The clean surfaces of the two samples can be modified by the adsorption of species that are introduced into the vacuum as vapour through standard leak valves. The mass spectrometer is used to analyze the species in the gas phase and can also be used to measure the desorption kinetics of species on the surface of the manipulator sample [37].

2.3.2 Research at microscopic to atomic scale

Strong adhesive forces are short-range interactions arising from the inter-atomic interactions of two surfaces in contact, which largely depends on the surface electronic configuration and properties [17]. Understanding the atomistic mechanisms for the interactions that occur when two materials are brought together is fundamentally important to adhesion and friction. This is mainly explored by advanced experiment techniques, analytical studies and computer simulation.

2.3.2.1 Experimental studies

The development of scanning probe microscopes (SPMs) family including atomic force microscope (AFM), friction-force microscopes (FFM), scanning tunneling microscope (STM), and scanning Kelvin probe microscope (SKPM) etc. revolutionized our abilities to probe the morphological and electronic structure and investigate the nature of interatomic forces in materials [4,9,18].

AFM is a powerful tool that makes it possible to visualize the surface and analyze tribological features at the nanometer scale. The developments of AFM and its extension FFM have opened a new era in the field of tribology. Bhushan et al. [9,38-48] did considerable work on friction and adhesion with AFM and FFM. Landman [18] measured the adhesion between a nickel tip and gold substrate with AFM and compared the results with molecular simulation (MD). The effect of water adsorption on friction of $SrTiO_3$ (001) and boron carbide films were studied with FFM [49,50]. Park et al. [51] studied friction of a silicon pn junction using AFM to investigate the electronic contribution to friction. The influence of surface oxidation on adhesion and friction between 10 fold Al-Ni-Co decagonal quasicrystals was studied in ultrahigh vacuum (UHV) with an AFM[52]. Peressadko et al. [53] studied the influence of surface roughness on adhesion between elastic bodies using an AFM.

2.3.2.2 Analytical Studies

Physicists tried to calculate the interaction at the atomic level. The computational techniques range from first-principles, pair-potentials, many-body potentials to semi-empirical methods [54].

Rose et al. [55,56] found that the adhesive binding energy of different metals against the separation could be scaled into a single universal curve. Ferrante et al. [57] calculated the binding energy using a quantum mechanical jellium model for a number of simple metals in contact. Smith et al. [58,59] calculated the binding energy at transition metals interfaces using a more complete quantum mechanical formalism. Energies of adhesion between bcc Fe (111), (100) and (110) match and mismatch interfaces [60], and those between metal and oxide were also calculated [61].

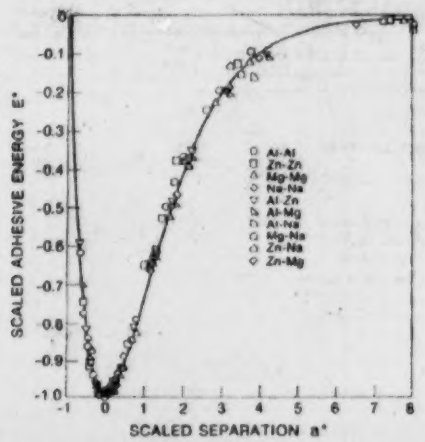

Figure 2.11 Adhesive energy versus separation for interfaces between Al, Zn, Mg and Na [57].

Fig. 2.11 presents the adhesive energies between all pairs of Al (111), Zn (0001), Mg (0001) and Na (110) calculated by Ferrante et al. [57] using first principles method.

Miedema and his coworkers related interface energies to the heat of alloying (chemical contribution) and the average grain boundary energy (geometrical contribution) of the two metals [62,63]. This semiempirical approach made it possible to quantitatively predict the adhesive energies for any type of metallic interfaces. Miedema also suggested an equation to relate surface energy of a metal to its electronic properties [64]. As a result, the adhesion energy of two metals could be related to their electronic properties.

Allan et al. [65-67] used a simple self-consistent method to calculate adhesion energy of two transition metals. The interface energy of two transition metals of the same series is expressed as a simple analytical function of the work functions and Fermi energies.

2.3.2.3 Computer simulation

Large-scale molecular dynamics (MD) simulations have greatly enhanced our understanding of the atomistic mechanisms for adhesion and friction. MD simulations can simulate a system of interacting atoms with high spatial and temporal resolutions by means of direct integration of equations of motion of atoms [54].

Landman et al. investigated the adhesion and tip sliding between several tips and substrate materials, including metallic (Ni and Au), ionic (CaF_2), covalent (Si), etc. [54]. Fig 2.12 presents the result of a MD simulation of the contact between a nickel indenter and an initially flat gold surface. As the indenter approaches the surface, the attractive force is sufficient to cause distortion of the gold surface, so the intimate contact occurs when the Ni tip is still at some distance above the original surface. When the tip is raised from the surface after indentation, the bond breaks within the gold atoms and significant transfer of gold to the nickel tip occurs (Fig. 2.12) [18].

Figure 2.12 Atomic configurations predicted by theoretical modeling of the contact between a nickel tip and an initially plane gold surface. It shows adhesion of gold atoms to the nickel tip as the tip is raised from the surface [18].

MD simulations of adhesion processes have also been performed by many other researchers with different emphases [68-71].

2.4 Electron work function (EWF)

2.4.1 Definition

Electron work function (EWF) is a parameter that characterizes the electronic behavior of metallic solid. EWF is the minimum energy required for an electron to escape from the Fermi level (E_F) to a point just outside the bulk metal. Fermi level is defined as the maximum energy occupied by an electron at the temperature of absolute zero [16,72,73]. A finite potential energy barrier (W) exists at each end of the solid. In order for an electron to escape from a metal, it must have a kinetic energy to overcome the potential barrier. The minimum energy that must be supplied to remove a free electron of E_F from the solid is called EWF. EWF (φ) is therefore determined as the difference between the Fermi level of a metal and the surface potential barrier (W) as the following equation [16,72,74].

$$\varphi = W - E_F \qquad \textbf{(2.17)}$$

EWF would be equal to E_F if there is no distortion of charge distribution in surface cells. In reality, charge distributions of surface cells are always different from charge distributions of cells inside the metal. This is because first the position of surface ions is slightly displaced from their ideal Bravais lattice positions, second surface cells do not have the symmetry of the Bravais lattice. Therefore surface cells have a non-vanishing electric dipole moment and may yield a non-vanishing net electrical surface charge [16]. The way in which the charge distribution in cells near the surface differs from that in the bulk depends on various surface conditions [16]. As the electron moves through the surface region, its energy is affected by the optical, electric and mechanical properties of the region. So EWF is an extremely sensitive indicator of surface condition and is affected by absorbed or evaporated layers, surface reconstruction, surface charging, oxide layer imperfections, surface and contamination, etc. [16,74-79].

As a fundamental electronic property of a metallic surface, EWF characterizes the electronic behavior of a metal and can be determined experimentally [74,80,81]. EWF has been widely used in various fields to investigate surface conditions of metals and alloys such as catalysis, adsorption phenomena, semi-conductivity,

surface physics and so on. EWF is becoming an important parameter in tribological research [74,77].

2.4.2 Measurements

2.4.2.1 General

EWF can be determined by direct or indirect techniques. Direct techniques are based on the emission of electrons from a surface. Depending on the external excitations, these techniques are subdivided into thermoemission, photoemission and exoelectronic emission. Indirect techniques determine EWF either by studying the effects of its surface on an external beam of electrons, or by measuring the contact potential difference (CPD) between its own surface and a reference surface [74,82,83].

CPD between two surfaces is the potential difference between them as they are brought together in electrical contact and thermodynamic equilibrium is achieved. The most common CPD measurement techniques are ionization and capacitor techniques. A radioactive source is required for ionization techniques, and its application is limited. The Kelvin method bade on CPD is the most widely used technique. The Kelvin probe is a noncontact, nondestructive vibrating capacitor device used to measure the work function difference between a conducting or partially conducting

specimen and a vibrating tip. It can be applied under a range of conditions including ambient, vacuum and even fluid environment [74,83].

2.4.2.2 Kelvin Probe Technique

The Kelvin method was first postulated in 1861 by the renowned Scottish scientist W. Tompson, later Lord Kelvin. Figure 2.13 illustrates the original apparatus used by Lord Kelvin [84]. In 1932 Zisman modified the Kelvin technique by vibrating one of the capacitor plates. In 1988, Baumgartner and Liess reported the manufacture of the micro-Kelvin probe with a resolution of 40μm. In 1991, Martin et al. and Veaver et al. used an AFM to achieve potential mapping with a lateral resolution around 50nm and voltage resolution in the microvolt range. The excellent resolution of this type of device has led to the term "nano-Kelvin probe" [85].

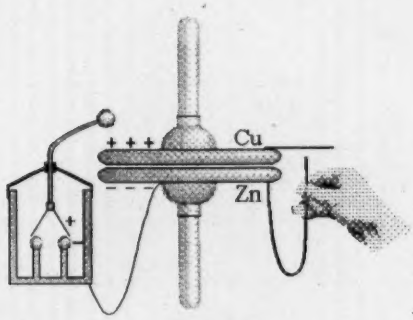

Figure 2.13 The original apparatus used by Lord Kelvin [84].

The energy diagram of two metal plates separated by a small vacuum gap is presented in Fig. 2.14 (a) [79]. The free electrons in a metal are prevented from escaping from it by electrical forces, which give rise to a surface potential barrier. When the two plates are connected electrically, thermodynamic equilibrium is achieved when the Fermi energy levels for the two metal plates are equal (Fig. 2.14 (b)). Electrons just outside the metal surfaces have different potentials since the equality of the Fermi levels is obtained by the flow of electrons from the plate with the lower work function (metal 1) to that with the higher one (metal 2). The first metal surface is charged positively and the second is charged negatively. The difference in the two potentials, known as the CPD (or surface potential) U_{CPD}, is the difference between the work functions of the metals, divided by the magnitude of the charge of one electron[74,79].

$$U_{CPD} = (\varphi_2 - \varphi_1)/e \qquad \textbf{(2.18)}$$

If an external compensating potential is used to establish the equilibrium of the surface potential barrier, this external potential will be equal in magnitude, but opposite in sign to the CPD. If the work function of one of the plates can be maintained constant (reference surface), the changes in the work function of the other

plate will manifest themselves as a change in CPD (referred to as change in surface potential). The change can be measured by detecting the charge flow between the plates of a capacitor [74,79].

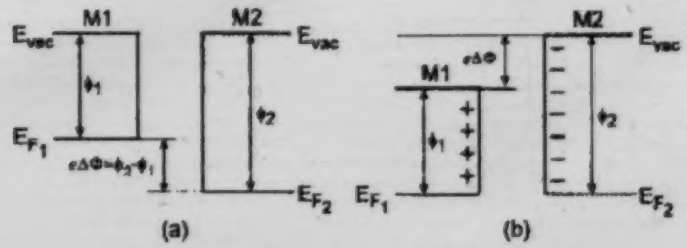

Figure 2.14 Energy diagrams for electrons in two metal plates (M_1 and M_2) separated by a small vacuum gap, E_{F_1} and E_{F_2} are the Fermi energy levels, E_{vac} is the surface potential barrier, (a) metal plates are isolated, and (b) plates are connected electrically and charged [79].

The Kelvin method involves placing a vibrating probe with radius (R), and vibration amplitude (d_{ac}), close to the sample and using it as one plate of a capacitor, with the grounded sample as the other plate. As the probe vibrates a current will flow onto and off the probe according to

$$I = \varepsilon \frac{\pi R^2}{l}(V_p - V_s)\omega d_{ac} Cos(wt) \qquad \textbf{(2.19)}$$

where V_p is a dc bias potential applied to the probe, V_s is the potential of the surface, 1' is the distance between the probe and the surface, and ε' is the dielectric constant between the plates of the capacitor. V_S is measured by adjusting V_p to nullify the current [85,86].

2.4.2.3 Kelvin probe system

There are a number of possible Kelvin probe system combinations. There are: static single probe system, scanning single probe system, ultrahigh vacuum (UHV) probe system, multi-headed bio scanning probe system and nano-Kelvin Probe (Kelvin Probe Microscopy) [84].

Scanning Kelvin Probe

Scanning single probe system can measure work function and surface potential topographics to tithing 1 meV energy resolution, and provides a method of simultaneously imaging sample height topographics [84].

Fig. 2.15 shows a schematic of the Scanning Kelvin Probe arrangement (a stationary probe is much the same but doesn't include the XY stage and Z course driver). The vibrating probe assembly is constructed from a voice coil housing containing the voice coil driver element, magnets and two 25mm diameter stainless steel springs. A digitally synthesized sinusoidal waveform

applied to the voice coil allows computer control of the frequency of oscillation, amplitude and height. The probe tip is directly mounted onto an I/V converter. The sample and probe are connected via a voltage source termed the "backing potential" (Vb), which is controlled by a 16-bit Digital to Analogue converter (DAC). A laboratory standard pre-amplifier, incorporating variable gain, roll-on and roll-off filters, Data-Acquisition System (DAS) and Digital Signal Processor (DSP) completes the measurement circuit [84].

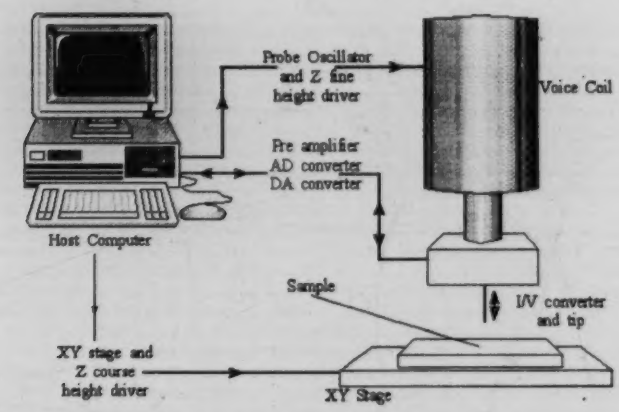

Figure 2.15 Scanning Kelvin probe arrangement [84].

Nano-Kelvin Probe (Kelvin Probe Microscopy)

Devecchio and Bhushan were the first to apply nano-Kelvin probe (also referred to as Kelvin probe microscopy (KPM)) for the detection of wear precursors at very low loads that precede wear

debris and/or measurable wear scars [79]. The technique was based on atomic force microscopy (AFM) and allowed mapping of surface potential simultaneously with topography measurements. AFM detects minute forces between a scanning tip and a sample via the deflection of a small cantilever upon which the tip is mounted. By changing the tip/cantilever materials and geometry, as well as the adaptations to the control of the cantilever, numerous physical properties of materials on the nanometer scale can be measured [78,85,86].

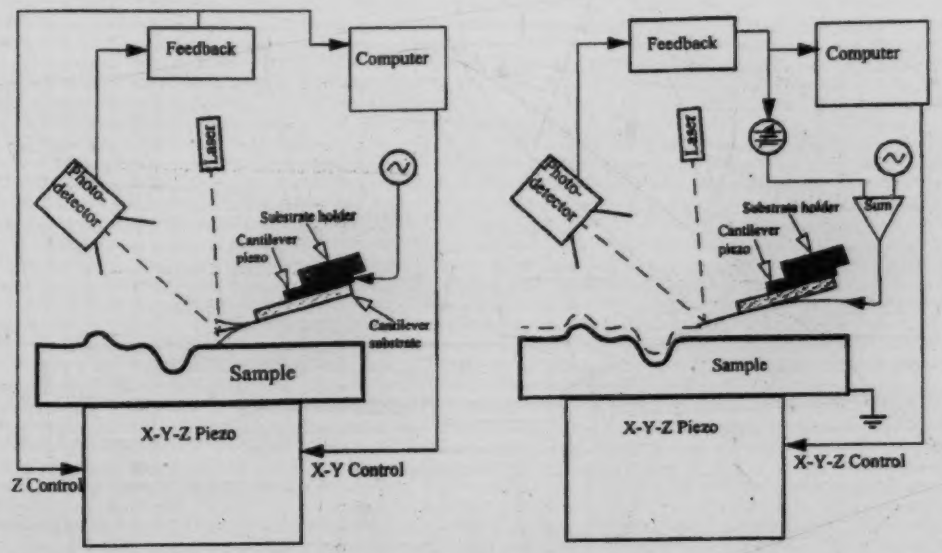

Figure 2.16 (a) Topography measurement in tapping mode. (b) Surface potential measurement in lift mode [86].

If the tip and the sample are electrically connected, electrons flow from the material with the smaller work function to the material with higher work function. This diffusion current builds up a double layer at the interface resulting in a contact potential difference $\Delta\varphi$ [78,85,86]:

$$\Delta\varphi = (\varphi_{tip} - \varphi_{sample})/e \qquad \textbf{(2.20)}$$

Three scanning modes of this microscope are used: Contact mode, tapping mode and lift mode (Fig. 2.16) [78,85,86].

Contact mode was used to abrade the specimen surface to simulate wear. Tapping mode is used to collect topography data after the wear scar is created and in preparation for the nano-Kelvin probe measurement. Lift mode is used to make the Kelvin probe measurements, which are made simultaneously with the topography scan in the tapping mode. After each line of topography scan is completed, the feedback loop controlling the vertical piezo is turned off, and the tip is lifted from the surface and traced over the same topography at constant distance of 100 nm. During this "interleave" scan, a DC bias potential and an oscillating (AC) potential was applied to the tip. The frequency of oscillating potential (operating frequency) is chosen to be equal to the resonant frequency of the cantilever. The feedback loop adjusts the DC bias on the tip to nullify the force and hence the vibration amplitude of the cantilever

at operating frequency. The Kelvin probe feedback output is recorded by the computer and by reversing the sign the surface potential map can thus be obtained [78,85,86].

2.4.3 Theoretical Analysis

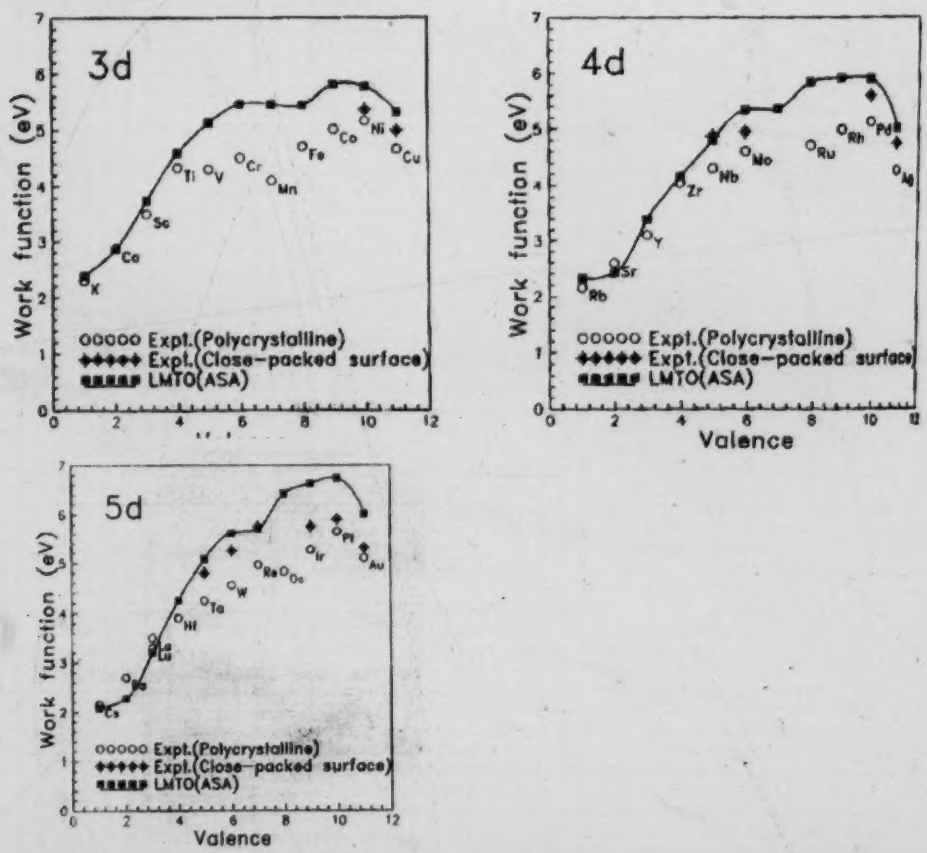

Figure 2.17 The calculated work function for the 3d, 4d and 5d series metals compared to available experimental polycrystalline data (open circles), and single-surface data (solid circles). All calculations are performed at the most close-packed surface of the experimentally observed crystal structure. The solid line connecting the theoretical values is a guide to the eye [81,89].

Evaluations of the work functions of the elements are of continuing interest. Scientists in early 20th century tried to calculate work function φ based on its relation with physical properties. Rother and Bomke expressed φ in terms of density, atomic weight and electronic valence in their empirical formula. Chittum and Gombas considered that φ was a function of the lattice energy in the crystal, Bartclink derived an approximate relationship between work function and the reciprocal of atomic volume for the alkali métals, Wigner and Bardeen developed another equation for work functions of the univalent metals in terms of the sublimation heat [87].

Scientists also developed methods to calculate EWF such as Jellium calculations, overlapping atomic charge densities, self-consistent Green's–function technique based on Andersen's tight-binding linear muffin-tin-orbital (TB-LMTO) method [81,87-89]. Fig. 2.17 illustrates the EWFs and surface energies of the closed-packed surfaces of transition metals calculated by Green's-function TB-LMTO method [81,89]. Brodie calculated EWF based on the electrostatic image potential energy without using *ab initio* methods in 1995. He expressed the work function of the polycrystalline metallic surface in terms of the atomic radius, Fermi energy, and

effective mass of an electron. Brodie's simple model produced results in very good agreement with experimental data. This approach was later substantially improved by Halas and Durakiewicz applying the metallic plasma model [90-92].

A simple electrostatic action model was proposed to investigate the effect of a dislocation on the EWF of a one-dimensional lattice. This model is based on the electrostatic action between electron and nuclei. From theoretical analysis, the authors have drawn the conclusion that in the elastic range tensile deformation decreases EWF while compressive deformation increases EWF. However, EWF always decreases with plastic deformation [93].

2.4.4 Correlation with other properties

Since EWF is a fundamental electronic property of metallic solids, it could be related to other properties of materials. In early 20^{th} century researchers started to calculate EWF and tried to relate it to physical properties. Langmuir observed a general parallelism for nine metals between thermionic work function and electrode potential [87]. This similarity was also noted by Scarpa for 16 metals [87]. Bockris reported an interesting reverse relationship between hydrogen overpotential and EWF [87]. It has been known

for a long time that EWF correlates well with many atomic properties such as ionization energies, electron affinity and electronegativity [72,94,95]. Ionization energy is approximately twice the value of EWF [90]. EWF also correlates with $n_{ws}^{1/3}$, $(H_{vap}/V_M^{2/3})^{1/3}$ and $V_M^{-1/3}$, where n_{ws} is the Wigner-Seitz electron density parameter, H_{vap} is the molar heat of vaporization, and V_M is the molar volume [94].

2.4.4.1 Periodicity of electron wok function

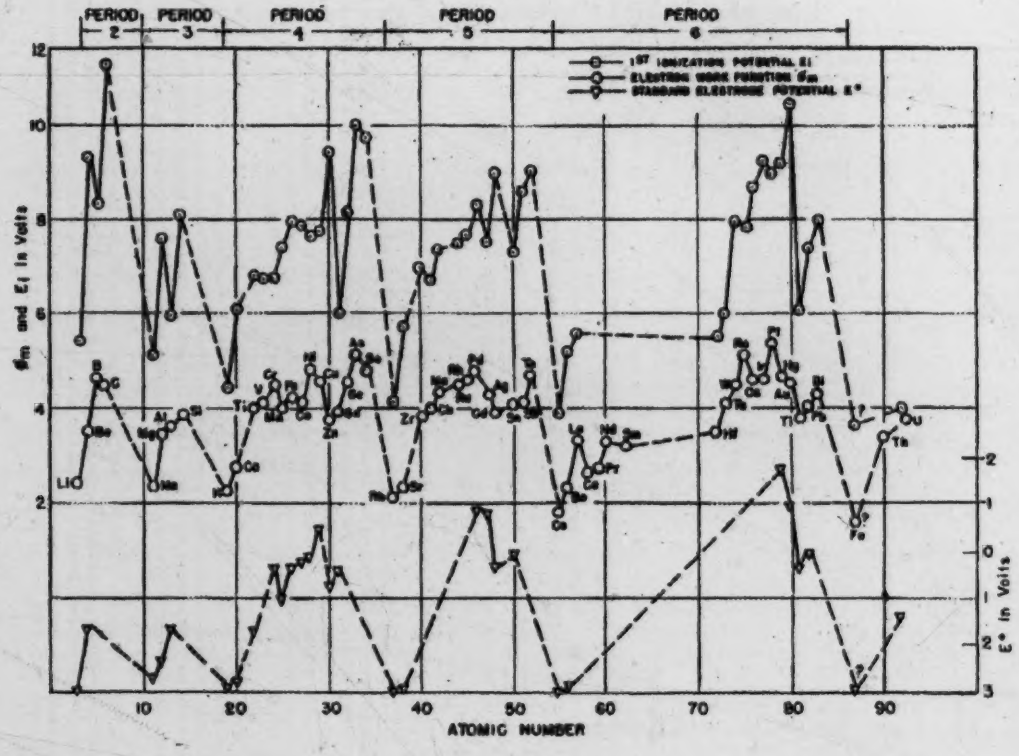

Figure 2.18 Plots of work function, first ionization potential, and standard electrode potential versus atomic number [87].

Table 2.3 EWFs (eV)(bottom row) and Ionization energies (eV)(upper row) of polycrystalline specimens [88,90,96]

$_{1}$H 13.598																	$_{2}$He 24.58
$_{3}$Li 5.39 2.9	$_{4}$Be 9.32 4.98											$_{5}$B 8.30 4.45	$_{6}$C 11.26 5.0	$_{7}$N 14.54	$_{8}$O 13.61	$_{9}$F 17.42	$_{10}$Ne 21.56
$_{11}$Na 5.14 2.75	$_{12}$Mg 7.64 3.66											$_{13}$Al 5.98 4.28	$_{14}$Si 8.15 4.85	$_{15}$P 10.55	$_{16}$S 10.36	$_{17}$Cl 13.01	$_{18}$Ar 15.76
$_{19}$K 4.34 2.30	$_{20}$Ca 6.11 2.87	$_{21}$Sc 6.56 3.4	$_{22}$Ti 6.83 4.33	$_{23}$V 6.74 4.3	$_{24}$Cr 6.76 4.5	$_{25}$Mn 7.43 4.1	$_{26}$Fe 7.90 4.5	$_{27}$Co 7.86 5.0	$_{28}$Ni 7.63 5.15	$_{29}$Cu 7.72 4.51	$_{30}$Zn 9.39 4.33	$_{31}$Ga 6.00 4.15	$_{32}$Ge 7.89 5.0	$_{33}$As 9.81 4.77	$_{34}$Se 9.75 5.9	$_{35}$Br 11.84	$_{36}$Kr 14.00
$_{37}$Rb 4.18 2.16	$_{38}$Sr 5.69 2.59	$_{39}$Y 6.38 3.1	$_{40}$Zr 6.95 4.05	$_{41}$Nb 6.88 4.3	$_{42}$Mo 7.18 4.6	$_{43}$Tc 7.28 4.9	$_{44}$Ru 7.36 4.71	$_{45}$Rh 7.46 4.98	$_{46}$Pd 8.343 5.12	$_{47}$Ag 7.57 4.26	$_{48}$Cd 8.99 4.22	$_{49}$In 5.78 4.12	$_{50}$Sn 7.34 4.42	$_{51}$Sb 8.64 4.55	$_{52}$Te 9.01 4.95	$_{53}$I 10.45	$_{54}$Xe 12.13
$_{55}$Cs 3.893 2.14	$_{56}$Ba 5.21 2.7	$_{57}$La 5.57 2.96	$_{72}$Hf 7.00 3.9	$_{73}$Ta 7.89 4.25	$_{74}$W 7.98 4.55	$_{75}$Re 7.87 4.87	$_{76}$Os 8.70 4.83	$_{77}$Ir 9.0 5.27	$_{78}$Pt 8.96 5.65	$_{79}$Au 9.22 5.1	$_{80}$Hg 10.43 4.49	$_{81}$Tl 6.11 3.84	$_{82}$Pb 7.41 4.25	$_{83}$Bi 7.29 4.22	$_{84}$Po 8.43 5.0	$_{85}$At 9.64	$_{86}$Rn 10.74
$_{87}$Fr 3.98 2.1	$_{88}$Ra 5.28 2.8	$_{89}$Ac 5.17 3.2															

$_{58}$Ce 5.466 2.97	$_{59}$Pr 5.42 2.96	$_{60}$Nd 5.49 3.2	$_{61}$Pm 5.54 3.1	$_{62}$Sm 5.6 2.85	$_{63}$Eu 5.67 2.5	$_{64}$Gd 6.14 3.17	$_{65}$Tb 5.85 3.15	$_{66}$Dy 5.93 3.25	$_{67}$Ho 6.02 3.22	$_{68}$Er 6.10 3.25	$_{69}$Tm 6.18 3.1	$_{70}$Yb 6.25 3.0	$_{71}$Lu 5.43 3.3
$_{90}$Th 6.08 3.4	$_{91}$Pa 5.89 3.7	$_{92}$U 6.05 3.63	$_{93}$Np 6.19 3.9	$_{94}$Pu 6.06 3.6	$_{95}$Am 6.00 3.7	$_{96}$Cm 6.02 3.9	$_{97}$Bk 6.23 3.8	$_{98}$Cf 6.30 4.0	$_{99}$Es 6.42 3.3	$_{100}$Fm	$_{101}$Md	$_{102}$No	$_{103}$Lr

The relationship between the work function and atomic number has been widely recognized and reported in the literature. Michaelson selected and analyzed the experimental results published during the period from 1924-1949, and plotted the work function, first ionization potential, and standard electrode potential of 57 elements versus atomic number. The plot (Fig. 2.18) shows that like the chemical properties of the elements, the work function is a periodic function of atomic number [87]. The currently accepted experimental data of EWF is summarized in Table 2.3, which shows a well-defined periodicity [90,96]. In the table, under the symbols of

elements, the upper row numbers are ionization energies, the bottom row numbers are EWFs (eV).

2.4.4.2 Electron work function and interface barrier

Ferrante [57] showed that the bimetallic interface barrier is related to EWFs of metals. For same metal interface, the barrier approaches the EWF of the metal; for two different metals, the barrier is intermediate between EWFs of the two metals. Table 2.4 lists the interface barriers for separation distance of 1.59 nm.

Table 2.4 Interface barriers and work function of metals at large separation [57]

Interface barrier (eV)		Work function (eV)	
Al-Al	3.79	Al	3.87
Zn-Zn	3.76	Zn	3.80
Mg-Mg	3.62	Mg	3.66
Na-Na	3.01	Na	3.06
Al-Zn	3.76		
Al-Mg	3.69		
Al-Na	3.42		
Zn-Mg	3.69		
Zn-Na	3.41		
Mg-Na	3.32		

2.4.4.3 Electron work function and Poisson's ratio

Baughman et al. [94] correlated EWFs of some metals with their Poisson's ratios when stretched along the [110] direction. Poisson's ratios were measured for $[1\ \bar{1}\ 0]$ and [001] lateral directions. Fig. 2.19 and Fig. 2.20 present correlations of

polycrystalline EWFs with the experimentally derived Poisson's ratios (ν) of B.C.C. metals and F.C.C. phases of the non-ferromagnetic elemental metals, respectively. In both figures, unfilled squares denote ν (110, $1\bar{1}0$) and filled diamonds for ν (110, 001).

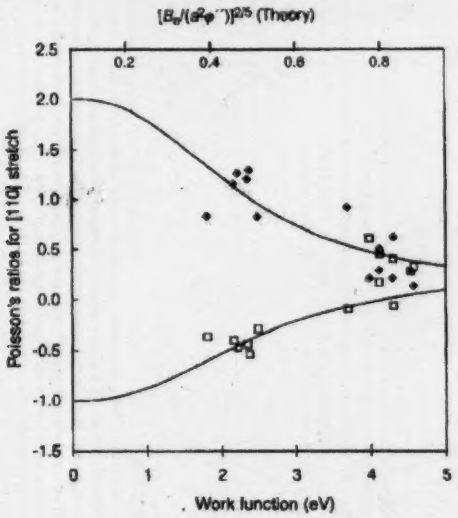

Figure 2.19 Correlations between ν (110, $1\bar{1}0$) and ν (110, 001) of B.C.C metals and the polycrystalline work functions. The unfilled squares denote ν (110, $1\bar{1}0$) and filled diamonds for ν (110, 001) [94].

In Fig. 2.19, the curves are predicted dependencies of ν (110, $1\bar{1}0$) and ν (110, 001) (bottom and top curves, respectively) on $[B/(b^2\phi'')]^{2/5}$. In this equation, B is bulk modulus, b is the lattice parameter, ϕ is the sum of nearest-neighbor central force

interaction, $\phi'' = d^2\phi/dr^2$ evaluated at the equilibrium interatomic separation $r = r_0$.

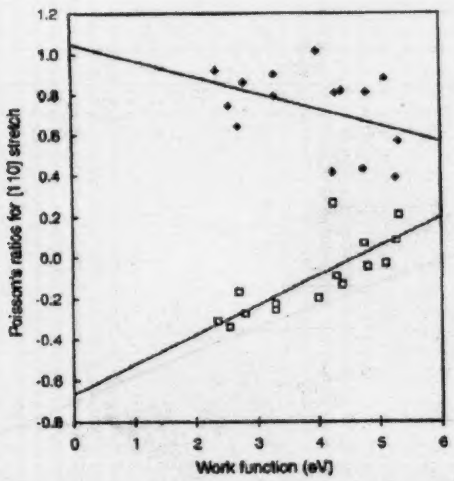

Figure 2.20 Correlations between ν (110, $1\bar{1}0$) and ν (110, 001) and polycrystalline work function for F.C.C. phases of the non-ferromagnetic elemental metals. The lines are least-squares fits to the experimental results. The unfilled squares denote ν (110, $1\bar{1}0$) and filled diamonds for ν (110, 001) [94].

2.4.4.4 Electron work function and surface energy

EWF is an important parameter in estimating the formation energy of binary alloys, in which charge transfer taken place from one constituent to the other to equalize the electrochemical potential throughout the crystal. By relating the surface energy of solid metal to the heat of formation of binary alloys and using the

data of surface energies of liquid metals, Miedema [64] suggested a semi-empirical equation to relate the surface energy of a metal to its electronic properties. This equation has the following form [64]:

$$\gamma = n_{ws}^{1/3} / (\varphi^* - 0.6)^2 \qquad (2.21)$$

where γ is the surface energy of a metal at 0 K; n_{ws} is the electron density at the boundary of the Wigner-Seitz cell; φ^* is a parameter approximately equal to EWF of a metal and related to its electronegativity [64,72,95,97,99].

Zadumkin [100] also correlated surface energy of the smooth facets of a metallic single crystal with its EWF using the following equation:

$$\varphi_i + \frac{C}{Z} b^2 \gamma_i = const. \qquad (2.22)$$

where γ_i and φ_i are the surface energy and EWF of the face with Miller indices (hkl), respectively. C is a constant which only depends on the type of structure. Z is the number of valence electrons. b is the lattice constant or the unit cell dimension of base plane in the case of the hexagonal structure.

Kalazhokov et al. [101] further developed the relation between surface energy and EWF. Surface energy was expressed as a function of EWF as follows

$$\gamma_i = (2 - \frac{\varphi_i}{\varphi_0})\varphi_0 \qquad (2.23)$$

where φ_0 is the EWF of the polycrystalline surface.

2.4.4.5 Electron work function and adhesion force

EWF is also related to crystallographic orientation and adhesion force [75]. Table 2.5 shows EWF and adhesion force (AF) of different crystallographic planes of copper. EWF decreased as the surface atomic packing density decreased in the following order (011), (112), (321) and (413). A clear relationship between AF and φ was demonstrated. The lower the φ, the higher is the AF. EWF is clearly a parameter reflecting the adhesive force [75].

Such a correlation between the EWF and the crystallographic orientation is consistent with theoretical analysis. According to an electrostatic force model, if small disturbance from the formation of the electric double layer at surface is neglected, the EWF is mainly dependent on the electrostatic interaction between electrons and nuclei in the surface layer. A closely packed plane has a higher EWF because an electron is subjected to higher attractive forces from the positive nuclei [102].

Adhesive force has a strong dependence on the surface arrangement. According to a "broken bond model" for surface energy, a closely packed plane has a lower surface energy than a

loosely packed plane, because the former has few broken bonds that are active. Fewer broken bonds of a closely packed surface provide fewer positions to interact with foreign atoms or the surface is less active when in contact with another surface, thus leading to lower adhesive force [75].

Both the adhesive force and EWF are dependent on the arrangement and nature of atoms in the surface layer; the EWF may therefore be a parameter that reflects the adhesion characteristic of a surface. Even for more complicated surface structures involving, e.g., adsorption of foreign atoms and lattice distortion due to residual stress, the correlation between AF and EWF may also be expected and predicted from the viewpoint of the electrostatic force model [75,102].

Table 2.5 EWF and adhesion force of single crystal copper with different crystallographic planes [75]

Orientation	(011)	(321)	(112)	(413)
φ (eV)	4.59	4.12	4.56	4.00
F (nN)	17.3	19.4	17.4	21.3

2.4.4.6 Electron work function and electrode potential

When a piece of metal is placed in an electrolyte solution, an electric potential difference is developed between the metal and the

solution as the result of charge transfer to equalize the Fermi level. This phenomenon is similar to what occurs when two dissimilar metals are placed in contact [103,104]. It is not surprising that electron work function is a component of electrode potential, which is expressed in equation (2.24). This complete expression of electrode potential (E^M) is obtained by considering the work to transfer electrons from the measuring electrode to the reference electrode [105]:

$$E^M = \varphi_o^M / e + \delta\chi_\sigma^M - g^{s^*}(dip)_\sigma + g_{s^*}^M(ion)_\sigma - E_T(ref) \qquad \textbf{(2.24)}$$

where φ_o^M is the electron work function of a clean metal surface and $\delta\chi^M$ is the modification as metal M is brought in contact with solution S^* (electronic term), $g^{s^*}(dip)$ is the contribution due to any preferentially orientated solvent molecules (dipolar term), and $g_{s^*}^M(ion)$ is the additional potential drop due to the presence of free charges on either sides of the interface (molecular term). $E_T(ref)$ is the potential barrier at the reference electrode and is known as the "absolute potential" of the reference electrode [105].

A two–Kelvin probe arrangement was used to monitor in situ both the working and reference electrode work function in a Y_2O_3-stabilized-ZrO_2 (YSZ) solid electrolyte cell, which is shown in Fig. 2.21 (a). It consists of an 8 mol% YSZ disc, which is an O^{2-}

conductor and the most commonly used solid electrolyte at temperatures 573-1373 K. On this YSZ disc, working, counter and reference electrodes were deposited. Two Kelvin probes were used to measure *in situ* work functions of the gas-exposed electrode surfaces of the working and reference electrodes, respectively (Fig 2.21 (b)) [106].

The potential difference U_{WR} between the working (W) and reference (R) electrodes reflects the difference of the actual work function φ_W and φ_R of the two electrodes [106,107]:

$$eU_{WR} = \varphi_W - \varphi_R \qquad \textbf{(2.25)}$$

In this equation, φ_i denotes the actual, experimentally measured work function of the gas-exposed electrode surface, which is related to the EWF of a clean metal surface (φ_o) as shown in the following equation [106-108] :

$$\varphi_W = \varphi_{W,0} + \Delta\varphi_W \qquad \textbf{(2.26)}$$

where $\Delta\varphi_W$ is the modification of $\varphi_{W,0}$ induced by the contact with the solution.

The absolute electrode potential $U_{O_2}(abs)$ in solid state electrochemistry is defined as [106,107]:

$$U_{O_2(abs)} = \varphi / e \qquad \textbf{(2.27)}$$

where φ is the work function of the gas-exposed electrode surface of the metal electrode in contact with the YSZ solid electrolyte at a fixed standard temperature and oxygen pressure. It expresses the energy to move an electron from vacuum to the Fermi level of the solid electrolyte.

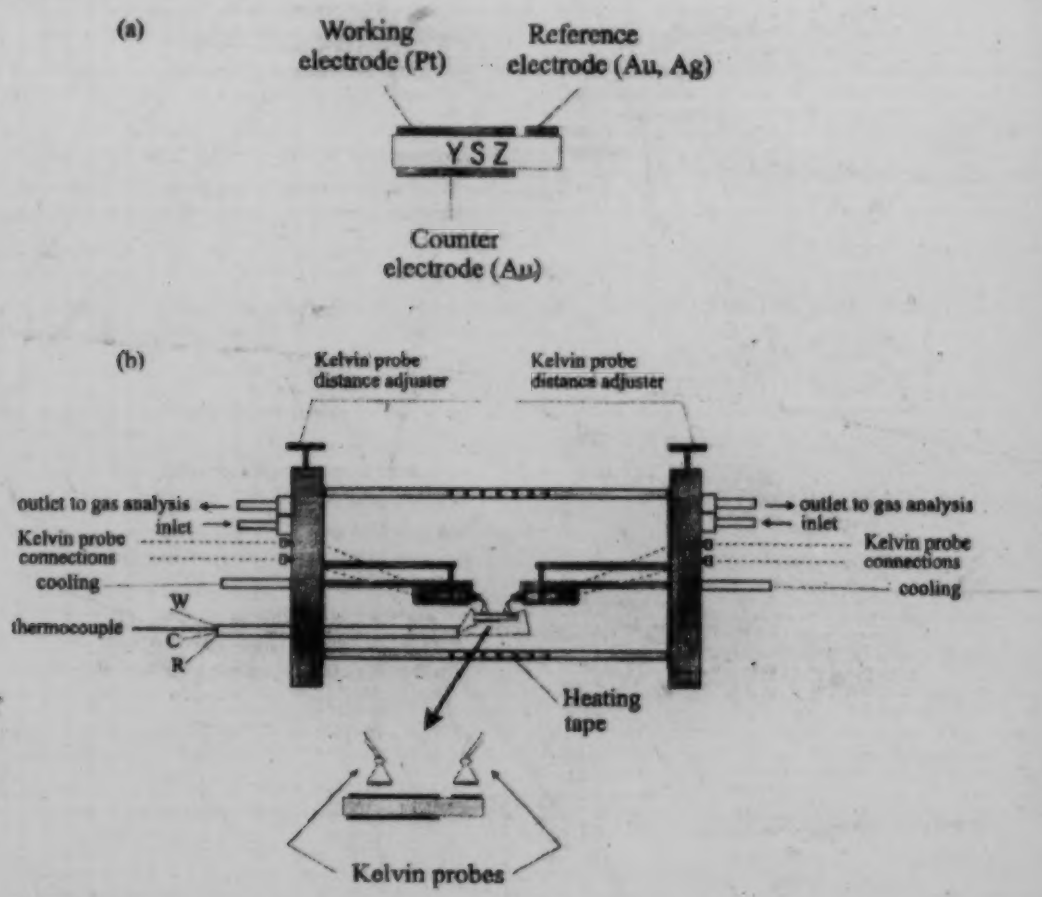

Figure 2.21 (a) Solid electrolyte cell consisting of a YSZ disk with working (Pt), reference (Au, Ag) and counter electrodes (Au). (b)Electrochemical reactor with two Kelvin probes [106].

2.4.4.7 Electron work function and number of transferred electrons

When two materials are brought into contact, their Fermi energies must become continuous across the junction. This equalization of the Fermi energy may require transfer of charges from one material of low EWF to the other with higher EWF [109]. Lee [110] related the number of transferred electrons with EWF using the following equation:

$$\Delta N = \Delta\varphi / \sum E_g^{AV} \qquad (2.28)$$

where ΔN is the number of transferred electrons, $\Delta\varphi$ is the difference of electron work function, and $\sum E_g^{AV}$ is average energy gap which is the difference in energy between the bottom of the conduction band and the top of the valence band [110].

2.4.5 Application of EWF

EWF is one of the fundamental characteristics of metals or semiconductors [16,72]. It is very sensitive to almost all processes which occur during friction and wear of metallic and semiconductor surfaces such as deformation and changes in the faulted structure, alterations of the chemical and phase compositions, adsorption and desorption of surrounding gases and lubricant molecules [74,78,111,112]. As a simple and inexpensive method, the Kelvin

probe technique provides a powerful tool for noncontact monitoring of changes in EWF. On-line monitoring EWF changes during surface rubbing provides the information on critical points in sliding process and the kinetics of friction processes [74,113,114]. Kelvin probe method has also been used to detect wear precursor [78,86,111], determine electrochemical reactivity [115-117], determine yield strain [118,119], and characterize interfacial bonding [77] etc.

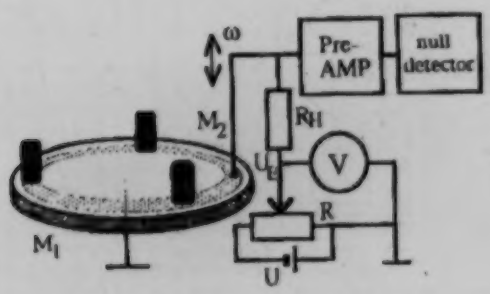

Figure 2.22 Kelvin probe combined with friction testing machine [120].

Combining Kelvin probe with a friction testing machine makes it possible to record the change of EWF during friction process, which reflects the changes in the material surface layers. Fig. 2.22 shows a Kelvin Method Combined with a friction testing machine. Such combined Kelvin probe techniques have been used in tribological studies [74,113,114,120-122].

2.4.5.1 Critical points with respect to changes in normal load

Studies of a wide range of materials with different crystalline lattices, strengths and chemical compositions have shown similar qualitative dependence of the rubbing surface's EWF on the normal load (Fig. 2.23). In general there are three specific zones. First, there is an increase of the EWF with load in the first zone. In the second zone the EWF of friction surface decreases. With further loading in the third zone there is very little change until the beginning of ploughing, which is detected by increase of the friction force and the bulk temperature of the sample. During ploughing the value of the EWF decreases sharply [74].

Additional investigations of specimens explained the results on the basis of dislocation interactions. The first zone mainly corresponds to elastic deformation and early stages of plastic deformation without a significant increase of dislocation concentration near the surface. In the second zone, plastic deformation dominates, but these processes are not saturated yet from the viewpoint of the density of dislocations. In the third zone, plastic processes are also important, but there is a dynamic process involving generation and annihilation of dislocations and the creation of micropores and microcracks [74,113].

Therefore the changes of EWF can tell the changes in the material surface layers. This change is not reflected by external friction parameters such as friction force and bulk temperature. It has been found that during long-run trials the wear rate is very low at loads corresponding to the first and second zones. For the third zone, damaged spots and high wear rates are observed [74,113].

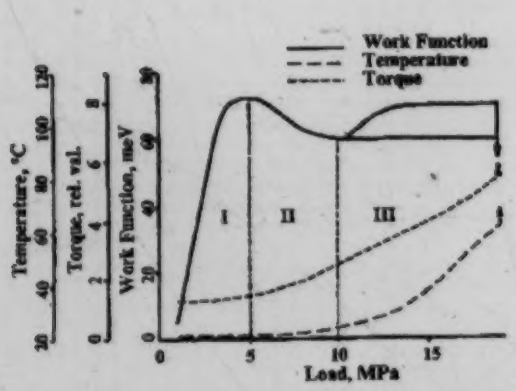

Figure 2.23 EWF, torque and surface temperature vs. normal load curves for the surface of a bronze sample [74].

Additional experiments have shown that the transition load separating the second and third zone could serve as an objective experimental criterion to estimate the serviceability of tribological materials. This transition is probably related to the critical transition between mild and severe wear for a given material [74,113].

This criterion allows us to compare the performance of various materials of friction couples and to optimize their chemical and phase composition as well as lubricants. Examples involving powder metallurgy materials and porosity optimization are provided in Fig 2.24 and 2.25, respectively. By optimizing tin content (Fig. 2.24) or porosity (Fig. 2.25), the critical load which marks the transition from mild to severe wear can be maximized for a given material.

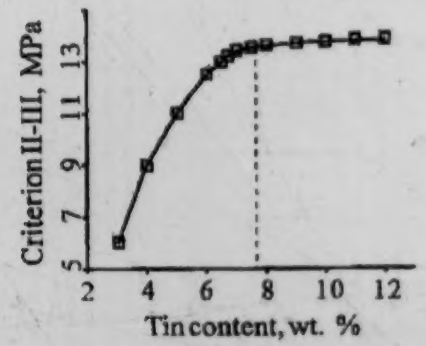

Figure 2.24 Example of power metallurgy material optimization (tin content) [74].

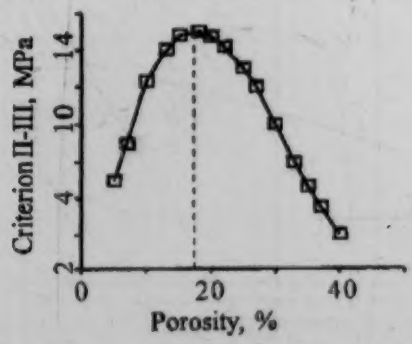

Figure 2.25 Example of powder metallurgy material optimization (porosity) [74].

2.4.5.2 Application of EWF in wear research

In microelectromechanical systems (MEMS), wear depths of a few nanometers can be critical and any wear debris could be an indication of catastrophic failure. EWF can detect atomic scale structural changes and/or chemical changes at the surface exposed to wearing forces; EWF is also a useful parameter for studying wear precursors on a nanometer size scale [78,79,85,86].

Devecchio and Bhushan were the first to apply nano-Kelvin probe (also referred to as Kelvin probe microscopy (KPM)) for the detection of wear precursors at very low loads that proceed wear debris and/or measurable wear scars [79]. The technique was based on AFM and allowed mapping of surface potential simultaneously with topography measurements for samples that have been abraded by an AFM tip. Samples studied include single crystal aluminum, gold, silicon, alumina [78,79,85,86]. They represent conducting, semi-conducting, insulating materials, respectively. It was shown that even in the case of no visible deformation of the surface, as observed by topography scans of an AFM, there is often a large change in the potential at the surface of the sample. The change in surface potential could be the result of chemical and structural changes in the first few nanometers of the sample. This allows for the study of the onset of wear in the ultralow wear regime, which is

not possible with other techniques. Fig. 2.26 shows one representative scar made from these tests along with representative cross sections [86]. The worn region of the sample has higher potential (lower work function) with respect to the non-abraded area. One possible explanation for the surface potential change in the worn region is that oxide layers and surface contaminants are being removed by the wear process, exposing the material of the bulk sample below [85,86].

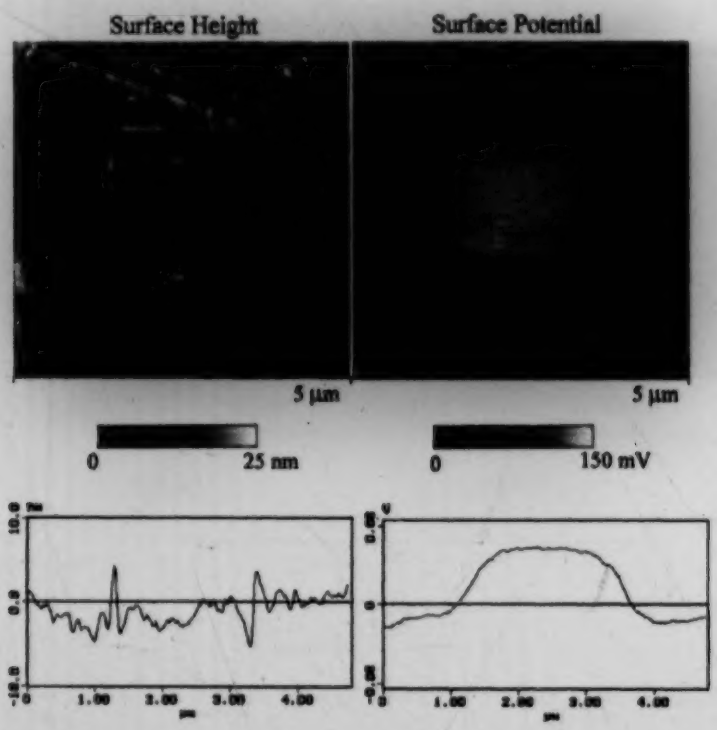

Figure 2.26 Surface height and surface potential maps of wear regions on a single crystal aluminum sample at 1µN. Included are cross-section analyses for each map [86].

Kelvin method was also used to detect onset of wear and to study the history prior to the occurrence of measurable wear in a macroscopic system [111]. Fig. 2.27 compares the three evaluation methods: weigh loss measurement, morphological observation and Kelvin probe technique. Among the three methods under study, the Kelvin probe method was proved to be the most sensitive one to changes in surface condition.

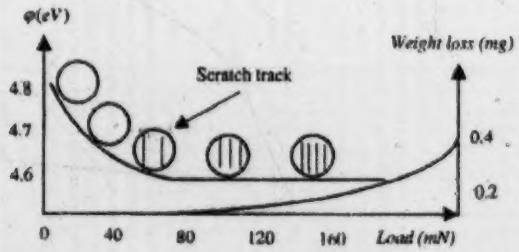

Figure 2.27 Comparison of the sensitivities of the three methods to wear: weight loss measurement, morphological variation, and the EWF measurement [111].

2.4.5.3 Application in corrosion

The EWF is a measure of the electrochemical stability or inertness of a material and has a close relation with the corrosion behavior of the material. Materials with higher EWF have higher corrosion resistance. The Kelvin probe technique is a useful tool to investigate the corrosion behavior of materials [115-117,123]. Fig.

2.28 presents EWFs of the yttrium (Y)-free and Y-containing 304 stainless steel after passivation treatment in 35% HNO_3. The passive film of a Y-containing 304 steel sample has higher EWF, which implies that this sample is more inert and more protective against electrochemical attack than a Y-free steel sample. This has been proved by higher corrosion resistance and improved polarization behavior of the Y-containing sample in a dilute H_2SO_4 solution [117].

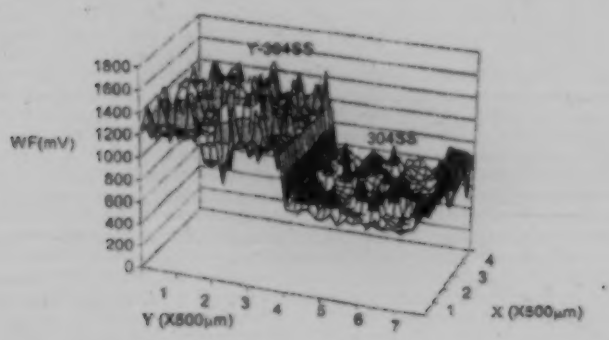

Figure 2.28 EWF of yttrium(Y)-free and yttrium (Y)-containing 304 stainless steel after passivation treatment in a 35% HNO_3 solution for 12 h [117].

2.4.5.4 Determine yield strain

Because of the high sensitivity of the EWF to surface condition, Kelvin probe was used to determine the materials yield strain under different types of stresses [118,124,125]. EWF decreases with tensile stress while increases with compressive

stress in the elastic range. Once deformation becomes plastic, EWF decreases rapidly due to the appearance and displacement of dislocations in surface layers [74,118,124,125]. The rapid drop in EWF makes it possible to determine yield strain of material using the Kelvin probe technique. Fig. 2.29 illustrates variations in EWF (φ) of copper with respect to tensile and compressive stress. ε_1 and ε_2 corresponding to the yield strain under tensile and compressive stress, respectively [124]. Other researchers also noticed the rapid decrease in EWF when the yield point was reached (Fig. 2.30) [74,112,113].

EWF is also used to characterize interfacial bonding and to study the effects of grain size on yield strain of brass [77,126].

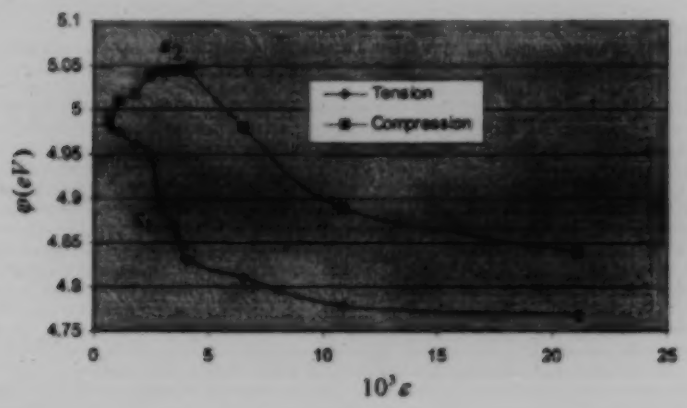

Figure 2.29 Variations in the EWF of copper with respect to elastic and plastic deformations [124].

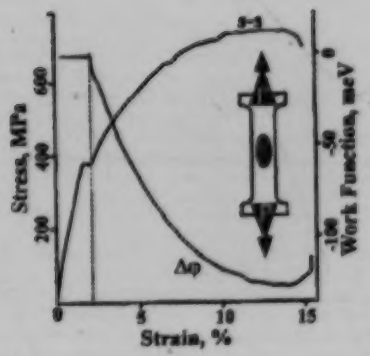

Figure 2.30 Results of simultaneous measurements of the regular stress-strain diagram and the EWF for medium carbon steel [113].

Chapter 3 : Metal-Ceramic contact: adhesion and friction between 3d transition metals and ceramics

This chapter presents the experimental study of adhesion and friction between ceramic and metal under light loads. Since electrons in a ceramic material are localized, the adhesion between a metal and a ceramic is mainly dependent on the electron behavior of the metal. Therefore the correlation between EWF and adhesion as well as friction is easier to be observed.

Adhesion and friction between 3d transition metals and ceramic were investigated under different loading conditions. EWF was measured using a scanning Kelvin probe. Adhesion and friction under light loads between a silicon nitride tip and metal surfaces were evaluated employing an atomic force microscope (AFM) that may also function as a lateral force microscope (LFM). Friction of the metal samples under a sharp tungsten carbide tip at higher load levels involving plastic deformation was also measured using a micro tribometer. It was demonstrated that there was strong correlation between the EWF, adhesion and friction. Higher EWF corresponded to lower adhesive force and thus lower friction when

measured under light loads using the AFM/LFM. Such correlation stems from the fact that the measured adhesion and friction are due to the intrinsic interaction between the sample and AFM/LFM tip, which is governed by the electronic behavior of the metal reflected by its EWF. However, such correlation became weaker when the friction was evaluated under a sharp tip at higher load levels. In this case, the friction behavior of a target metal was mainly determined by its mechanical behavior [127].

3.1 Introduction and objective

Friction is the resistance to movement when two surfaces in contact move tangentially in opposite directions. Friction force comes from two main contributions one is the adhesive force that arises from contact areas between two surfaces and the other is the deformation force needed for the surface with certain roughness or asperities to mutually plow each other. The coefficient of friction is thus expressed as $\mu = \mu_{adh} + \mu_{def}$, where μ_{adh} and μ_{def} is the friction coefficient from adhesion and deformation, respectively. The ratio of these two contributions varies with the contact condition especially the contact force [1-3,11]. Fundamental understanding of the correlation between friction behavior and material properties is

therefore important to design and optimization of machinery and devices when surface contact is involved [127].

Adhesion occurs in nearly all practical systems where two solid surfaces are in contact. Adhesion is of importance to friction and wear of materials, especially for contacting components of nano/micro devices in which deformation contribution might be negligible because only light contact force could be involved. For instance, the small-scale contact between smooth surfaces in information storage devices could result in considerable adhesive force, which may play a much more significant role than in conventional tribological processes [9,11]. The adhesive force can be determined using various instruments, such as the surface force apparatus (SFA) and atomic force microscope (AFM) [127].

Intrinsic adhesion may come from various interfacial bonds, such as ionic, covalent, metallic, hydrogen and Van der Waals bonds, which are largely determined by the surface electronic configuration and behavior [17]. The electron behavior of a metal may be characterized by its electron work function (EWF), which is the minimum energy required for an electron to escape from the Fermi level to a point just outside the bulk metal [16,79]. The EWF is one of the fundamental electronic properties of a metallic surface and is related to various properties of metals [81] and semiconductors

[128] as well as many surface processes, such as adsorption, contamination, surface segregation and friction [81,88]. The EWF has also been used for investigation of bio-processes [82]. The EWF can be determined using a Kelvin probe [80]. Recently, EWF has received increasing interest from tribologists. Considerable efforts have being made to explore potential applications of the Kelvin probe in investigation of tribological processes and relevant mechanical phenomena [127].

The adhesive force results from the short-range atom-to-atom interaction, which is mainly controlled by the electronic behavior. Since the EWF reflects the activity of an electron, it should be closely related to the adhesive force. For example, the relationship between electron behavior and surface energy has been described using Miedema's equation [64]. Since the surface energy is directly related to adhesion force [11,62], the correlation between EWF and adhesion could thus be expected. Although there have been many studies on adhesion and EWF, respectively, the correlation between these two properties and their influences on friction behavior of materials have not been well clarified yet [127].

The objective of the work reported in this chapter is to experimentally investigate relationships among the EWF, adhesion and friction behavior of 3d transition metals. The transition metals

and their alloys are widely used for tribological applications [129]. The degree of filling the d-electron band of a transition metal largely affects its physical and chemical properties such as surface energy, Young's modulus, hardness and chemical stability [130-132]. Attempts were also made to understand roles of EWF, adhesion and hardness in governing friction, which is affected not only by adhesion but also by mechanical interaction and deformation behavior of materials [127].

Both EWF and friction measurements were carried out in the ambient environment. It should be pointed out that the EWF measured under the ambient condition is influenced by a possible adsorption layer or oxide film (e.g., passive film), which may make the measured value more or less deviate from the intrinsic electron work function of a metal. The deviation is not large since in the dry ambient environment the oxide file, if exists, may be too thin to effectively block electrons escape from the surface. It is very difficult to determine the EWF of a pure metal since the adsorption or oxide film always exists. Even in vacuum, the oxide film of a sample could be removed before EWF measurement; however, the action of oxide removal or sample preparation in vacuum could introduce surface defects that also affect the EWF measurement. On the other hand, measuring the EWF of a natural surface may not be

regarded as inadequate, since in realistic applications materials are in a natural state and usually used in the ambient environment [133].

3.2 Experimental Procedure

3.2.1 Samples preparation

Materials under the study were 3d transition metals provided by Alfa Aesar and Strem Chemicals Companies (Table 3.1). All metal samples (plates) were annealed in argon atmosphere at temperatures above their recrystallization points for 1 hour and slowly cooled down in furnace. The annealing temperatures for the metals are listed in Table 3.2.

Table 3.1 Composition of the metals

Metal	Ti	V	Cr	Mn	Fe	Co	Ni	Cu	Zn
Purity(%)	99.2	99.5	99	99.9	99.97+	99.9+	99.9+	99.9	99.9+

Table 3.2 Annealing Temperature

Metal	Ti	Fe	Co	Ni	V	Cr	Mn	Cu	Zn
Annealing Temp.(°C)	500				630		390		140

The samples were then lightly polished using a slurry containing aluminum oxide powder (0.05μm). After polishing, the

samples were ultrasonically cleaned in reagent grade acetone (10 min) and reagent alcohol (5 min). All tests were carried on the polished surfaces without etching in order to 1) reduce the probability of formation of surface films, and 2) to minimize the crystallographic influence on EWF. Friction tests were performed under unlubricated condition. The investigation was carried out in ambient environment (22±2$^{\circ}C$, 45±5% relative humidity (RH)).

3.2.2 EWF measurement

The EWF of the specimens was measured using a scanning Kelvin probe (SKP), provided by KP Technology Ltd. (Wick, UK). The SKP system used in this study was developed from a high-resolution static-KP system. The system can control the spacing between its probe tip and a tested surface within 4 nm. During test, a surface under study is scanned by a Kelvin probe line by line over an area of 2×2 mm that covered 10×10=100 points for EWF measurement. Each measured value is therefore an average over 100 measurements, which is statistically more precise than that of the measurement at a single point. The SKP system does not directly provide absolute EWF of a metal but a value relative to EWF of a standard gold sample (5.1 ev) [16,82]. Absolute EWF of a metal sample can be calculated by subtracting its relative EWF value from

the absolute EWF of the standard gold sample. In the present study, a gold tip of 1mm in diameter was used. The oscillation frequency of the SKP tip was 173 Hertz. More information about the SKP system can be found in reference [82].

3.2.3 Adhesion and light-loaded friction measurement

The local adhesion and friction under light loads were measured using an atomic force microscope (AFM) which could also function as a lateral force microscope (LFM) (Digital Instrument, Santa Barbara, CA, USA). The AFM can be used to detect ultra-low forces (less than 1nN) between the AFM tip and a sample surface by measuring the distortion of a flexible cantilever using a laser beam deflection technique (Fig. 3.1) [9,45,134]. A 200 μm long narrow silicon nitride probe with a spring constant of 0.06 N/m was used. The silicon nitride probe consisted of a cantilever with a sharp tip at the end. The nominal tip radius was 20-60nm. For adhesion measurement, the AFM tip moved vertically. The adhesion between the silicon nitride tip and a tested surface was evaluated by measuring the vertical deflection of the cantilever when the tip approached and left the sample surface. Fig. 3.2 illustrates the process of the adhesion measurement. The horizontal distance between points 3 and 7 multiplied by the spring constant of the

cantilever gives the adhesive force [45,50,75,134]. At least five such adhesion measurements were performed on each specimen.

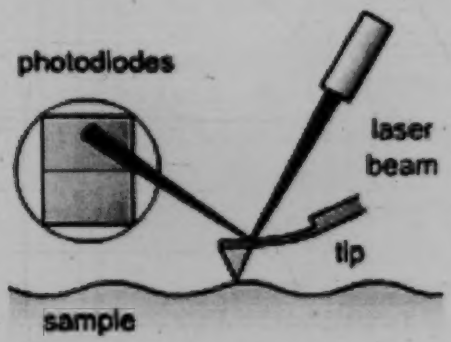

Figure 3.1 Distortion of cantilever measured by laser beam deflection technique in AFM.

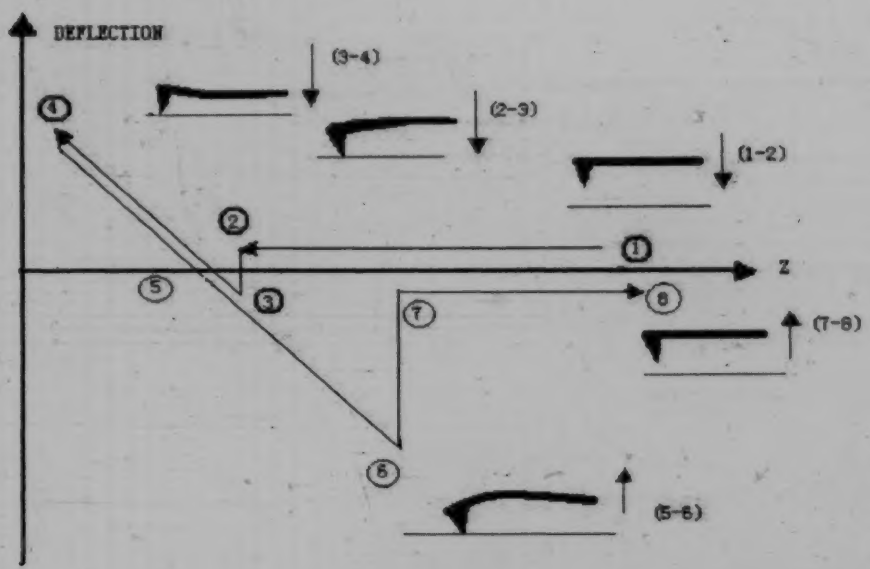

Figure 3.2 The curve of deflection versus displacement (Z) of cantilever when the AFM tip is approaching and leaving a sample surface. A recorded deflection vs. Z curve is also presented in the same figure.

In Fig. 3.2,

1-2: The AFM tip is pushed by the cantilever towards a sample surface

2-3: The tip is pulled down by an attractive force from the sample surface;

3-4: The cantilever is bent up as the tip touches the surface under an applied force;

5-6: The tip is attracted by the adhesive force when pulled away from the sample surface;

6-7: The tip escapes from the surface when the external force exceeds the adhesive force, which can be determined if the spring constant of cantilever is known;

7-8: The tip moves away from the sample surface.

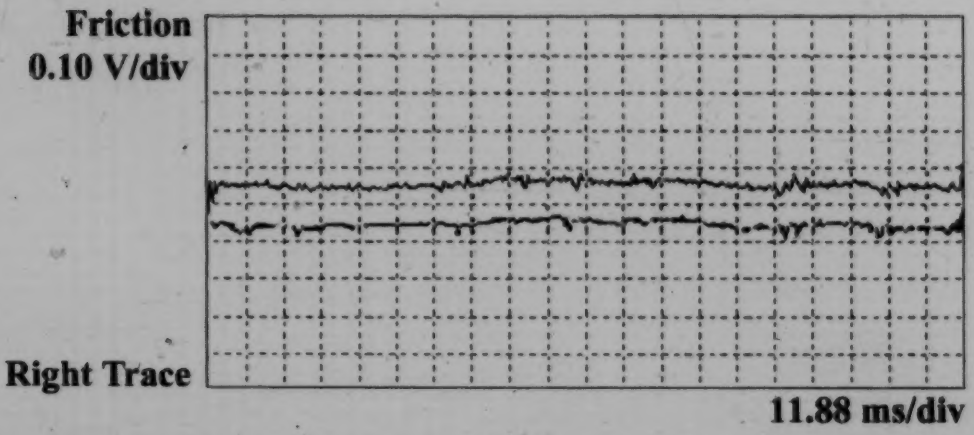

Figure 3.3 Friction trace and retrace, determined by AFM.

For friction measurement, a surface area of 1μm^2 was scanned by the AFM/LFM tip with cantilever scanning laterally. As the tip moved on a surface, the frictional force resulted in torsion of the cantilever on which the probe was mounted. The torsion of the cantilever was proportional to the frictional force between the tip and the surface. The relative frictional force was estimated from the friction traces (Fig. 3.3). The vertical axis represents the differential signal from two photodiodes, while the horizontal axis represents the tip position along the fast scan direction. The larger the distance between the friction trace and the retrace, the larger the frictional force [135]. The average value of this distance (TMR) may therefore be used to evaluate the friction behavior. Roughness of the tested area was simultaneously determined using the AFM.

3.2.4 Friction under higher loads

Coefficients of friction of the metals under a sharp tip were also measured using a universal micro-tribometer (UMT) provided by CETR, California, USA. The tribometer has a mechanical probe made of tungsten carbide (radius: 25μm). Single-pass sliding tests were performed under a series of constant loads from 1 to 5 mN at a velocity of 3 mm/min. The sliding distance was 6mm. Both normal load (L) and frictional force (F) were measured during the single-

pass sliding process. The friction coefficients ($\mu = F/L$) of the transition metals were obtained by averaging 3-5 measurements. Fig. 3.4 shows the UMT system.

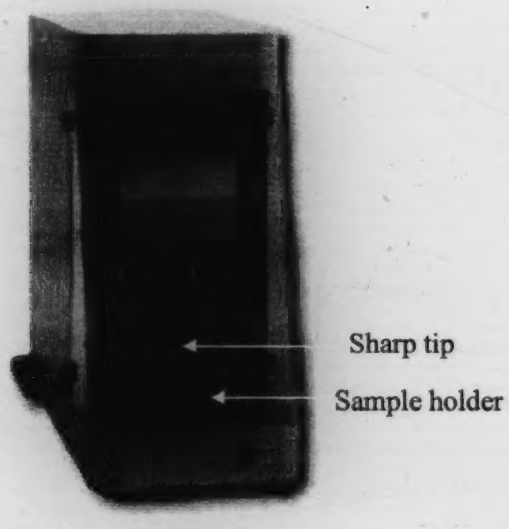

Figure 3.4 CETR universal micro-tribometer (UMT) system.

3.2.5 Hardness measurement

Surface mechanical properties were evaluated using a micro-mechanical probe (Fischer Technology Inc., Windsor, CT, USA). The technique is based on Vickers indentation, which provides information on local hardness and elastic behavior. A standard Vickers diamond indenter was employed, which has the shape of square-based pyramid with an angle of 136° between opposite

faces. The micro-indentation test was performed under a maximum load of 300 mN. An entire loading and unloading process was recorded automatically, resulting in a load-depth curve. Hardness values were determined from the load-depth curve [136] by averaging 5 measurements for each target metal. Fig. 3.5 presents a typical load-depth curve [137]. Hardness (H) is the ratio of the maximum indentation force to the contact area of the indentation under a certain load and may be expressed as [138]:

$$H = \frac{L}{A_s(x)} = \frac{L}{26.43x^2} \qquad \textbf{(3.1)}$$

where L is the test force (N), $A_s(x)$ is the surface area of the indentation and x is the depth of penetration (mm).

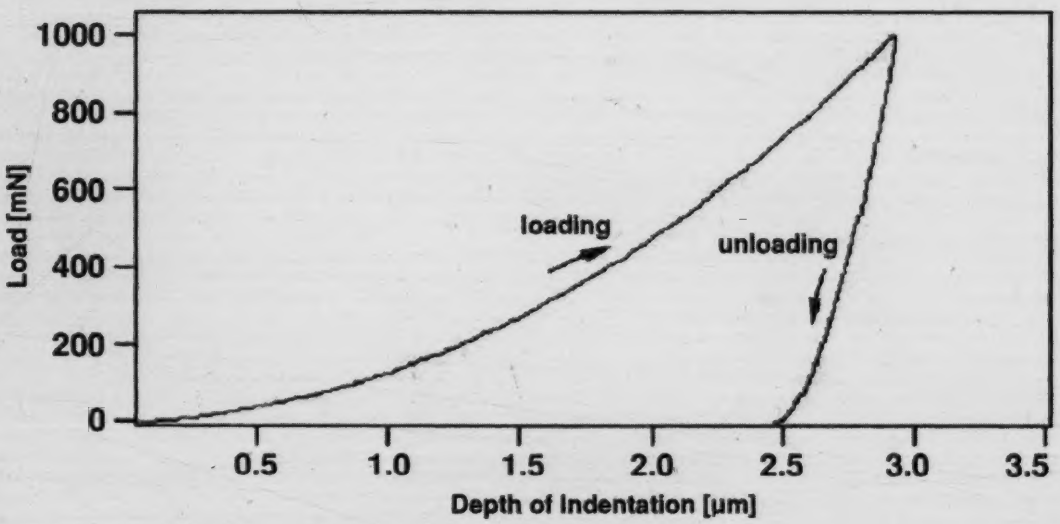

Figure 3.5 A typical load-depth curve from micro-hardness test [137].

3.3 Results and discussion

3.3.1 Electron work function

The EWF of transition metals is of interest, since it can be used as a parameter for surface characterization of the metals. However, experimental work function values reported in literature are rather scattered because of the high sensitivity of EWF to the surface condition that is influenced by the sample preparation procedure [139]. The EWF of transition metals has also been calculated using various theoretical methods [81,89,139]. Despite relatively large data scattering of reported EWF values, the periodicity of EWF for transition metals was clearly demonstrated by various researchers [81,87-89].

Atomic surface density or the degree of surface packing influences the EWF [11,75]. In this work, polished surfaces of the transition metals were analyzed, so that influences of the crystallographic orientation and possible oxide films on EWF could be minimized. Or in other words, the measured EWF more reflected the intrinsic chemical behavior when the crystallographic influence is minimized. Results of the EWF measurement are presented in Fig. 3.6. EWF values determined in the present study are about 25% lower than those calculated using the *ab initio* approach [81]. This is

understandable, since the calculations were carried out for the most close-packed crystallographic planes which have the highest work function. The data were also about 10% lower than the reported EWF values of polycrystalline transition metals, bearing in mind that plastic deformation introduced by polishing could decrease EWF [93,113,124]. Regarding the trend of the variation in EWF with elements, the present experiment results are consistent with data reported in literature.

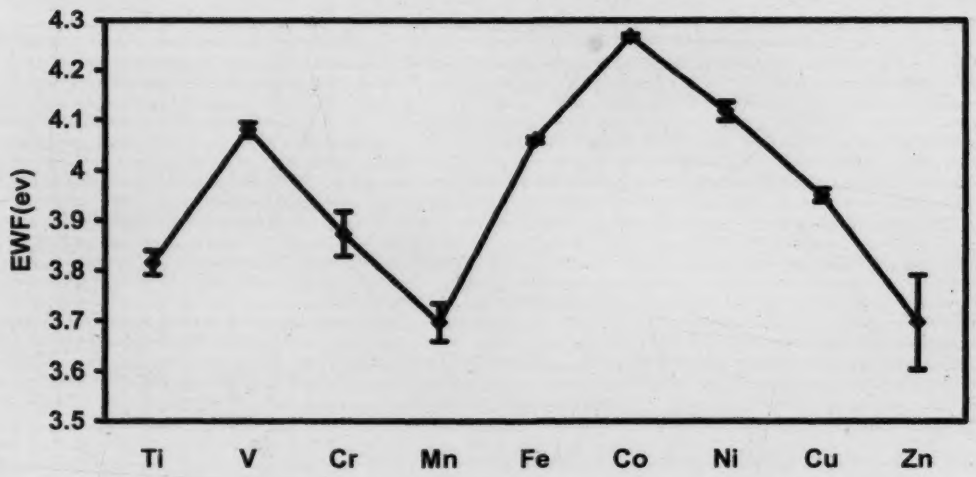

Figure 3.6 Electron work function of 3d transition metals [127].

3.3.2 Adhesion measurement using AFM

The adhesion behavior of the transition metals was evaluated using AFM. It is known that real contact area, which is affected by hardness and applied load, has great influence on surface adhesive interaction. However, when the adhesive force was measured with AFM on a small scale, the influence of surface roughness could be minimized and the measured should be closer to intrinsic adhesion. This is reasonable since the radius of the tip is 20-60 nm which is much smaller than the radii of asperities that are usually in the range of 100-200nm.

Microstructure and crystal structure can affect adhesion. As mentioned earlier, for a polished surface the crystallographic influence was minimized so that the determined adhesive force is more a measure of the atomic interaction, largely depending on the electronic configuration of the tested metal.

The interaction between the silicon nitride AFM tip and the metals may involve electrostatic and Van der Waals forces. The humidity also influences the interaction [6,134,135]. Surface electron behavior certainly affects the forces, so that the EWF should be a parameter reflecting the adhesive interaction or force. Magnitudes of adhesive force of the transition metals under study are shown in Fig. 3.7. Comparing Fig. 3.6 (EWF) with Fig. 3.7 (adhesive force), one may see a clear correlation between adhesion

and EWF. As demonstrated, the higher the EWF, the lower the adhesion. It has been shown that the adhesion between transition metals and ceramics is mainly related to the relative chemical activity of the metals [11,140], which may be characterized by their EWF. Therefore, higher EWF may correspond to lower activity and thus lower adhesion. Such correlation is consistent with previous observations [75].

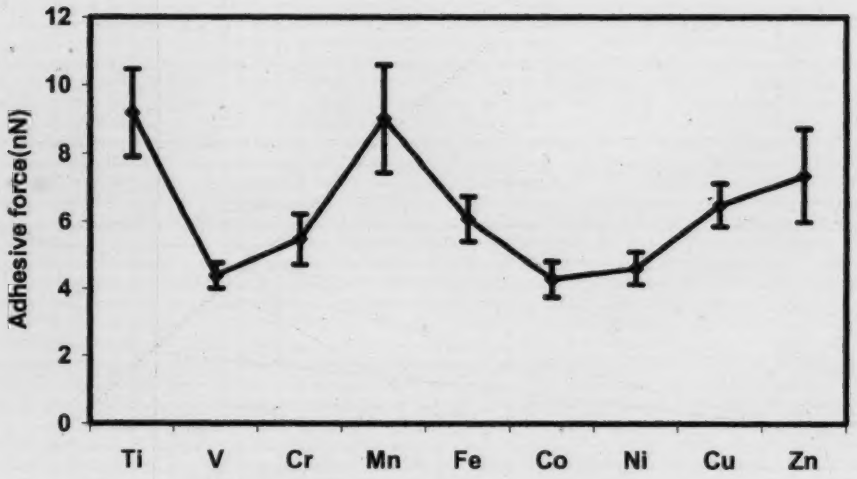

Figure 3.7 Adhesion force between 3d transition metals and a Si_3N_4 tip in AFM [127].

The tip radius and humidity may influence the adhesion and friction measurement [50,134]. Since our study on different metals were carried out in the same ambient environment using the same

tip, the effects of humidity and tip radius on the determined trend of variations in adhesion for the transition metals could be negligible or minimized.

3.3.3 Friction measurement using AFM/LFM

The friction behavior of the transition metals under light loads was evaluated using the AFM/LFM. For friction measurement, the AFM tip slid on a sample surface over a micro/nano scale area. The torsion of cantilever was very sensitive to the interaction between the tip and the sample surface. The AFM/LFM could be used to measure surface structural variation and to identify different chemical species. This technique has been widely applied for nano-tribological studies [9,45,50,134,141-146].

Since the surface roughness influences the friction measurement, the roughness of target surfaces under study was determined using AFM/LFM and is presented in Table 3.3. Root mean square (RMS) was used to represent the roughness. As shown, there is no large difference in roughness among the metals. Therefore, during the friction measurement, the tip-sample contact area could thus be considered the same for all the metals under a light contact force.

Table 3.3 Surface roughness

Metals	Ti	V	Cr	Mn	Fe	Co	Ni	Cu	Zn
RMS(Rq)(nm)	4.241	5.256	3.682	4.481	4.536	5.023	4.123	4.397	7.152

Fig. 3.8 illustrates the magnitude of friction force for the transition metals during the lateral force friction measurement. The friction behavior of the transition metals is consistent with their adhesion behavior (Fig. 3.7). As illustrated, the higher the adhesive force, the larger the frictional force. It is evident that under light loads, for smooth surfaces, the friction is dominated by adhesion that is governed by the electronic behavior as characterized by the EWF.

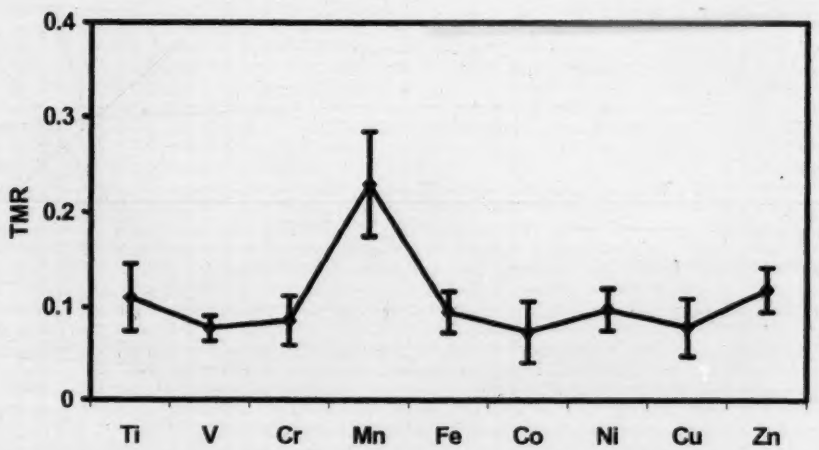

Figure 3.8 Friction of 3d transition metals under a light load (between 0 and 50 nN) [127].

As mentioned earlier, the frictional force results from two main sources. One is the adhesive force (F_{adh}) from chemical interaction and the other is mechanical interaction (F_{def}) involving asperity-plowing and surface deformation [1-3,11]. Since all samples has similar roughness and the AFM/LFM friction measurement was carried out under ultralow load, the friction force was thus mainly affected by the adhesive force between a specific sample and the AFM tip, which was directly related to EWF.

3.3.4 Friction behavior under larger loads

As demonstrated, friction of the transition metals under light loads was greatly dependent on their adhesion behavior. However, for many cases, the normal load is not small and contribution of F_{def} becomes larger [1-3,11]. In order to better understand the frictional behavior of the transition metals, their friction behavior under larger contact forces was also investigated using a sharp tip (micro tribometer) under higher loads.

Friction coefficients of the transition metals were determined using the sharp tip during a single-pass sliding processes under a normal load of 1 mN. Results of the sharp-tip friction measurement are presented in Fig. 3.9. Comparing the measured friction coefficients of the transition metals with their EWFs (Fig 3.6) and

adhesion (Fig 3.7), one may see almost no correlation between the friction coefficients and the adhesion behavior or EWF of the metals. Similar friction behavior was observed when the normal load was further increased. It was demonstrated that under relatively high loads, the adhesion force became less important. In this case, the mechanical action dominated the friction process and the mechanical behavior of the metals could therefore play a major role in determining the frictional behavior.

In order to see how the friction behavior was affected by mechanical behavior, hardness of the 3d transition metals was determined using a micro-mechanical probe (FischerScope) and their hardness values are presented in Fig. 3.10. Comparing with Fig. 3.9 (coefficients of friction), one may see that harder metals showed lower coefficients of friction. Such a relationship is consistent with conventional friction law: $\mu = s/H$ (equation 2.12), where s is shear strength of the material, and H is hardness of the material [2,13]. A hard metal had higher resistance to penetration and thus reduced the plowing effect, leading to lower friction. In addition, when a surface was harder, the contact area was reduced, leading consequently to reduced adhesive force.

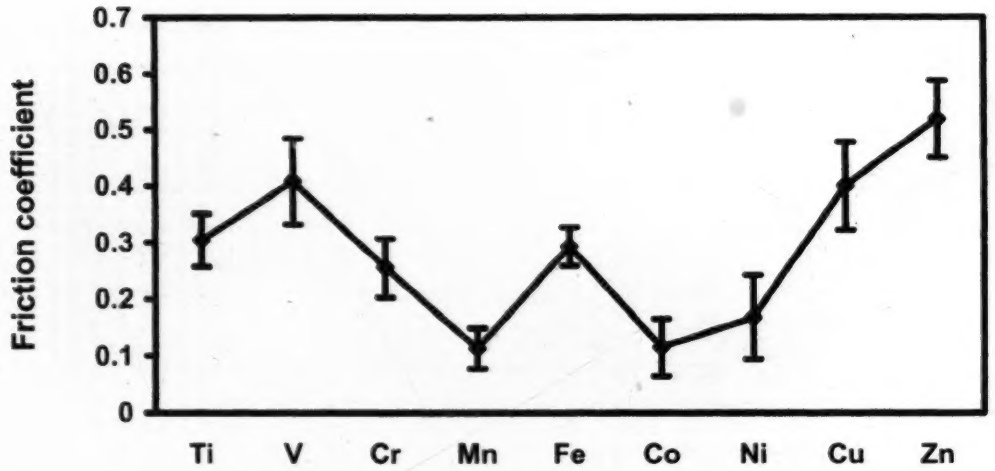

Figure 3.9 Friction coefficient of 3d transition metals under 1 mN load [127].

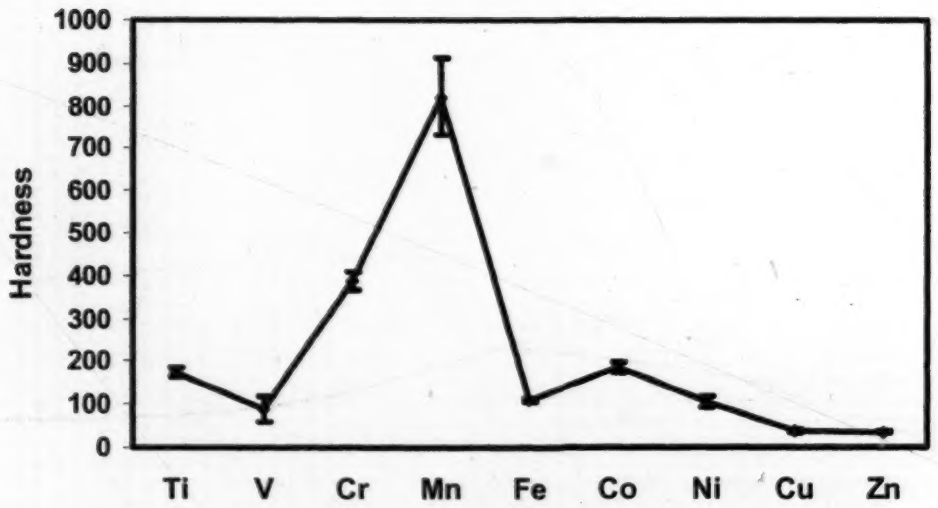

Figure 3.10 Micro-hardness of 3d transition metals [127].

3.4 Summary

The electron work function (EWF) of 3d transition metals and the adhesion between an AFM silicon nitride tip and surfaces of the transition metals were measured, respectively. Results of the measurements demonstrated unambiguous correlation between these two properties: the lower the EWF, the higher the adhesion. As a result, a smooth metal surface having lower EWF showed a larger frictional force when tested under light loads. Such correlation is of particular importance to nano/micro devices in which adhesion may dominate the friction behavior of various dynamic components. This study has also demonstrated that the Kelvin method is promising for characterization of adhesion and investigation of relevant tribological phenomena on small scales under light contact forces.

The friction measurement with a sharp tip demonstrated that mechanical properties played a more important role than adhesion under larger contact forces when the mechanical interaction became predominant. In this case, harder metals showed lower friction.

Chapter 4 : Metal-Metal contact: adhesion and friction between 3d transition metals

The correlation among EWF, adhesion and friction is further studied by investigating the friction between two transition metals.

In this study, the metal-metal friction under light loads was evaluated employing a micro-tribometer. It was demonstrated that adhesion and friction of the transition metals under light loads were closely related to their EWFs. The adhesion between two metals in contact could be expressed as a function of their EWFs and electron densities. Consequently, the friction between the two metals under light loads could be estimated based on these two parameters [147].

4.1 Introduction and objective

Adhesion and friction between metallic materials are of importance to many dynamic mechanical systems, particularly to those at nano- or micro-scales. Considerable efforts have been made to fundamentally investigate adhesion and friction between two metals using experimental and theoretical approaches. Correlating experimental data of adhesion and friction to various material properties such as chemical reactivity, metallurgical

compatibility, d-valence bond character and electron work function is certainly an area attracting extensive attention [11-13,33,34,127]. Many researchers are also engaged in study of adhesion and friction on atomic level using computational techniques [18,57,148,149]. Investigation of adhesion and friction by means of contact mechanics is another important area, in which a number of models have been proposed to simulate contacting processes involving friction [20,21,26,150]. Despite the numerous efforts made to understand adhesion and friction between two metals, clear correlation between adhesion of metals and their fundamental properties, e.g. the electron behavior, has not yet been established. Different mechanisms have been proposed regarding the adhesion between two metals; it is without doubt that the intrinsic adhesion largely depends on the surface electronic configuration and properties. The electron behavior of a metal can be characterized by its EWF, the minimum energy required for an electron to escape from the Fermi level to a point just outside the bulk metal [147].

Metal-metal contact is more complicated than metal-ceramic contact. Ceramic is relatively inert, so the EWF of the metal largely determines the adhesion and friction for the metal-ceramic contact. However, when two metals are brought into contact, electrons would flow from one metal to the other having a lower Fermi energy,

resulting in a dipole layer at the interface, which produces an electrostatic potential that will align the Fermi levels of the two metals [65,109]. As a result, the adhesion and friction are largely affected by the EWFs of both the metals in contact [147]. Fig. 4.1 illustrates the equilibrium of the Fermi energies when two metals are put in contact.

Transition metals and their alloys are widely used in engineering practice, often involving dynamic metal-metal contact [129]. The interaction between transition metals is more complicated than simple metals because of their complex electronic configurations [149]. The adhesion behavior of transition metals is a topic of both practical and theoretical interest.

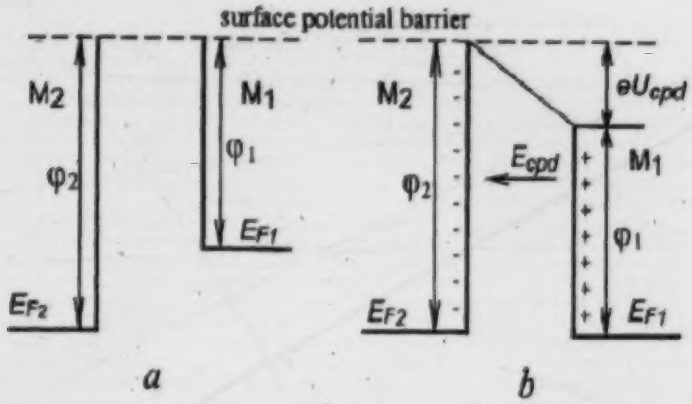

Figure 4.1 Contact phenomena of two metal plates (a) Fermi energies are different before equilibrium (b) Fermi energies are equal after equilibrium [74].

The objectives of this work were to 1) measure the friction between 3d transition metals and an iron plate; 2) investigate the relationship between the EWF and adhesion as well as friction for 3d transition metals. A semi-empirical approach was used to establish the relationship. Due to the difficulty in direct determination of adhesion between the metals, in this work, friction was used as a parameter to evaluate the adhesion behavior. This is acceptable when the contact load is light. It is known that the friction force is the summation of two contributions: the adhesive force and the deformation force. The ratio of these two contributions varies with the contact condition especially the contact force. Our previous study has demonstrated that under light load adhesion plays a predominant role in controlling the friction force [127].

4.2 Friction measurement

4.2.1 Samples preparation

Materials under the study were 3d transition metals provided by Alfa Aesar and Strem Chemicals Companies. The compositions of the samples were listed in Table 3.1. All metal samples (plates) were annealed in argon atmosphere at temperatures above their recrystallization points for 1 hour and slowly cooled down in the

furnace. The annealing temperatures for the metals were listed in Table 3.2.

The samples were then lightly polished using a slurry containing aluminum oxide powder (0.05μm). After polishing, the samples were ultrasonically cleaned in reagent grade acetone (10min) and reagent alcohol (5min). All tests were carried out on the polished surfaces without etching in order to reduce the probability of forming surface oxide, as well as to minimize the effect of crystallographic orientation on friction measurement. The time interval between sample preparation and the test was less than 3 min. Friction tests were performed under unlubricated condition in ambient environment (22±2$^{\circ}C$, 45±5% relative humidity (RH)).

4.2.2 Friction measurement

Friction coefficients of the metals in contact with iron were measured using a universal micro-tribometer (UMT) provided by CETR (California, USA). Fig. 4.2 schematically illustrates the friction apparatus. Efforts were made to carefully arrange the target surface and the counter-face parallel to each other. Before the friction test, a small plate of iron with dimensions 4×4×1.2 mm slid (reciprocating) on the surface of a large target sample metal under a load of 40 mN for 6 passes. The sliding distance was 6 mm for

each pass at a sliding speed of 4 mm/s. The purpose of the reciprocating sliding process was to remove a possible oxide scale or adsorption layer on sample surface. Single-pass sliding tests were then performed under different constant loads from 1 to 40 mN at a sliding speed of 3 mm/min over a sliding distance of 6 mm. Friction measurements were carried out at different positions of the same sample in order to obtain average values. Both normal load and frictional force were measured during the single-pass sliding process. Friction coefficients of the transition metals against iron were determined by averaging at lease three measurements.

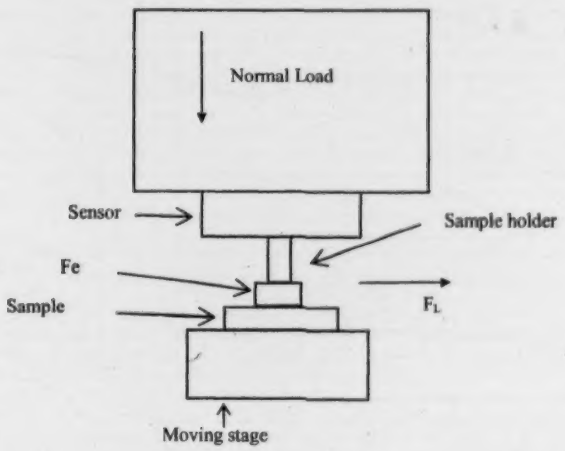

Figure 4.2 Schematic illustration of the friction apparatus. The iron plate was glued to the sample holder [151].

4.3 Results and Discussion

4.3.1 Friction measurement under light loads

Adhesion and friction of metals largely depend on the surface condition and the contact load [152]. Surface contamination by water, gases and oxides, which are unavoidable in ambient environment, could be a major barrier to the intrinsic adhesion of metals [11,152]. In the present friction measurement, in order to eliminate the barrier and achieve metal-metal contact, the top sample slid (reciprocating) on the bottom sample under 40 mN before the test was started. Such pre-rubbing process could remove possible surface films to minimize non-metallic contact [21,32,34,153]. Fig. 4.3 illustrates friction coefficients measured with and without the pre-rubbing process for a Fe-Fe pair. Other metal pairs also showed a similar trend. As shown, pre-rubbing resulted in higher friction coefficients, which implies that the rubbing process could maximize the metal-metal contact. It should be mentioned that the increase in friction caused by pre-rubbing may not attribute to changes in roughness and dislocations resulting from this process, since the original surfaces were already polished and there was no significant change in surface roughness observed after the pre-rubbing process [151].

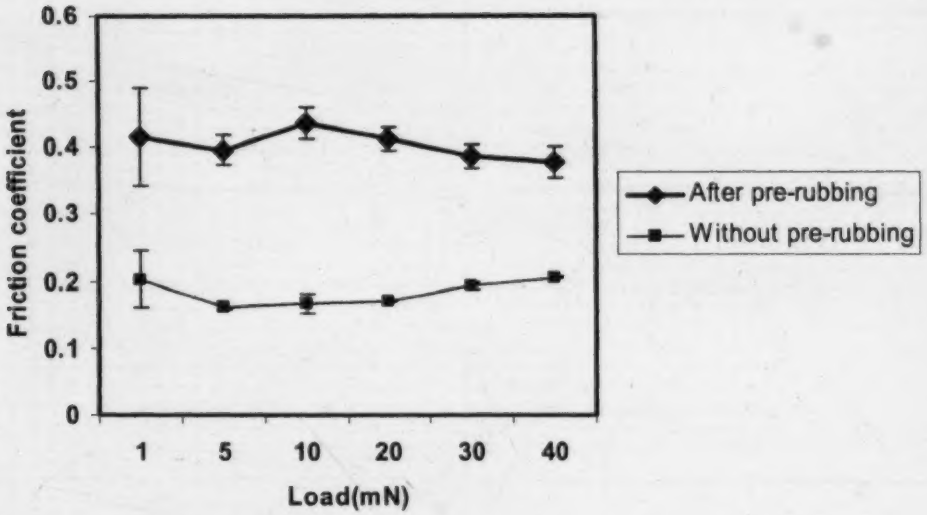

Figure 4.3 Friction coefficient of Fe-Fe pairs (polished) measured with and without pre-rubbing, respectively [151].

Microstructure and crystal structure certainly affect adhesion. As mentioned earlier, for a polished surface, the orientation effect could be minimized so that the determined adhesive force was more a measure of the atomic interaction, which largely depended on the electronic configuration of the tested metal [147].

With this pre-rubbing treatment, friction coefficients of all 3d transition metals in contact with iron under a load of 30 mN were measured. This load resulted in a small contact stress for a nominal contact area of 4×4 mm^2 (i.e. the surface area of the iron plate). Results of the friction measurement are illustrated in Fig. 4.4.

Comparing with previously reported EWFs of the metals (Fig. 4.5) [95] and our experimental results presented in Chapter 3 (Fig. 3.6) [127], there is no obvious relationship between EWFs of the individual metals and the measured friction coefficients. This is understandable, since in the present case, the adhesion and thus friction between two different metals under a light contact force are affected by the EWFs of both metals in contact. In order to explain the adhesion between two different metals based on their electronic behaviors, the adhesion between the two metals and their EWFs needs to be correlated [147].

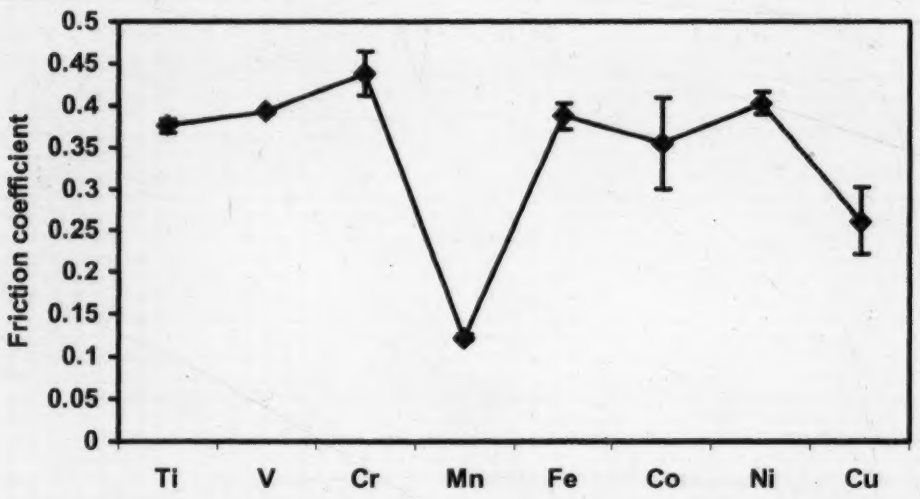

Figure 4.4 Friction coefficients of 3d transition metals in contact with iron (under 30 mN) [147].

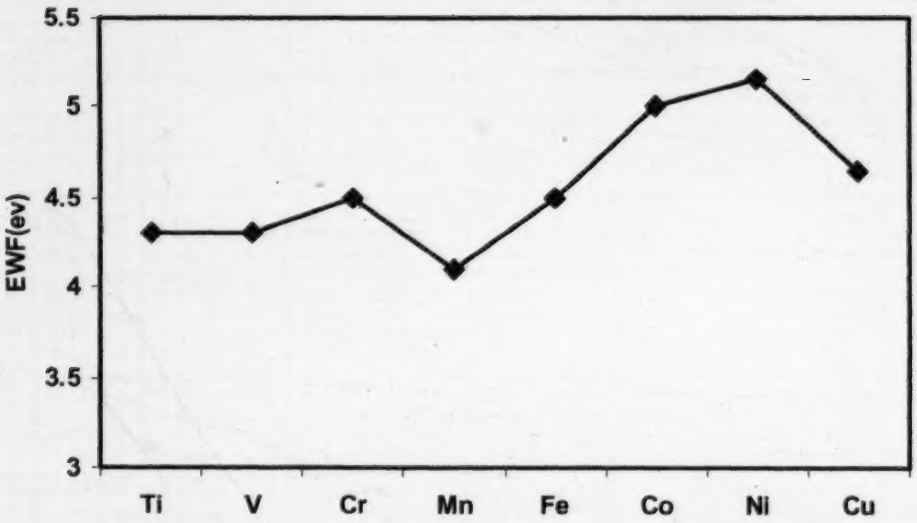

Figure 4.5 EWFs of 3d transition metals from ref.95 (Miedema's data) [95].

4.3.2 Theoretical consideration

When two surfaces are brought into contact, the adhesion or the pull-off force is usually analyzed in terms of surface energy rather than the force [24]. Surface energy is an important property of materials: the energy required to form a surface, and is therefore closely related to the cohesive energy [11]. The surface energy is largely determined by the surface electronic configuration [11,33,81]. Many models have been proposed to predict surface energies of solid surfaces [11,100,101]. Miedema [64] suggested an equation to relate the surface energy of a metal to its electronic

properties, which has received experimental and theoretical support [81,154]. This semi-empirical equation has the following form [64]:

$$\gamma = n_{ws}^{5/3} / (\varphi^* - 0.6)^2 \qquad \textbf{(4.1)}$$

where γ is the surface energy of a metal at $0K$; n_{ws} is the electron density at the boundary of the Wigner-Seitz cell; φ^* is a parameter approximately equal to EWF of a metal and related to its electronegativity [64,95,97-99,155].

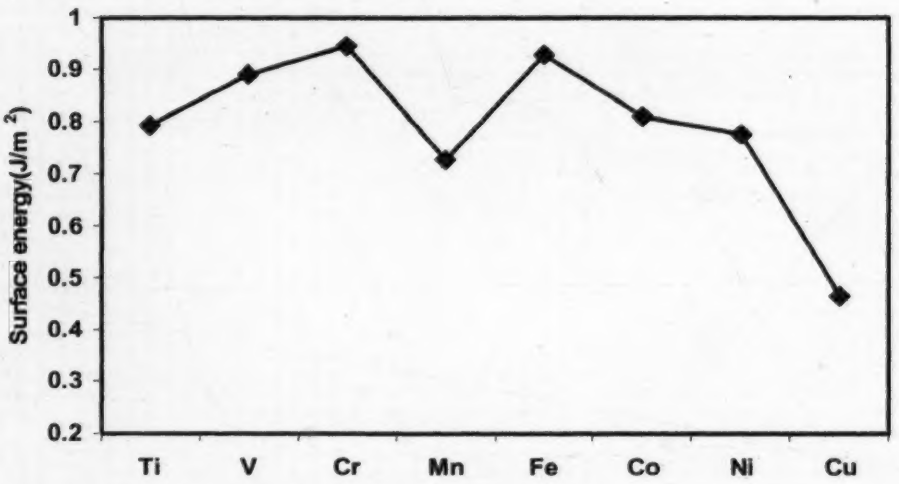

Figure 4.6 Surface energy calculated using equation (4.1).

This semi-empirical equation suggested by Miedema includes EWF and electron density, which has also been applied in analyzing the heat of formation of solid alloys [95,98]. These two parameters are properties of pure metals and related to the strength of metallic

bonds. When two metals are brought into contact, electrons will flow from one metal to the other with a lower Fermi energy, resulting in a dipole layer at the interface [65,109,149,156]. In addition to the reconstruction of the Fermi surface at the interface, the electronic density must be continuous at the boundary between two corresponding Wigner-Seitz cells [95,97]. Therefore the interaction between the two metals is related to the differences in both EWF and the electron density between the two metals. For a metal in vacuum, its surface energy is only determined by the EWF and electron density of the metal [64]. Fig. 4.6 presents surface energies of 3d transition metals, calculated using equation (4.1). The incorporation of EWF into surface energy calculation can also be found in other models [100,101].

In order to separate two bonded surfaces (per unit area), a minimum energy i.e. the adhesion energy is required [13,34]. The adhesion energy (W_a) for a pair of metals, 1 and 2, may be expressed as a function of surface energies, γ_1, γ_2, of the metals A and B and the interfacial energy γ_{12} (equation (4.2)). The latter is the summation of the average interfacial configuration energy (γ^{geom}) and the chemical interaction energy (γ^{chem}) of the two metals (equation (4.3)) [62,63]:

$$W_a = \gamma_1 + \gamma_2 - \gamma_{12} \quad \textbf{(4.2)}$$

$$\gamma_{12} = \gamma^{chem} + \gamma^{geom} \quad \textbf{(4.3)}$$

The average interfacial configuration energy is approximately expressed as [62,63]:

$$\gamma^{geom} = 0.15(\gamma_1 + \gamma_2) \quad \textbf{(4.4)}$$

So the adhesion energy may be represented as:

$$W_a = 0.85(\gamma_1 + \gamma_2) - \gamma^{chem} \quad \textbf{(4.5)}$$

Since γ^{chem} is a relatively small contribution to the total adhesion energy, it may be ignored in approximate calculations [63].

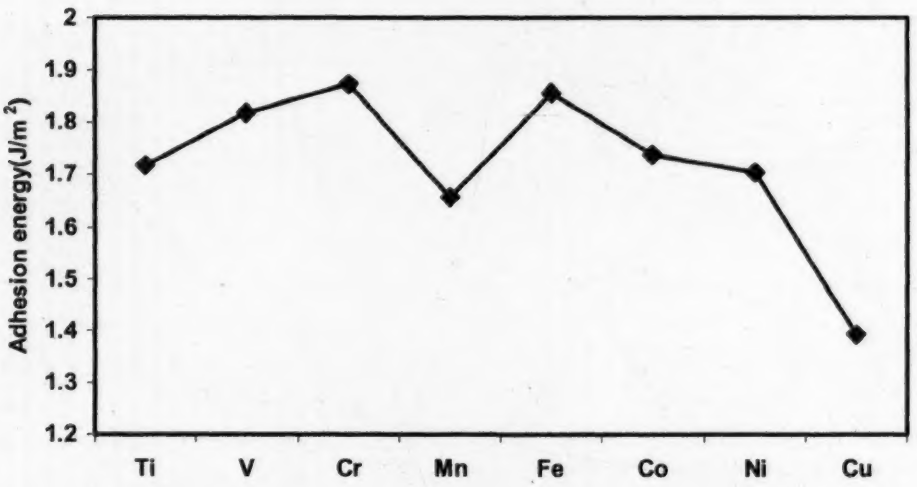

Figure 4.7 Adhesion energy for 3d transition metals in contact with Fe calculated using equations (4.1) to (4.5).

If EWF and n_{ws} are known, the adhesion energy for a pair of metals can be calculated based on equations (4.1) and (4.5). Fig. 4.7 presents the result of such calculated adhesion energies between Fe and 3d transition metals. The values of EWF and electron densities come from references [155].

4.3.3 Further discussion

As indicated earlier, frictional force results from two main sources. One is the adhesive force (F_{adh}) from the chemical interaction and the other is the mechanical force (F_{def}) involving asperity-plowing and deformation [1-3]. Under low loads, F_{adh} plays the main role in generating the frictional force, while under high loads F_{def} becomes predominant.

Our previous work [127] demonstrated variations in friction between a sharp ceramic tip and 3d transition metals with respect to the load. Under light loads, friction was largely contributed by adhesion; while under relatively high loads, the friction coefficient was mainly determined by the hardness of the metals. The friction coefficient of the 3d transition metals in contact with Fe under 30 mN (Fig. 4.4) shows no correlation with the hardness of the metals (Fig. 3.10), so the plowing effect should not be dominant. Besides, fairly good agreement between the friction coefficients (Fig. 4.4)

and calculated adhesion energies (Fig. 4.7) was observed. Therefore, it is believed that in the present study, 30 mN was low enough to have the friction dominated by adhesion between two metal samples with apparent contact area equal to 4×4 mm^2.

In addition, previous studies on friction of 3d transition metals using atomic force microscope [127] showed that adhesion played a predominant role when a metal sample was in contact with a moving ceramic tip (radius: 20–60 nm) under a load within 50 nN. Assuming that the contact area was $\pi a^2 = \pi(40nm)^2$ under a load of 50 nN, one may find that the contact stress was approximately equal to $50nN/\pi(40nm)^2 \approx 1\times10^{-2} nN/nm^2$. This contact stress is much larger than the contact stress used in the present study. In the present friction measurement, the contact force was 30 mN and the apparent contact area is 4×4 mm^2, which resulted in a contact stress in the range of $2\times10^{-6} nN/nm^2$. This estimation may further support the argument that the measured friction in this study was mainly contributed by adhesion.

According to the definition of adhesion energy, the work required to separate two bonded surfaces is equal to the adhesion energy multiplied by the real contact area [13,34]. The real contact area is affected by mechanical properties of the two contacting

solids and the applied load [2,13,17]. For the present friction measurements, the top sample (Fe) had the same apparent surface area. Under low loads, the influence of hardness on the real contact area could be negligible. Or in other words, the real contact area may be roughly the same for all target metals, so the magnitude of adhesion energy should reflect the adhesion between a pair of metals. Therefore, the frictional force determined under low loads mainly results from adhesion and may thus be predicted based on EWFs and electron densities of two metals in contact. Comparing the measured friction coefficients of the 3d transition metals in contact with Fe under 30 mN (Fig. 4.4) with the calculated adhesion energies (Fig. 4.7), one may see that these two parameters are basically consistent, although minor discrepancy exists. For example, the calculation (Fig. 4.7) indicates that the Fe-Cu contact should have a lower friction coefficient than the Fe-Mn contact, which is different from that experimentally determined (Fig. 4.4). The difference may be explained by considering the fact that Mn is much harder than Cu [127,157] so that the true contact area of the Fe-Mn contact is smaller than that of the Fe-Cu contact [2], thus leading to a lower friction coefficient for the Fe-Mn contact.

In this study, the surface energy was used to connect metal-metal adhesion to the EWF and the electron density. Although the

relation between surface energy and the electron behavior is very complicated, such a relation may, however, be described using a simple semi-empirical equation such as equation (4.1), which makes it possible to predict, quickly and approximately, the adhesion between a pair of different metals based on their electronic properties.

For metal-ceramic adhesion and friction presented in Chapter 3, the trends of adhesion and friction are not consistent with the trend of surface energies of metals (Fig. 4.6). The possible reason is that interfacial energy (γ_{12}) of metal-ceramic contact makes greater contribution to the adhesion energy than that of metal-metal interfacial energy. This may make the trend of metal-ceramic adhesion energy not to have the same trend as the surface energies of the metals.

4.4 Summary

Friction between iron and 3d transition metals under low loads were investigated. Efforts were made to correlate the electron work functions of the metals with their adhesion and thus friction between the 3d transition metals under light loads. It was demonstrated that the adhesion and friction between two metals under light loads could

be predicted based on their electron work functions and electron densities.

The correlation among adhesion, EWF and electron density is of importance to materials selection and friction control for nano/micro devices in which friction is dominated by adhesion.

Chapter 5 : An energy consumption model for metal-metal adhesion and friction

This chapter reports a study on metal-metal adhesion and friction under light load from an energy balance perspective. An energy consumption friction (ECF) model was proposed to calculate friction coefficients of transition metals in contact. In this model, elastic contact between two metals is assumed when calculating adhesion energy and deformation energy as two metals slide on each other. Moreover, the adhesion energy between two contacting metals is calculated based on more concrete physical concepts.

Friction coefficients of 3d transition metals in contact with Zn were measured using a micro-tribometer. It was demonstrated that friction coefficients of 3d transition metals in contact with Zn predicted using the model was consistent with experimental observations under low contact loads. The study showed that adhesion dominated friction under light loads [151].

5.1 Introduction and objective

In our previous studies presented in Chapter 4 [147], Miedema's empirical equations of surface energy and adhesion energy were used to establish the correlation between EWF and

metal-metal adhesion as well as friction under light loads. However, in the empirical equations, the exponents of EWF and electron density were obtained by fitting the semi-empirical model to the surface energies of solid metals, which were extrapolated from liquid metal data [64]. The fitted exponents do not have clear physical meaning. Besides, the relationships between some parameters, e.g. electronegativity and EWF, are not well defined [64]. Therefore, the fundamental correlation between EWF and adhesion cannot be quantitatively established with the semi-empirical model.

Various computational techniques have been used to attack adhesion problems. For instance, Rose et al.[55,56] suggested that the adhesive binding energy of different metals against the separation could be scaled into a single universal curve. Ferrante et al. [57] calculated the binding energy using a quantum mechanical jellium model for a number of simple metals in contact. Smith et al. [58,59] calculated the binding energy for transition metals interfaces using a more complete quantum mechanical formalism. These studies shed light on the nature of fundamental interatomic interactions and provide quantitative adhesion energies for some metal pairs. However, these model calculations are so complicated that they are hard for non-specialists to comprehend and are difficult to be applied to predict general metal-metal interactions.

The application of these approaches is therefore rather limited. Thus, an easy to use but fundamental model for quantitative prediction of metal-metal adhesion and friction under light loads is demanded to support tribological and nanotribolgical research and practice.

The objectives of this work were to 1) measure the friction between 3d transition metals and a zinc plate; and 2) establish a fundamental and feasible energy consumption friction (ECF) model for predicting metallic friction under low loads based on the surface electron behavior and mechanical properties. The former governs the adhesive force while the latter determines the contact area and deformation of two metals under a certain contact condition. This model assumes elastic contact between two metals in contact and the calculation includes adhesion energy and deformation energy when the two metals slide on each other. The purpose of doing a new set of friction measurements was to provide more experimental data to evaluate the proposed ECF model [151].

5.2 Experimental procedure

The samples were 3d transition metals provided by Alfa Aesar and Strem Chemicals Companies (Table 3.1). All metal samples (plates) were annealed in argon atmosphere at temperatures above their recrystallization points for 1 hour and slowly cooled down in

the furnace. The annealing temperatures for the metals are listed in Table 3.2. The samples were then polished and ultrasonically cleaned using the same procedures as described in Chapter 4.

Friction coefficients of the metals in contact with zinc were measured using a universal micro-tribometer (UMT) provided by CETR (California, USA). The friction apparatus is illustrated schematically in Fig. 4.2. Efforts were made to carefully arrange the target surface and the counter-face parallel to each other. Before the friction test, a small plate of zinc with dimensions 4×4×1.2 mm slid (reciprocating) on the surface of a large target sample metal under a load of 40 mN for 6 passes. The sliding distance was 6 mm for each pass at a sliding speed of 4 mm/s. The purpose of the reciprocating sliding process was to remove a possible oxide scale or adsorption layer on the sample surface. Single-pass sliding tests were then performed under different constant loads from 1 to 40 mN at a sliding speed of 3 mm/min over a sliding distance of 6 mm. Friction measurements were carried out at different positions of the same sample in order to obtain an average value. Both normal load and frictional force were measured during the single-pass sliding process. Friction coefficients of the transition metals against zinc were determined by averaging at least three measurements to ensure the consistency of the friction measurements.

5.3 Experimental observations

Adhesion and friction of metals are surface phenomena and depend on physical and chemical properties of the metals in contact, the contact force and surface condition, e.g., contamination. When a friction test is performed in the ambient environment, the existence of oxide and adsorption is almost unavoidable. Therefore, before each friction test, the top sample (zinc) was slid on the bottom sample under a relatively larger load (40 mN) to produce metal-metal contact in order to minimize the influence of oxide film or surface contamination on friction. The combination of normal and tangential forces may remove contaminated surface layers so that direct metal-metal contact with clean and fresh surfaces could be obtained [147].

After pre-rubbing treatment, friction coefficients of all 3d transition metals in contact with Zn under a light load of 1 mN were measured. Results of the friction measurement are illustrated in Fig. 5.1.

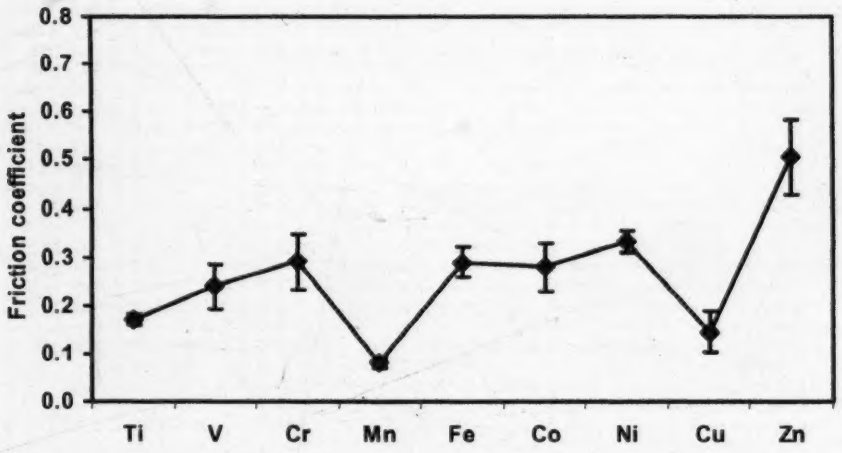

Figure 5.1 Experimentally measured friction coefficients of 3d transition metals in contact with Zn under 1mN.

5.4 An energy consumption model

5.4.1 Concept

In order to fundamentally understand the adhesion and friction between the 3d transition metals, attempts were made to establish a model to correlate the metallic friction to the surface electron behavior of the metals involved.

Since only friction under light loads is considered in this model, the surface deformation is assumed to be elastic. In addition, the surfaces in contact are generally considered to be smooth after fine polishing, so that elastic contact is more likely to be obtained

[27,150,158]. Single-asperity and multi-asperity contacts are commonly considered when investigating contact processes [2,20,22,24,25,27,28,158,159]. In the present model, the single-asperity contact is adopted in which a semi-sphere with its radius equal to R slides on a plate. This is a simplified situation but is widely used to study mechanical contacts [20].

From the point view of energy consumption, the work done by the frictional force that drives an asperity sliding on a plate over a unit distance is partially consumed in breaking the adhesive bonds and partially consumed in generating elastic deformation in both the asperity and the plate. In the present case, we ignore the frictional heat, which may not be negligible if the sliding speed and normal load are large. For contact processes under light loads in nano/micro-devices, frictional heating may not be a concern. As a result, the work done by friction may be expressed as a summation of the adhesion energy and the elastic strain energy:

$$F \cdot S = [A_r \cdot W_a + A_r \cdot W_e] \cdot (\frac{S}{d}) \qquad \textbf{(5.1)}$$

F - frictional force,

S - total sliding distance,

A_r - real contact area,

W_a - adhesion energy per unit contact area (J/m^2),

W_e - the average elastic energy in the contact region under a unit contact area,

d - diameter of contact area A_r,

(S/d) - the number of sliding steps; each step spans a distance of d.

During a continuous sliding process under a light load without plastic deformation involved, the elastic energy stored in the semi-sphere would approximately be constant. As a result, the portion of the work consumed by elastic deformation is mainly for the plate, which is recovered after the semi-sphere moves away from a specific contact area but the adjacent new contact area on the plate will be deformed, which consumes energy during the sliding process. Therefore, one may ignore the constant elastic deformation energy in the semi-sphere and only take account of the energy consumed by the plate, which increases as the sliding process proceeds. If we assume that the contact force is very small, then the overlap of strain fields of adjacent contact areas (one sliding step) could be neglected.

The friction coefficient is defined as,

$$F = \mu \cdot L \qquad \textbf{(5.2)}$$

where μ is the friction coefficient and L is the normal load. Combining equations (5.1) and (5.2), the friction coefficient can be turned into the following form:

$$\mu = \frac{A_r}{L \cdot d}(W_a + W_E) = \frac{A_r}{L \cdot (\frac{4A_r}{\pi})^{1/2}}(W_a + W_E) = \frac{\pi^{1/2} \cdot A_r^{1/2}}{2L}(W_a + W_E) \quad \textbf{(5.3)}$$

In order to calculate μ, three key parameters need to be determined. They are contact area (A_r), adhesion energy (W_a) and elastic energy (W_e). The contact area can be estimated based on DMT contact theory, which takes into account of the adhesion force and is suitable for metallic materials [21,22,24].

According to the DMT model, the contact area between a sphere with radius R and a flat plate is expressed as [20,25,159]:

$$A_r = \pi\left(\frac{3\pi W_a R^2}{2E^*}\right)^{2/3}\left(1 + \frac{L}{2\pi W_a R}\right)^{2/3} \quad \textbf{(5.4)}$$

where R is the radius of the semi-sphere. E^* is the reduced Young's modulus of the two contacting metals, which is expressed as:

$$\frac{1}{E^*} = \frac{1-\nu_1^2}{E_1} + \frac{1-\nu_2^2}{E_2} \quad \textbf{(5.5)}$$

where E_1, E_2, ν_1 and ν_2 are the Young's moduli and Poisson's ratios of the semi-sphere and the plate, respectively.

5.4.2 Adhesion energy

Allan et al. [65,67,160] used a simple self-consistent tight binding approximation and the method of moments to calculate the adhesion energy of a bimetallic interface.

The tight binding approximation (TBA) or linear combination of atomic orbitals (LCAO) is used to describe approximately the d bands of the transition metals. Isolated atoms have discrete allowed energy levels. When the atoms are brought together to form a crystal, their wavefunctions overlap and the Coulomb interaction between the atom cores and the electron splits the energy levels, spreading them into bands. The width of the band is proportional to the strength of the overlap interaction between neighbouring atoms. For transition metals, the atomic potential is quite large and the election wave function is mostly localized about the atomic core. That is the reason it is called "tight binding". TBA is used to calculate electronic band structure and gives a good description of the d band of transition metals [67,73,109].

The method of moment expands the density of states into a series of n^{th} order moments of the density of states about the center of energy of the DOS (density of states). The n^{th} moment of the local density of states on an atom i is determined by the sum of all paths of n hops (or steps) between neighboring atoms that star and end at

atom i. By doing this, the local cohesion energy is linked to the local atomic environment through the local electronic structure [161,162].

The adhesion energy (W_a) between two metals is defined as [65,66]:

$$W_a = \gamma_1 + \gamma_2 - \gamma_{12} \quad \textbf{(5.6)}$$

where γ_1 and γ_2 are the surface energies of metals 1 and 2 respectively. γ_{12} is their interface energy.

There are different methods to theoretically and experimentally determine surface energy of materials [11,163,164]. According to Allan's method, the surface energy per surface atom is equal to half of the energy difference between an infinite perfect crystal and its two separated half-parts. The surface energy is expressed as [65,67,160]:

$$\gamma = E_C\left(1-\sqrt{\frac{n'}{n}}\right) \quad \textbf{(5.7)}$$

where E_C is the cohesive energy per atom. n and n' are the second moments of the density of states of bulk and surface atoms, respectively. The second moment is a rough estimate of the band width [67], with which one may use the method of moments to calculate the local densities of states without using the reciprocal lattice [160]. The cohesive energy E_C is expressed as [65,160]:

$$E_C = 10\sqrt{\left(\frac{n}{2\pi}\right)}\exp\left(-\frac{E_F^2}{2n}\right) \qquad \textbf{(5.8)}$$

where E_F is the Fermi energy of a metal, which can be calculated by integration of the density of states using the following equation:

$$N_0(E_F) = \int_{-\infty}^{E_F} D(E)dE = \int_{-\infty}^{E_F} \frac{10}{\sqrt{2\pi n}}\exp\left(-\frac{E^2}{2n}\right)dE \qquad \textbf{(5.9)}$$

where $D(E)$ is the local density of states of d band per atom and N_0 is the number of d electrons per atom in the unperturbed crystal. $D(E)$ of d band as shown in Fig. 5.2 is approximated by a Gaussian curve fitted to the second moment of the density of states. The factor 10 in $D(E)$ is for the degeneracy of the d band [65,67]. If N_0 and n are known, the equation could be solved and the value of E_F can thus be determined.

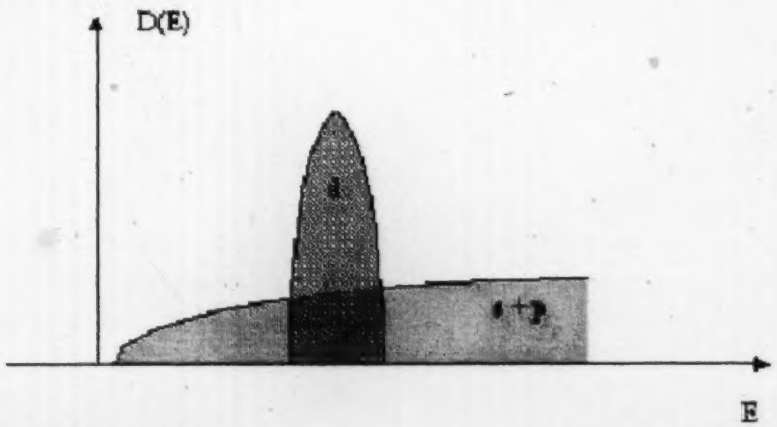

Figure 5.2 Schematic diagram for the density of states (D(E)) of a transition metal [162].

Equations (5.8) and (5.9) indicate that cohesive energy is assumed to come only from tight-binding d bands, because only density of states of d band was used in the equations. This is reasonable since for a transition metal the degree of filling the d electron band largely affects its physical and chemical properties [130-132,156].

The second moment of density of states is determined by only two hops (or steps): one hop from the central atom to a nearest neighbor atom and one hop back [161,162]. Therefore, it is proportional to the coordination number of the crystal under study. The second moments of bulk (n) and surface atoms (n') are expressed as [65,160]:

$$n = N\beta^2 \qquad \textbf{(5.10)}$$

$$n' = (N-M)\beta^2 \qquad \textbf{(5.11)}$$

where N and $N-M$ are the numbers of nearest neighbors of a bulk atom and a surface atom, respectively, which are determined by the crystal structure of the metal. β is the hopping integral between the first nearest bulk neighbors. The hopping integral is a function of the distance between neighboring atoms [165]. Fig. 5.3 illustrates the paths that contribute to the second moment of a two-dimensional simple cubic crystal. For 3d transition metals, a typical value of β is

equal to 5/12 ev [65,67]. Values of N and $N-M$ are given in Table 5.1 [67]:

Figure 5.3 Paths contributes to the second moment of a two-dimensional simple cubic crystal [162].

Table 5.1 Numbers of neighbors of a bulk (N) and a surface atom (N-M) on a (100) plane of typical metallic lattices (BCC,FCC and Simple Cubic)

	BCC	FCC	S.C.
N	8	12	6
N-M	4	8	5

The surface energy may thus be obtained by solving an equation set including equations (5.7)-(5.11). It is mainly a function of Fermi energy, influenced by the crystal structure of the metal.

Since the surface energy (γ) calculated from equation (5.7) to (5.11) is for a pair of atoms, it needs to be divided by b^2 to convert to energy per unit area [65]. Here b is the lattice constant of a metal. This is based on the assumption of Allan's method:

$$\frac{A}{N_S} = b^2 \qquad \textbf{(5.12)}$$

where A is the interface area and N_s is the number of surface atoms.

In this study, for simplicity an average value of b =4 $\overset{0}{A}$ was used for all metals, bearing in mind that all the samples were polished so that the crystal lattice in the surface layer was distorted with dislocations. Therefore, taking an average value of an interfacial area (choosing an equivalent (001) orientation) to calculate the number of atomic bonds per unit area for all metals is an approximate but reasonable treatment.

The surface energies (γ) per unit area of 3d transition metals were calculated with the procedure described above and result of the calculation is shown in Fig. 5.4.

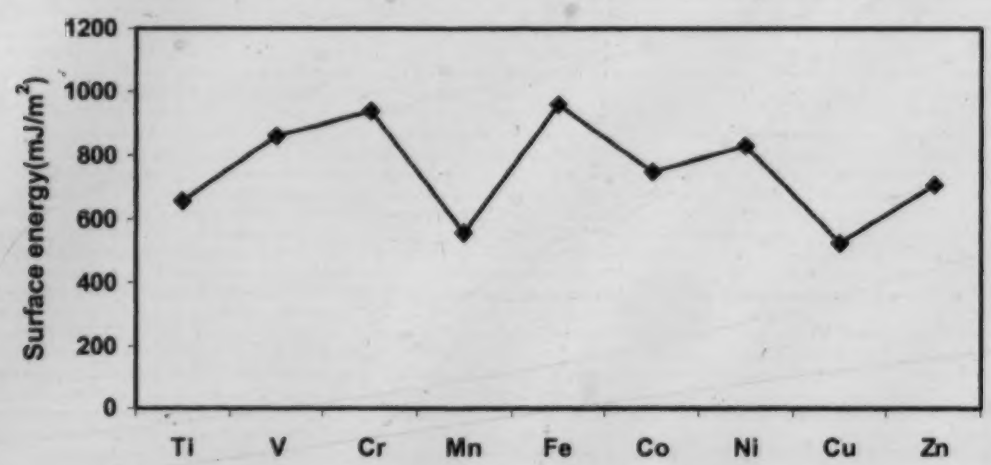

Figure 5.4 Surface energy calculated using equations (5.7)-(5.12).

The interfacial energy (γ_{12}) per unit interface area can be calculated using the following equation [65,67]:

$$\gamma_{12} = \frac{\varepsilon_0}{2l}\left(\frac{\varphi_1 - \varphi_2}{e}\right)^2 + \frac{\varepsilon_0}{e^2 l}(\varphi_1 - \varphi_2)\times \left[E_{F1} - E_{F2} + \frac{1}{4}\left(E_{F1}\frac{\Delta n_1}{n_1} - E_{F2}\frac{\Delta n_2}{n_2}\right)\right] - \frac{N_s}{2S}\left(E_{C1}\frac{\Delta n_1}{n_1} + E_{C2}\frac{\Delta n_2}{n_2}\right) \quad \textbf{(5.13)}$$

where φ is the EWF of a metal. l is the distance between the two metals at atomic level and may be reasonably assumed to be 4 $\overset{0}{A}$. ∇n_i is the difference in the second moment between an interfacial atom (n'') and a bulk atom (n). The second moment of interfacial atoms is expressed as [65]:

$$n_1^{*} = (N - M)\beta_1^{2} + M\beta^{'2} \quad \textbf{(5.14)}$$

where β' is the hopping integrals between interface atoms. For an interface between two transition metals of the same series, one may assume $\beta_1 = \beta_2 = \beta'$, so that $\nabla n = 0$, and equation (5.13) can be consequently changed to equation (5.15). The interfacial energy thus becomes a function of EWFs and Fermi energies of the two metals in contact.

$$\gamma_{12} = \frac{\varepsilon_0}{2l}\left(\frac{\varphi_1 - \varphi_2}{e}\right)^2 + \frac{\varepsilon_0}{e^2 l}(\varphi_1 - \varphi_2)\times [E_{F1} - E_{F2}] \quad \textbf{(5.15)}$$

Based on equation (5.15), the interfacial energy of two transition metals in contact can be calculated. E_F is deduced from

equation (5.9) and work functions can be measured experimentally, which are presented in Fig. 3.6.

With the procedure described above, the adhesion energy (W_a) per unit area between Zn and 3d transition metals were calculated and results of the calculation are shown in Fig. 5.5.

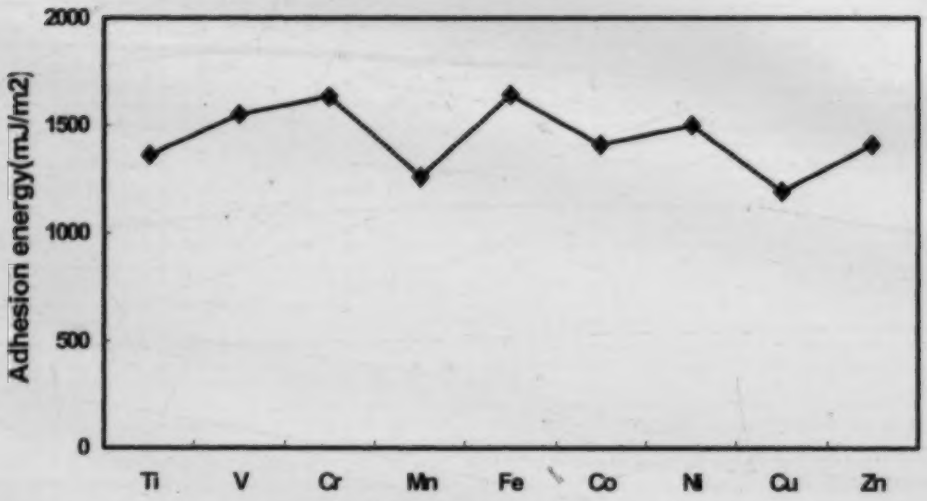

Figure 5.5 Adhesion energies for metals in contact with Zn, calculated using equations (5.6)-(5.15) [151].

5.4.3 Elastic strain energy

The total elastic strain energy (per unit volume) of a system containing a semi-spherical asperity and a plate is equal to:

$$W_{EV} = W_{EV1} + W_{EV2} = \int \sigma_1 d\varepsilon_1 + \int \sigma_2 d\varepsilon_2 = \int E_1 \varepsilon_1 d\varepsilon_1 + \int E_2 \varepsilon_2 d\varepsilon_2$$
$$= \frac{1}{2}(E_1 \bar{\varepsilon}_1^2 + E_2 \bar{\varepsilon}_2^2) \qquad \textbf{(5.16)}$$

where $\bar{\varepsilon}_1^2$ and $\bar{\varepsilon}_2^2$ are average elastic strains in the semi-sphere and the plate, respectively. Accurate calculation of the contact strain is complicated. In this study, the contact strain in the direction of contact force was estimated to determine the role of the strain energy plays in a light load friction process. The strain in the contact region may be expressed as [166]:

$$\varepsilon_z = \frac{\partial K}{\partial z} \qquad \textbf{(5.17)}$$

where K is the displacement along the direction of normal contact force, which may be approximated by the displacement of an infinitesimal element under a point normal force [29,166],

$$K = \frac{(1+\nu)L}{2\pi E\sqrt{x^2+y^2+z^2}}\left[2(1-\nu)+\frac{z^2}{x^2+y^2+z^2}\right] \qquad \textbf{(5.18)}$$

Equation (5.18) indicates that the vertical displacement at the surface decreases inversely with distance from the contact point i.e. the origin. Therefore, the average strain in the plate, concentrated at the contact point can be calculated by averaging the vertical strain over a certain distance just below the surface. Since the contact point is a singular point, we may estimate $\bar{\varepsilon}_z$ as:

$$\bar{\varepsilon}_z = \frac{1}{(a-0.1a)} \int_{0.1a}^{a} \varepsilon_{(x=0,y=0,z)} dz \qquad \textbf{(5.19)}$$

where a is the radius of the contact area. For estimation, the depth of 0.1a is chosen as the starting point for the strain calculation (equation (5.19). At the depth of a, the strain drops to 1% of $\varepsilon_{0.1a}$. This average strain was then used to estimate the strain energy of the plate. As we discussed earlier, we neglect the strain energy in the asperity, since its strain energy is constant during sliding on a smooth plate; the deformation of the asperity therefore does not contribute to the energy consumption during a continuous sliding process.

The elastic strain energy (W_E) per unit contact area of the plate is equal to:

$$W_E = W_{EV} \times D \qquad \textbf{(5.20)}$$

where D is the effective depth of stress-affected region under the contact surface. In this study, the strain energy is estimated using an effective depth (D) that is six times as large as the radius of the contact area. At the edge of such a stress-affected region, the maximum principle stress is close to 10% of the normal stress at the surface [167]. Fig. 5.6 illustrates the stress contour lines in the xz-plane, and Y-direction that are due to tangential and normal loads on an elastic solid. In the figure, a is the radius of the contact

area. The maximum stress in the figure is decreases to around 10% of the normal stress at a depth of 6a. We may choose a larger D, e.g. 7a as the effective depth of stress-affected region; however, a D larger than 6a will not affect the order of magnitude of the strain energy.

With this approximation and letting $\varepsilon_2 = \varepsilon_z$, the strain energy was calculated using equations (5.16) - (5.20). This estimated strain energy is in the order of 10^{-3} J/m^2, which is sufficiently small in comparison with the adhesion energy (10^0 J/m^2). Therefore, the strain energy could be neglected in the calculation of friction coefficient for elastic contact under light loads.

Combining equations from (5.4) to (5.20), the friction coefficient of two metallic surfaces can be approximately calculated using equation (5.3). Material properties needed for the calculation are: EWF, Fermi energy, Young's modulus, Poisson's ratio of the two metals. For the present calculation, the elastic constants and Poisson's ratios were taken from reference [168], EWFs of the metals were measured experimentally [127], and Fermi energies were calculated based on references [65,67].

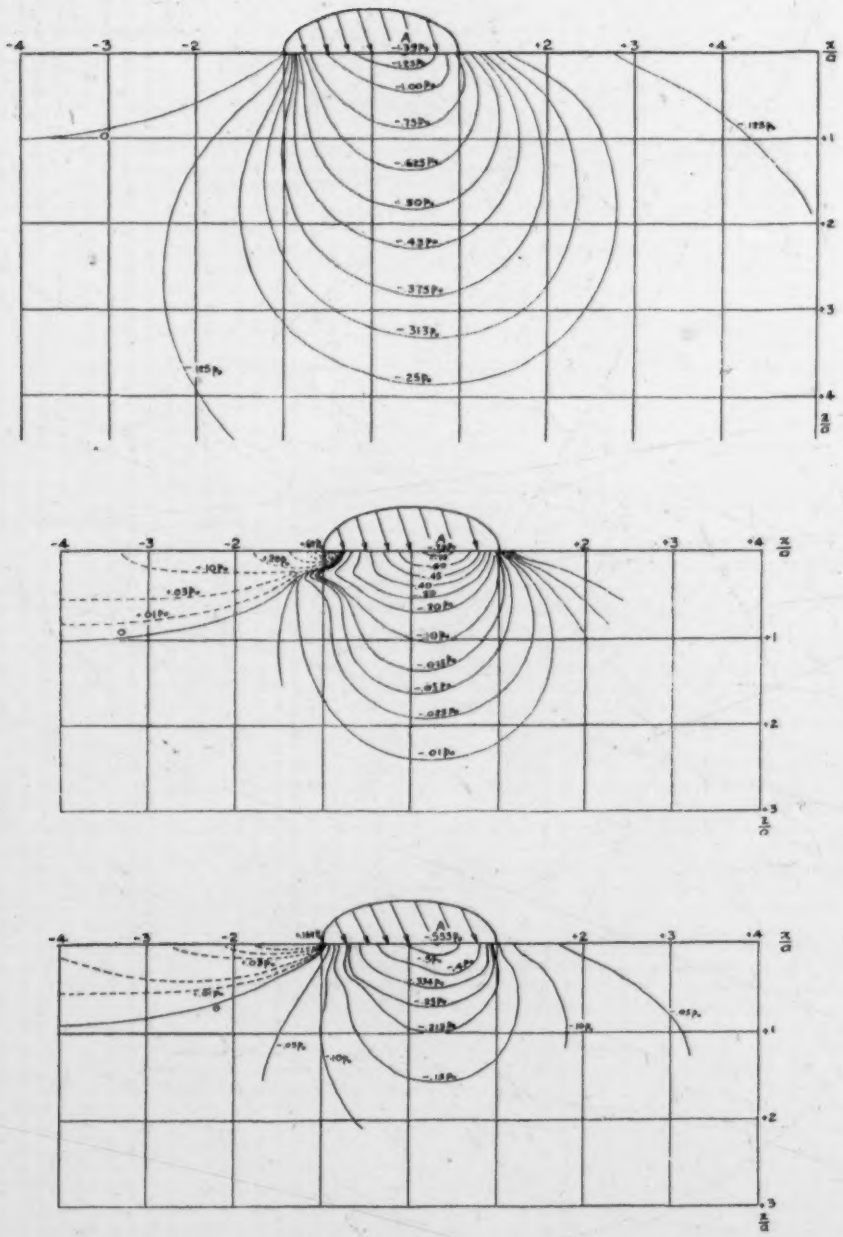

Figure 5.6 (a) Contours represent constant values of one of the two principle stresses in xz-plane.(b) Contours represent constant values of one of the two principle stresses in xz-plane. (c) Contours of principle stresses in Y-direction [167].

5.5 Theoretical prediction of friction under light loads

Fig. 5.7 presents calculated friction coefficients of 3d metals in contact with Zn under a light load using the proposed approach. In the calculation, a semi-sphere was assumed to have its radius equal to 4 mm sliding on a flat counter-face under a light contact load of 0.1 mN, which led to a contact area in the order of 10^{-10} m^2. The stress under this load ($\approx 0.1mN/10^{-10}$ m^2=1 MPa) is below the elastic yield strength of all the testing metals, so that the elastic contact is ensured.

By comparison with the experimentally measured friction coefficients under a light load of 1mN (Fig. 5.1), the predicted variation in friction coefficient against the metal type is consistent with that experimentally observed to some degree. Fig. 5.5 illustrates the adhesion energy calculated using equations (5.6)-(5.15), which is in agreement with the friction coefficient (Fig. 5.7), because friction under a light load is dominated by adhesion.

The predicted changes in the friction coefficient of Zn against other metals (Fig. 5.7) are basically consistent with those experimentally observed (Fig. 5.1). However, discrepancy still exists between the prediction and experimental measurement, e.g. the

scale. This may be attributed to the fact that the proposed model is a simplified approach, in which we deal with the contact between an asperity and a plate rather than two plates in contact as arranged in the experiment. Realistic surfaces are rough with asperities having different morphologies, which may enhance the mechanical interaction or the effect of plowing. Such enhancement in mechanical interaction could increase the friction coefficient especially for soft metals such as Zn.

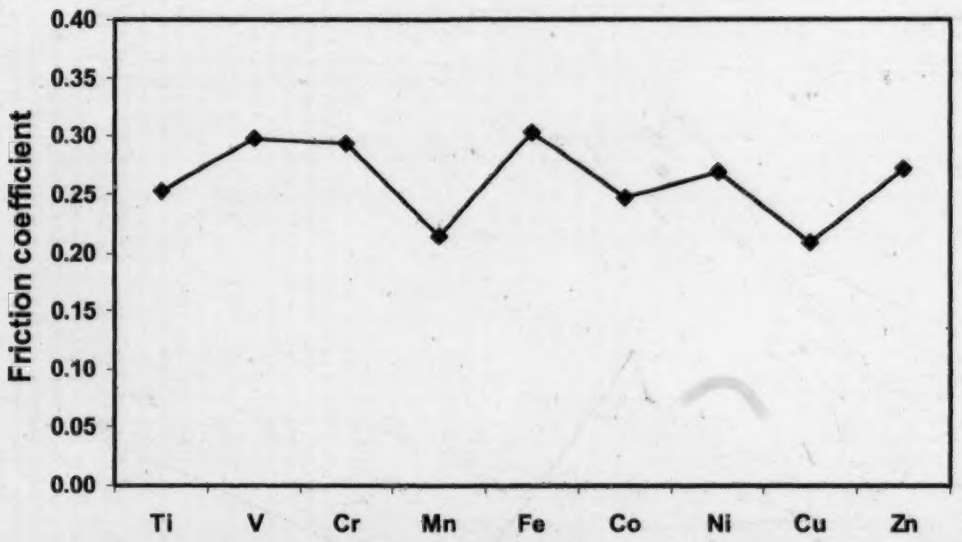

Figure 5.7 Calculated friction coefficients of 3d transition metals in contact with Zn using the proposed ECF model. Contact condition: a semi-spherical ball with its radius equal to 4 mm slid on a flat counter-face under a light load of 0.1 mN [151].

5.6 Conclusions

An energy consumption friction model (ECF) is proposed to predict adhesion and friction behavior of 3d transition metals in elastic contact under light loads. The prediction is made based on the electron work functions and Fermi energies of two metals in contact, incorporating the DMT model for calculating the elastic contact area. It was shown that the elastic strain energy made negligible contribution to friction for elastic contact under light loads. Reasonable agreement between the theoretical prediction using the model and experimental observations has been found.

Chapter 6 : Prediction of light-load friction solely based on EWF

As demonstrated in Chapter 5, EWF and elastic modulus of metals have been shown to be dominant parameters for adhesion and light-load friction of metals.

This chapter presents the study to correlate the elastic properties of metal with the EWF. It is demonstrated that there exists a strong correlation between EWF and elastic behavior. Such a correlation makes it possible to predict adhesion and elastic-contact friction mainly based on the EWF [133].

6.1 Introduction and objective

In Chapter 5, adhesion and light-load friction of metals were predicted using an ECF (energy consumption friction) model. The model incorporated adhesion energy and deformation energy when the two metals slide on each other. Based on this model, adhesion and light load friction may be predicted mainly based on the EWFs and elastic moduli of the metal pair.

The objective of this study was to develop a simple approach using the fundamental parameter, the EWF only, to deal with adhesion and friction under light loads, which could be beneficial to

material selection and optimization of nano/micro-devices. To develop such an approach with EWF as the single parameter in the prediction of adhesion and friction, it is necessary to correlate the elastic properties of metal with the EWF [133].

6.2 Relationship between EWF and mechanical properties

EWF is the minimum energy required to move electrons from inside a metal to its surface with zero kinetic energy [16]. EWF reflects the surface electronic behavior and is a fundamental material property [72]. The EWF strongly affects various material properties such as electrode potentials, atomic volume, ionization potential and electronegativity, etc. [169]. This parameter is closely related to a wide range of surface phenomena including adsorption, surface segregation [81,88], precursor of wear [86,170], and electrochemical stability [116].

It is not surprising that EWF and mechanical properties of metals should be intimately related, since contact mechanical properties are also intrinsically dependent on the electron behavior that determines the strength of metallic bonds [171,172]. For instance, Young's modulus and shear modulus are governed by interatomic potentials, electron state, and phonon spectra [173].

EWF characterizes the electron behavior and is approximately equal to the depth of the potential well [124]. The elastic modulus is determined by the interatomic bond strength which directly depends on the electronic configuration of the solid [172]. If a relationship between EWF and mechanical behavior can be established, adhesion and elastic-contact friction could be predicted mainly based on EWF [133].

There have been studies to correlate EWF with Poisson's ratios [94] and bulk modulus [174]. The bulk modulus determines the volume stiffness of a crystal lattice under an applied reversible hydrostatic compression, which is one of the fundamental elastic moduli for isotropic materials [175,176]. This modulus depends mainly on the potential energy-interatomic distance relationship because any change in volume requires a corresponding change in the bond length [176]. Therefore, the bulk modulus is closely related to other properties that depend on the interatomic potential, such as the cohesive energy, hardness and lattice constant [175-177]. Fig. 6.1 illustrates the bulk moduli of transition metals from literature [168] and the EWFs from our measurement using a scanning Kelvin probe (Chapter 3) [127]. The value of EWF is multiplied by 100 to fit the EWF and bulk modulus into one figure. It is evident that the EWF and bulk moduli of the metals have similar

trends. It should be mentioned that the EWF measurements were carried out in the ambient environment; in such an environment, the electron work function could be influenced by a possible adsorption layer or oxide film (e.g., passive film), which may make the measured value more or less deviate from the intrinsic electron work function of a metal [178-181]. It is very difficult to determine the EWF of a pure metal since adsorption or an oxide film is likely to form. Our EWF measurements were carried out right after the samples were polished. As mentioned in Chapter 3, such polishing treatment has two main effects: 1) remove or reduce a possible oxide film developed on the metal, and 2) introduce surface deformation to minimize the regular atomic arrangement in the crystal lattice. As a result, the influences of possible oxide film and the crystallographic orientation on EWF could be minimized, so that one may obtain the information on EWF that is more directly related to the atomic bond of the metal, on which its bulk elastic properties are basically dependent. Besides, a naturally formed oxide film in a dry ambient environment, if it forms, is very thin and may not have a large influence on the ranking of metals in terms of the EWF, which has been demonstrated by the similar EWF ranking of transition metals determined in vacuum [90] in comparison with that from our measurements [127,133].

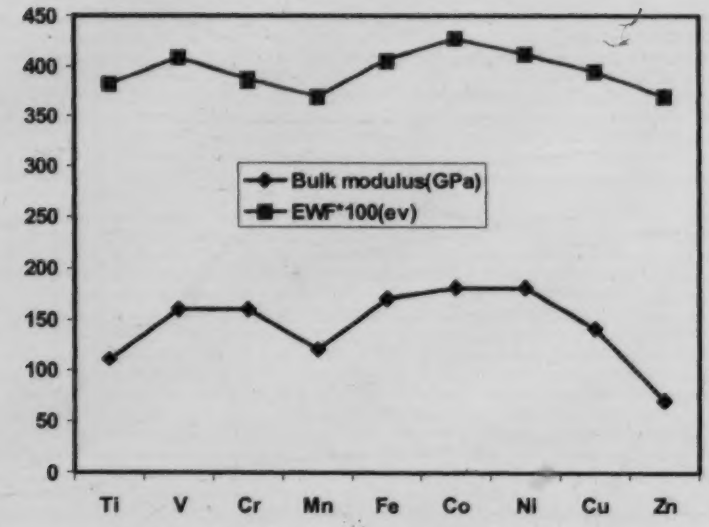

Figure 6.1 The EWF [127]and bulk modulus [168] of 3d transition metals.

Many theoretical studies have been devoted to the calculation of bulk modulus of metals and compounds. Makino empirically expressed bulk modulus as a function of interatomic distance [182] or effective pseudopotential radius [183]. Bulk modulus has been calculated using the first principle method based on the density function theory (DFT) with both local density approximation (LDA) or generalized gradient corrections (GGA) [173,184-187]. Stabilized jellium model has also been employed to calculate the bulk modulus [174]. The parameter required to specify the stabilized jellium is

only the average valence electron density in the bulk [174,188]. Both EWF and bulk modulus depend on the density parameter (r_s) by power laws. Bulk moduli of some metals are well fitted to $r_s^{-7/2}$ while the EWFs are fitted to $r_s^{-0.5}$. These two parameters are related by the following simple equation [174]:

$$B = \frac{0.143\varphi}{r_s^3} \qquad \textbf{(6.1)}$$

where B and φ are the bulk modulus and the EWF of the metal, respectively. The density parameter r_s is the Wigner-Seitz radius of a sphere containing a single electron, which can be determined using the following equation [174,188]:

$$r_s = \left(\frac{3}{4\pi \bar{n}}\right)^{1/3} \qquad \textbf{(6.2)}$$

where $\bar{n}$ is average valence electron density in the bulk [174,188].

In our previous study, friction coefficients of 3d transition metals in contact with Zn were measured using a micro-tribometer provided by CETR (California, USA) [151]. Details of the experimental measurement have been given in Chapter 3. The samples were plates of pure polycrystalline metals. A pre-rubbing process was performed before the friction measurement in order to minimize the influence of surface contamination or possible oxide

film on the measured friction coefficients. A detailed discussion regarding the function of the pre-rubbing process can be found in Chapter 4 section 4.3.1. Fig. 6.2 presents experimental results of the friction measurements under 1 mN. Friction coefficients were also calculated using an energy consumption friction (ECF) model [151]. In this model, the work done by the friction force is consumed partially in breaking the adhesive bonds and partially in generating elastic deformation in the surface layers of two metals in contact. So the work done by friction may be expressed as a summation of the adhesion energy and the elastic strain energy. Details of this model can be found in Chapter 5 section 5.4.

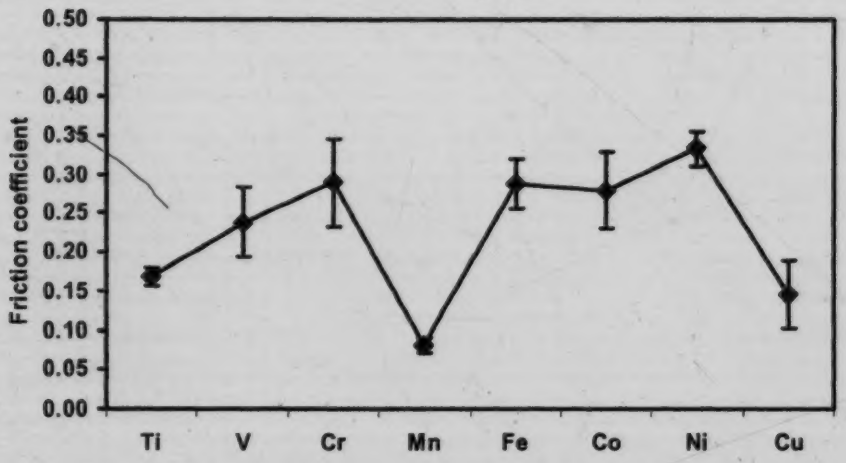

Figure 6.2 Friction coefficients of 3d transition metals in contact with Zn under 1mN [151]. Nominal contact area is 4×4 mm^2.

Based on the ECF model, the friction coefficient of two metals in contact under light loads can be calculated. The material properties needed for the calculation are EWF, Fermi energy, Young's modulus and Poisson's ratio. According to the theory of elasticity, Young's modulus (E) is expressed as a function of bulk modulus (B), and Poisson's ratio (ν) [151].

$$E = 3B(1-2\nu) \qquad \textbf{(6.3)}$$

With this relationship, E may be represented as a function of the EWF and r_s [189] because of B=B(EWF, r_s) as expressed in equation (6.1). For many metals and alloys, their Poisson's ratios range between 0.25 and 0.35, Poisson's ratios of the 3d transition metals are therefore assumed to be equal to 0.3 [13,190]. Consequently, Young's modulus can be related to electronic properties. Thus, EWF becomes the main input needed for prediction of friction coefficient under elastic contact conditions. Fig. 6.3 presents calculated friction coefficients under a light contact load with EWF as a dominant parameter using equation (5.3). The consistency between Fig. 6.2 and Fig. 6.3 shows that the adhesion and elastic-contact friction could be predicted mainly based on EWF.

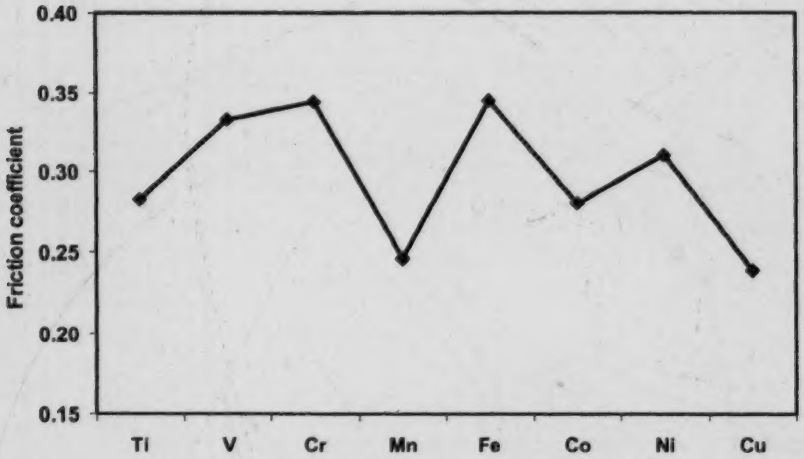

Figure 6.3 Calculated friction coefficients of 3d transition metals in contact with Zn using the proposed ECF model described in Chapter 5 with EWF as the main parameter. Contact condition: a semi-spherical ball with its radius equal to 4 mm slid on a flat counter-face under a light load of 0.1 mN.

It may need to be indicated that although the predicted changes in the friction coefficient of Zn against other metals (Fig. 6.3) are consistent with the experimental observation (Fig. 6.2), discrepancy still exists between the prediction and the experimental measurement, e.g. the scale. This could be attributed to the fact that in this simplified theoretical treatment, we deal with the contact between an asperity and a plate while in the friction measurement we used two plate samples in contact. Besides, the theoretically

treated one is an ideal situation, while the experimental measurement could be affected by many additional factors, such as the surface roughness at microscopic scale, which affects the contact condition, and possible environmental influences [133].

6.3 Further discussion

With the established correlation between EWF and Young's modulus, friction coefficients can be calculated mainly based on EWF although the calculation also involves Fermi energy (E_F) and electron density (r_s). Research on the calculation of EWF shows the relationship among EWF, Fermi energy and electron density.

Halas and Durakiewicz improved Brodie's approach of calculating EWF with classical electrostatic image-potential. They used the length of spontaneous polarization of the electron gas at the Fermi level to calculate the distance *d* at which the image force begins to act. According to their theory, EWF is expressed as a function of Fermi energy and electron density [90-92]:

$$\varphi = \frac{43.46\alpha^*}{r_s^{3/2} E_F^{1/2}} \qquad (6.4)$$

where r_s is expressed in atomic units (Bohr radius). The scaling factor α^* was assumed to be equal to unity for all elements except

the alkali metals, Ca, Sr, Ba, Ra and Tl for which it was assumed to be equal to 0.86 [90-92].

Fermi energy can be expressed solely in terms of electron density for practical calculations [91]:

$$E_F = 50.03 r_s^{-2} \tag{6.5}$$

The work function may now be expressed as [91]:

$$\varphi = 6.15 \times \alpha^* \times r_s^{-1/2} \tag{6.6}$$

Based on equation (6.5) to (6.6), Fermi energy can be expressed as a function of EWF:

$$E_F = \frac{0.035 \varphi^4}{\alpha^{*4}} \tag{6.7}$$

Therefore both Fermi energy and electron density are related to EWF by a simple equation. According to Allan's self-consistent theory, the local density of states per atom was fitted to a Gaussian curve which is centered on the energy zero, so Fermi energy must be calculated according to equation (5.9). Although equation (6.7) cannot be used to calculate adhesion energy in the ECF model, these equations provides further proof for the statement that EWF is the main input for prediction of friction coefficient under elastic contact conditions.

6.4 Conclusions

From the above analysis it is shown that both EWF and mechanical behavior are dependent on the electronic behavior of metals and such dependence relates EWF with mechanical properties. The reasonable agreement between the measured friction coefficients of 3d transition metals under light loads and the calculation results suggests that EWF is a fundamental parameter that could be used to predict the adhesion and friction of metals under elastic-contact conditions [133].

Chapter 7 : Conclusions and future studies

This chapter summarizes the conclusions drawn from this dissertation research. Possible further research topics are suggested.

Adhesion and friction of solids are two important issues of nanotribology. With the development of nanotechnology, it is essential to understand the mechanisms of tribological processes under light loading condition. Efforts were made in this research to investigate adhesion and friction under light loads from experimental as well as theoretical perspectives. The correlations of adhesion and friction with EWF were established for both ceramic-metal and metal-metal pairs. For ceramic-metal pairs, EWF, adhesion and friction were correlated based on phenomenological observations. Metal-metal friction coefficients under light loads were measured and a semi-empirical treatment was first used to establish the relationships between EWF and adhesion/friction between metals. Then an energy consumption friction (ECF) model was proposed to calculate the metal-metal friction coefficient quantitatively. EWF and mechanical properties of the metals are the main parameters used in this model. The correlation between EWF

and the elastic behavior of metal was finally studied with the aim of predicting adhesion and friction mainly based on the EWF.

7.1 Conclusions

In this work, the relationships among EWF, adhesion and friction are investigated, and EWF has proven to be a promising parameter which can be used to predict adhesion and friction.

Adhesion and friction of ceramic-metal contact were evaluated employing an atomic force microscope (AFM) that may also function as a lateral force microscope (LFM). Results of the measurements demonstrated unambiguous correlation between these two properties: the lower the EWF, the higher the adhesion. As a result, a smooth metal surface having lower EWF showed a larger frictional force when tested under light loads. The friction measurement with a sharp tip demonstrated that mechanical properties played a more important role than adhesion under larger contact forces when the mechanical interaction became predominant. In this case, harder metals showed lower friction.

Metal-metal frictions under light load were investigated using a microtribometer. It was demonstrated that adhesion and friction of the transition metals were closely related to their EWFs. The adhesion between two metals in contact could be expressed as a

function of their EWFs and electron densities using Miedema's semi-empirical method. Consequently, the friction between the two metals under light loads could be estimated based on these two parameters.

The relationship between EWF, adhesion and friction was further investigated by proposing an ECF model for lightly loaded contact. This model assumes elastic contact between two metals in contact. Adhesion energy and deformation energy of the two metals when they slide against each other were included in the calculation. In addition, adhesion energy in this model was calculated based on more concrete physics concepts. Allan's self-consistent theory of adhesion at a bimetallic interface was employed to determine adhesion energy between two metals based on their electron work function and Fermi energy. DMT model was incorporated to calculate the elastic contact area. It was shown that the elastic strain energy made negligible contribution to friction for elastic contact under light loads. Reasonable agreement between the theoretical prediction using the ECF model and experimental observation has been found.

EWF and elastic modulus of metals have been demonstrated to be important parameters for adhesion and light-load friction of metals. Our study has demonstrated that there is strong correlation between EWF and elastic behavior. Such a correlation makes it

possible to predict adhesion and elastic-contact friction mainly based on the EWF as demonstrated in this study. The reasonable agreement between the measured friction coefficients of 3d transition metals under light loads and the calculation results mainly based on EWF suggests that EWF is a fundamental parameter that could be used to predict the adhesion and friction of metals under elastic contact conditions.

7.2 Future studies

The relationships among EWF, adhesion and friction have been investigated. The consistency between experimental measurements and theoretical calculations has demonstrated that EWF could be used to predict adhesion and light-loaded friction. In order to further understand the relationship and make more accurate prediction of adhesion and friction, the following studies need to be conducted.

7.2.1. Using improved contact model

The proposed energy consumption friction (ECF) model is a simplified single asperity model. A multi-asperity model should be developed to improve the validity of the prediction. In addition, elastic contact between two metals was assumed in this model. This is not unreasonable because of the light-loaded contact condition

and smooth contact surfaces. However, there are always some plastic deformed asperities in the bimetallic interface, which is ignored in this mode. A more complicated contact model which is closer to the real situation and takes into account both elastic and plastic deformation would improve the theoretical prediction.

7.2.2 More fundamental studies

More fundamental studies should be conducted to better understand the relationship between EWF, adhesion and friction. Allan's self-consistent theory of adhesion at a bimetallic surface involves some assumptions that affect the calculation result [156]. Incorporating first principle calculations of adhesion energy into the prediction of adhesion and friction would deepen our understanding of the correlation between EWF, adhesion and friction.

7.2.3 The dependence of friction coefficient on load

Friction coefficient is often assumed to be a constant. However, load dependence of the friction coefficient is widely observed [54]. This phenomenon was also noticed in the friction measurement of 3d transition metals in contact with iron and zinc. In different loading ranges, the friction coefficient showed different values. Under lighter loads, the friction coefficient is mainly dependent on the adhesion between two surfaces in contact; under larger loads,

the friction is dominated by mechanical plowing and deformation. It is worth investigating the dependence of friction on load and extending the current approach to a comprehensive model for general friction prediction.

References

[1] Friction, lubrication, and wear technology, ASM handbook, ASM International, Materials Park, OH, 1990.

[2] I.M. Hutchings, Tribology: Friction and Wear of Engineering Materials, CRC Press, Boca Raton, 1992.

[3] H. Czichos, Tribology: a systems approach to the science and technology of friction, lubrication, and wear, Elsevier, New York, 1978.

[4] B.N.J. Persson, Sliding friction: physical principles and applications, Springer-Verlag, Berlin, 2000.

[5] D. Maugis, Creep, Hot Hardness and Sintering in the Adhesion of Metals at High-Temperature, Wear 62 (1980) 349-386.

[6] K.L. Johnson, Mechanics of adhesion, Tribol. Int. 31 (1998) 413-418.

[7] Y.-P. Zhao, L.S. Wang, T.X. Yu, Mechanics of adhesion in MEMS - a review, J. Adhes. Sci. Technol. 17 (2003) 519-546.

[8] G. Carbone, L. Mangialardi, B.N.J. Persson, Adhesion between a thin elastic plate and a hard randomly rough substrate, Phys. Rev. B 70 (2004).

[9] B. Bhushan, Handbook of micro/nanotribology, CRC Press, Boca Raton, 1999.

[10] A. Dayo, J. Krim, Atomic-Scale Friction in Xe/Ag and N2/Pb, Inter. J. Thermophysics 19 (1998) 827-834.

[11] D.H. Buckley, Surface effects in adhesion, friction, wear, and lubrication, Elsevier, New York, 1981.

[12] N. Ohmae, T. Okuyama, T. Tsukizoe, Influence of Electronic-Structure on the Friction in Vacuum of 3d Transition-Metals in Contact with Copper, Tribol. Int. 13 (1980) 177-180.

[13] E. Rabinowicz, Friction and wear of materials, Wiley, New York, 1995.

[14] A. Dayo, W. Alnasrallah, J. Krim, Superconductivity-Dependent Sliding Friction, Phys. Rev. Lett. 80 (1998) 1690-1693.

[15] B.N.J. Persson, A.I. Volokitin, Dynamical interactions in sliding friction, Surf. Sci. 457 (2000) 345-356.

[16] N.W. Ashcroft, N.D. Mermin, Solid state physics, Holt, Rinehart and Winston, New York, 1976.

[17] K.-H. Zum Gahr, Microstructure and wear of materials, Elsevier, Amsterdam; New York, 1987.

[18] U. Landman, W.D. Luedtke, N.A. Burnham, R.J. Colton, Atomistic Mechanisms and Dynamics of Adhesion, Nanoindentation, and Fracture, Science 248 (1990) 454-461.
[19] K.C. Ludema, Friction, wear, lubrication : a textbook in tribology, CRC Press, Boca Raton, 1996.
[20] E. Meyer, Nanoscience : friction and rheology on the nanometer scale, World Scientific, New Jersey, 1998.
[21] S.K.R. Chowdhury, P. Ghosh, Adhesion and Adhesional Friction at the Contact between Solids, Wear 174 (1994) 9-19.
[22] W.R. Chang, I. Etsion, D.B. Bogy, Adhesion Model for Metallic Rough Surfaces, J Tribol-T Asme 110 (1988) 50-56.
[23] P. Sahoo, S.K.R. Chowdhury, A fractal analysis of adhesive friction between rough solids in gentle sliding, P I Mech Eng J-J Eng 214 (2000) 583-595.
[24] M.D. Pashley, J.B. Pethica, D. Tabor, Adhesion and Micromechanical Properties of Metal-Surfaces, Wear 100 (1984) 7-31.
[25] Y.-P. Zhao, X. Shi, W.J. Li, Effect of work of adhesion on nanoindentation, Rev. Adv. Mater. Sci. 5 (2003) 348-353.
[26] F.M. borodich, B.A. Galanov, Molecular adhesive contact for indenters of non-ideal shapes, in: XXI International congress of theoretical and applied mechanics (Warsaw, 2004).
[27] J.A. Greenwood, J.B.P. Williamson, Contact of Nominally Flat Surfaces, Proc. R. Soc. A 295 (1966) 300-319.
[28] H. Zahouani, F. Sidoroff, Rough surfaces and elasto-plastic contacts, Comptes Rendus De L Academie Des Sciences Serie Iv Physique Astrophysique 2 (2001) 709-715.
[29] N.P. Suh, Tribophysics, Prentice-Hall, Inc., New Jersey, 1986.
[30] O.M. Braun, A.G. Naumovets, Nanotribology: Microscopic mechanisms of friction, Surf. Sci. Rep. 60 (2006) 79-158.
[31] E.D. Hondros, Tribology, Mills & Boon, London, 1971.
[32] F.P. Bowden, D. Tabor, The Friction and lubrication of solids, Clarendon Press, Oxford, 1950.
[33] D.H. Buckley, Adhesion of Metals to a Clean Iron Surface Studied with Leed and Auger Emission-Spectroscopy, Wear 20 (1972) 89-103.
[34] M.E. Sikorski, The adhesion of metals and factors that influence it, Wear 7 (1964) 144-162.
[35] K. Miyoshi, Fundamental Considerations in Adhesion, Friction and Wear for Ceramic Metal Contacts, Wear 141 (1990) 35-44.

[36] A.K. Vijh, Influence of Metal-Metal Bond-Energies on Adhesion, Hardness, Friction and Wear of Metals, J. Mater. Sci. 10 (1975) 998-1004.
[37] A.J. Gellman, J.S. Ko, The current status of tribological surface science, Tribol. Lett. 10 (2001) 39-44.
[38] B. Bhushan, Nano- to microscale wear and mechanical characterization using scanning probe microscopy, Wear 250 (2001) 1105-1123.
[39] B. Bhushan, Nanotribology and nanomechanics, Wear 259 (2005) 1507-1531.
[40] B. Bhushan, Nanotribology and nanomechanics of MEMS/NEMS and BioMEMS/BioNEMS materials and devices, Microelectron. Eng. 84 (2007) 387-412.
[41] Z.H. Tao, B. Bhushan, Surface modification of AFM Si3N4 probes for adhesion/friction reduction and imaging improvement, J Tribol-T Asme 128 (2006) 865-875.
[42] Y.X. Song, B. Bhushan, Atomic-scale topográphic and friction force imaging and cantilever dynamics in friction force microscopy, Phys. Rev. B 74 (2006) 165401.
[43] R. Szoszkiewicz, B. Bhushan, B.D. Huey, A.J. Kulik, G. Gremaud, Correlations between adhesion hysteresis and friction at molecular scales, J. Chem. Phys. 122 (2005) 6.
[44] H.W. Liu, B. Bhushan, Adhesion and friction studies of microelectromechanical systems/nanoelectromechanical systems materials using a novel microtriboapparatus, J. Vac. Sci. Technol. A 21 (2003) 1528-1538.
[45] B. Bhushan, C. Dandavate, Thin-film friction and adhesion studies using atomic force microscopy, J. Appl. Phys. 87 (2000) 1201-1210.
[46] N.S. Tambe, B. Bhushan, Nanoscale friction mapping, Appl Phys Lett 86 (2005) 193102.
[47] B. Bhushan, Z. Burton, Adhesion and friction properties of polymers in microfluidic devices, Nanotechnology 16 (2005) 467-478.
[48] N.S. Tambe, B. Bhushan, A new atomic force microscopy based technique for studying nanoscale friction at high sliding velocities, J. Phys. D-Appl. Phys. 38 (2005) 764-773.
[49] K. Iwahori, S. Watanabe, M. Kawai, K. Kobayashi, H. Yamada, K. Matsushige, Effect of water adsorption on microscopic friction force on SrTiO3(001), J. Appl. Phys. 93 (2003) 3223-3227.
[50] R. Prioli, D.C. Reigada, F.L. Freire, The role of capillary condensation of water in the nanoscale friction and wear

properties of boron carbide films, J. Appl. Phys. 88 (2000) 679-682.
[51] J.Y. Park, D.F. Ogletree, P.A. Thiel, M. Salmeron, Electronic control of friction in silicon pn junctions, Science 313 (2006) 186-186.
[52] J.Y. Park, D.F. Ogletree, M. Salmeron, C.J. Jenks, P.A. Thiel, Friction and adhesion properties of clean and oxidized Al-Ni-Co decagonal quasicrystals: a UHV atomic force microscopy/scanning tunneling microscopy study, Tribol. Lett. 17 (2004) 629-636.
[53] A.G. Peressadko, N. Hosoda, B.N.J. Persson, Influence of surface roughness on adhesion between elastic bodies, Phys. Rev. Lett. 95 (2005).
[54] I.L. Singer, H.M. Pollock, Fundamentals of friction: macroscopic and microscopic processes, Kluwer Academic Publishers, Netherlands, 1992.
[55] J.H. Rose, J. Ferrante, J.R. Smith, Universal Binding-Energy Curves for Metals and Bimetallic Interfaces, Phys. Rev. Lett. 47 (1981) 675-678.
[56] J.H. Rose, J.R. Smith, J. Ferrante, Universal Features of Bonding in Metals, Phys. Rev. B 28 (1983) 1835-1845.
[57] J. Ferrante, J.R. Smith, Theory of the Bimetallic Interface, Phys. Rev. B 31 (1985) 3427-3434.
[58] J. Ferrante, Applications of Surface-Analysis and Surface Theory in Tribology, Surf. Interface Anal. 14 (1989) 809-822.
[59] J.R. Smith, J.G. Gay, F.J. Arlinghaus, Self-Consistent Local-Orbital Method for Calculating Surface Electronic-Structure - Application to Cu(100), Phys. Rev. B 21 (1980) 2201-2221.
[60] M.J.S. Spencer, A. Hung, I.K. Snook, I. Yarovsky, Further studies of iron adhesion: (111) surfaces, Surf. Sci. 515 (2002) L464-L468.
[61] G. Pacchioni, Metal/oxide adhesion energies from first-principles, Surf. Sci. 520 (2002) 3-5.
[62] J. Gerkema, A.R. Miedema, Adhesion between Solid Metals - Observations of Interfacial Segregation Effects in Metal-Film Lubrication Experiments, Surf. Sci. 124 (1983) 351-371.
[63] A.R. Miedema, F.J.A. Denbroeder, Interfacial Energy in Solid-Liquid and Solid-Solid Metal Combinations, Z. Metallk. 70 (1979) 14-20.
[64] A.R. Miedema, Surface Energies of Solid Metals, Z. Metallk. 69 (1978) 287-292.

[65] G. Allan, M. Lannoo, Dobrzyns.L, Simple Self-Consistent Theory of Adhesion at a Bimetallic Interface, Philosophical Magazine 30 (1974) 33-45.
[66] G. Allan, M. Lannoo, L. Dobrzynski, Adhesion at a Bimetallic Interface, Japanese Journal of Applied Physics (1974) 715-718.
[67] L. Dobrzynski, Handbook of surfaces and interfaces, Vol. 1, Garland STPM Press, New York, 1978.
[68] P. Ying, N.B. Liao, Surface sliding simulation in micro-gear train for adhesion problem and tribology design by using molecular dynamics model, Comput. Mater. Sci. 38 (2007) 678-684.
[69] L.Z. Zhang, S.Y. Jiang, Molecular simulation study of nanoscale friction between alkyl monolayers on Si(111) immersed in solvents, J. Chem. Phys. 119 (2003) 765-770.
[70] S.S. Cho, S. Park, Molecular dynamics simulation of adhesion processes, KSME Int. J. 16 (2002) 1440-1447.
[71] Y.S. Leng, S.Y. Jiang, Dynamic simulations of adhesion and friction in chemical force microscopy, J. Am. Chem. Soc. 124 (2002) 11764-11770.
[72] L.H. Lee, Fundamentals of adhesion, Plenum Press, New York, 1991.
[73] C. Kittel, Introduction to solid state physics, Wiley, New York, 1996.
[74] A. Zharin, D.A. Rigney, Application of a contact potential difference technique for on-line rubbing surface monitoring (review), Tribol. Lett. 4 (1998) 205-213.
[75] D.Y. Li, W. Li, Electron work function: A parameter sensitive to the adhesion behavior of crystallographic surfaces, Appl Phys Lett 79 (2001) 4337-4338.
[76] W. Li, D.Y. Li, Effect of grain size on the electron work function of Cu and Al, Surf. Rev. Lett. 11 (2004) 173-178.
[77] W. Li, D.Y. Li, Characterization of interfacial bonding using a scanning Kelvin probe, J. Appl. Phys. 97 (2005) 7.
[78] B. Bhushan, A.V. Goldade, Kelvin probe microscopy measurements of surface potential change under wear at low loads, Wear 244 (2000) 104-117.
[79] B. Bhushan, A.V. Goldade, Measurements and analysis of surface potential change during wear of single-crystal silicon (100) at ultralow loads using Kelvin probe microscopy, Applied Surface Science 157 (2000) 373-381.
[80] I.D. Baikie, P.J. Estrup, Low cost PC based scanning Kelvin probe, Review of Scientific Instruments 69 (1998) 3902-3907.

[81] H.L. Skriver, N.M. Rosengaard, Surface-Energy and Work Function of Elemental Metals, Phys. Rev. B 46 (1992) 7157-7168.
[82] I.D. Baikie, P.J.S. Smith, D.M. Porterfield, P.J. Estrup, Multitip scanning bio-Kelvin probe, Review of Scientific Instruments 70 (1999) 1842-1850.
[83] N.A. Surplice, R.J. Darcy, A Critique of Kelvin Method of Measuring Work Functions, Journal of Physics E-Scientific Instruments 3 (1970) 477-482.
[84] http://www.rgu.ac.uk/
[85] D. DeVecchio, Using an atomic force microscope for mechanical and tribological proprties of thin films and surfaces, Master of Science, Materials science and engineering, The Ohio State of University, 1998.
[86] D. DeVecchio, B. Bhushan, Use of a nanoscale Kelvin probe for detecting wear precursors, Review of Scientific Instruments 69 (1998) 3618-3624.
[87] H.B. Michaelson, Work Functions of the Elements, J. Appl. Phys. 21 (1950) 536-540.
[88] H.B. Michaelson, Work Function of Elements and Its Periodicity, J. Appl. Phys. 48 (1977) 4729-4733.
[89] H.L. Skriver, N.M. Rosengaard, Abinitio Work Function of Elemental Metals, Phys. Rev. B 45 (1992) 9410-9412.
[90] S. Halas, 100 years of work function, Materials Science-Poland 24 (2006) 951-967.
[91] T. Durakiewicz, S. Halas, A. Arko, J.J. Joyce, D.P. Moore, Electronic work-function calculations of polycrystalline metal surfaces revisited, Phys. Rev. B 6404 (2001) 045101.
[92] S. Halas, T. Durakiewicz, Work functions of elements expressed in terms of the Fermi energy and the density of free electrons, Journal of Physics-Condensed Matter 10 (1998) 10815-10826.
[93] W. Li, D.Y. Li, Effects of dislocation on electron work function of metal surface, Mater. Sci. Technol. 18 (2002) 1057-1060.
[94] R.H. Baughman, J.M. Shacklette, A.A. Zakhidov, S. Stafstrom, Negative Poisson's ratios as a common feature of cubic metals, Nature 392 (1998) 362-365.
[95] A.R. Miedema, Electronegativity Parameter for Transition-Metals - Heat of Formation and Charge-Transfer in Alloys, Journal of the Less-Common Metals 32 (1973) 117-136.
[96] Chemical Rubber Company., Knovel (Firm), CRC handbook of chemistry and physics, in: (Knovel, Binghamton, N.Y., 2004).
[97] A.R. Miedema, R. Boom, Surface-Tension and Electron-Density of Pure Liquid-Metals, Z. Metallk. 69 (1978) 183-190.

[98] A.R. Miedema, R. Boom, F.R. Deboer, Heat of Formation of Solid Alloys, Journal of the Less-Common Metals 41 (1975) 283-298.
[99] A.R. Miedema, F.R. Deboer, P.F. Dechatel, Empirical Description of Role of Electronegativity in Alloy Formation, Journal of Physics F-Metal Physics 3 (1973) 1558-1576.
[100] S.N. Zadumkin, Shebuhkh.Ig, Alchagir.Bb, Surface-Energy and Work Function of Smooth Facets of a Metallic Single-Crystal, Physics of Metals and Metallography-Ussr 30 (1970) 195-198.
[101] K.K. Kalazhokov, A.S. Gonov, Z.K. Kalazhokov, On the calculation of the surface energy of a face of a single crystal through the electron work function of this face, Russian Metallurgy (1996) 39-41.
[102] W. Li, D.Y. Li, A simple method for determination of the electron work function of different crystallographic faces of copper, Phys. Status Solidi A-Appl. Res. 196 (2003) 390-395.
[103] P.H. Rieger, Electrochemistry, Chapman & Hall, New York, 1994.
[104] C.H. Hamann, A. Hamnett, W. Vielstich, Electrochemistry, Wiley-VCH, Weinheim ; New York 1998.
[105] J.O.M. Bockris, B.E. Conway, E. Yeager, Comprehensive treatise of electrochemisty, Vol. 1, Plenum Press, New York, 1980.
[106] D. Tsiplakides, C.G. Vayenas, The absolute potential scale in solid state electrochemistry, Solid State Ionics 152 (2002) 625-639.
[107] D. Tsiplakides, C.G. Vayenas, Electrode work function and absolute potential scale in solid-state electrochemistry, Journal of the Electrochemical Society 148 (2001) E189-E202.
[108] S. Trasatti, Structure of the Metal Electrolyte Solution Interface - New Data for Theory, Electrochimica Acta 36 (1991) 1657-1658.
[109] R.H. Bube, Electrons in solids: an introductory survey, Academic Press, Boston, 1992.
[110] L.H. Lee, Relevance of the Density-Functional Theory to Acid-Base Interactions and Adhesion in Solids, J. Adhes. Sci. Technol. 5 (1991) 71-92.
[111] W. Li, D.Y. Li, Exploring the application of the Kelvin method in studying the history prior to wear and the onset of wear, Wear 253 (2002) 746-751.
[112] A. Zharin, Technique of friction monitoring, J. Friction Wear 14 (1993) 111-120.

[113] A. Zharin, E.I. Fishbein, N.A. Shipitsa, Effect of contact deformation upon surface electron work function, J. Friction Wear 16 (1995) 66-78.
[114] A. Zharin, N.A. Shipitsa, E.I. Fishbein, Some features of fatigue at sliding friction, J. Friction Wear 14 (1993) 13-22.
[115] W. Li, D.Y. Li, Variations of work function and corrosion behaviors of deformed copper surfaces, Applied Surface Science 240 (2005) 388-395.
[116] X.Y. Wang, D.Y. Li, Mechanical and electrochemical behavior of nanocrystalline surface of 304 stainless steel, Electrochimica Acta 47 (2002) 3939-3947.
[117] X.Y. Wang, D.Y. Li, Beneficial effects of yttrium on the mechanial failure and chemical stability of the passive film of 304 stainless steel, Materials Sci. and Eng. A315 (2001) 158-165.
[118] W. Li, D.Y. Li, Determination of the yield locus using a Kelvin probing method, J. Phys. D-Appl. Phys. 37 (2004) 948-951.
[119] W. Li, Y. Wang, D.Y. Li, Response of the electron work function to deformation and yielding behavior of copper under different stress states, Phys. Status Solidi A-Appl. Res. 201 (2004) 2005-2012.
[120] T. Kasai, D.A. Rigney, A. Zharin, Changes detected by a non-contacting probe during sliding, Scripta Materialia 39 (1998) 561-567.
[121] A.L. Zharin, N.A. Shipitsa, D.I. Saroka, Effect of chemical and phase composition of sintered tin bronzes on fatigue failure with friction, Powder Metallurgy and Metal Ceramics 41 (2002) 29-35.
[122] A.L. Zharin, G.P. Shpenkov, Macroscopic Effects of Delamination Wear, Wear 56 (1979) 309-313.
[123] X.Y. Wang, D.Y. Li, Mechanical, electrochemical and tribological properties of nano-crystalline surface of 304 stainless steel, Wear 255 (2003) 836-845.
[124] D.Y. Li, Kelvin probing technique: A promising method for the determination of the yield strain of a solid under different types of stress, Phys. Status Solidi A-Appl. Res. 191 (2002) 427-434.
[125] D.Y. Li, L. Wang, W. Li, Effects of grain size from micro scale to nanoscales on the yield strain of brass under compressive and tensile stresses using a Kelvin probing technique, Mater. Sci. Eng. A-Struct. Mater. Prop. Microstruct. Process. 384 (2004) 355-360.

[126] W. Li, D.Y. Li, Effects of elastic and plastic deformations on the electron work function of metals during bending tests, Philosophical Magazine 84 (2004) 3717-3727.
[127] Y. Li, D.Y. Li, Experimental studies on relationships between the electron work function, adhesion, and friction for 3d transition metals, J. Appl. Phys. 95 (2004) 7961-7965.
[128] O. Vatel, M. Tanimoto, Kelvin Probe Force Microscopy for Potential Distribution Measurement of Semiconductor-Devices, J. Appl. Phys. 77 (1995) 2358-2362.
[129] W.A. Glaeser, Materials for tribology, Elsevier Science, Amsterdam ; New York, 1992.
[130] Hochstra.R.M., Energies of Electronic Configurations of Transition Metals, J. Chem. Educ. 42 (1965) 154-156.
[131] K. Miyoshi, D.H. Buckley, Adhesion and Friction of Single-Crystal Diamond in Contact with Transition-Metals, Applied Surface Science 6 (1980) 161-172.
[132] K.F. Purcell, J.C. Kotz, Inorganic chemistry, Saunders, Philadelphia, 1977.
[133] Y. Li, D.Y. Li, Prediction of elastic-contact friction of transition metals under light loads based on their electron work functions, J. Phys. D-Appl. Phys. 40 (2007) 5980-5983.
[134] B. Bhushan, Nanoscale tribophysics and tribomechanics, Wear 229 (1999) 465-492.
[135] AFM/LFM Instruction Manual(Digital Instrument), in: (Santa Barbara, 1999).
[136] Instruments for coating thickness measurement and materials testing,Fischerscope H100C, in: (Windsor, 2000).
[137] I. Radu, D.Y. Li, R. Llewellyn, Tribological behavior of Stellite 21 modified with yttrium, Wear 257 (2004) 1154-1166.
[138] S.A. Shahdad, J.F. McCabe, S. Bull, S. Rusby, R.W. Wassell, Hardness measured with traditional Vickers and Martens hardness methods, Dental Materials 23 (2007) 1079-1085.
[139] M. Weinert, R.E. Watson, Contributions to the Work Function of Crystals, Phys. Rev. B 29 (1984) 3001-3008.
[140] D.H. Buckley, K. Miyoshi, Friction and Wear of Ceramics, Wear 100 (1984) 333-353.
[141] V.N. Koinkar, B. Bhushan, Effect of scan size and surface roughness on microscale friction measurements, J. Appl. Phys. 81 (1997) 2472-2479.
[142] J.A. Ruan, B. Bhushan, Atomic-Scale and Microscale Friction Studies of Graphite and Diamond Using Friction Force Microscopy, J. Appl. Phys. 76 (1994) 5022-5035.

[143] S. Sundararajan, B. Bhushan, Topography-induced contributions to friction forces measured using an atomic force/friction force microscope, J. Appl. Phys. 88 (2000) 4825-4831.
[144] U.D. Schwarz, O. Zworner, P. Koster, R. Wiesendanger, Quantitative analysis of the frictional properties of solid materials at low loads .1. Carbon compounds, Phys. Rev. B 56 (1997) 6987-6996.
[145] E. Liu, B. Blanpain, J.P. Celis, J.R. Roos, Comparative study between macrotribology and nanotribology, J. Appl. Phys. 84 (1998) 4859-4865.
[146] R. Prioli, D.C. Reigada, F.L. Freire, Nanoscale friction and wear mechanisms at the interface between a boron carbide film and an atomic force microscope tip, J. Appl. Phys. 87 (2000) 1118-1122.
[147] Y. Li, D.Y. Li, Electron work function, adhesion, and friction between 3d transition metals under light loads, Wear 259 (2005) 1432-1436.
[148] J. Ferrante, J.R. Smith, Theory of Adhesion at a Bimetallic Interface - Overlap Effects, Surf. Sci. 38 (1973) 77-92.
[149] A. Yaniv, Electronic Properties of a Simple Metal-Metal Interface, Phys. Rev. B 17 (1978) 3904-3918.
[150] W.R. Chang, I. Etsion, D.B. Bogy, Static Friction Coefficient Model for Metallic Rough Surfaces, J Tribol-T Asme 110 (1988) 57-63.
[151] Y. Li, D.Y. Li, An energy consumption model based on the electron work function and Fermi energy for predicting adhesion and low-load friction between 3d transition metals, Wear 263 (2007) 1610-1615.
[152] D.V. Keller, Adhesion between solid metals, Wear 6 (1963) 353-365.
[153] K. Miyoshi, Adhesion, friction, and wear behavior of clean metal-ceramic couples, NASA Technical Memorandum 106815 (1995) 1-6.
[154] N. Martensson, A. Stenborg, O. Bjorneholm, A. Nilsson, J.N. Andersen, Quantitative Studies of Metal-Metal Adhesion and Interface Segregation Energies Using Photoelectron-Spectroscopy, Phys. Rev. Lett. 60 (1988) 1731-1734.
[155] F.R. Deboer, R. Boom, W.C.M. Mattens, A.R. Miedema, Cohesion in Metals, North-Holland Physics Publishing, The Netherlands, 1988.

[156] F. Gautier, A.M. Llois, Adhesion of Transition-Metals - Energies and Thin-Film Deposition - an Electronic Approach, Surf. Sci. 245 (1991) 191-206.
[157] R.B. Roos, Metallic materials specification handbok, E. & F. N. Spon., London, 1980.
[158] N. Gane, P.F. Pfaelzer, D. Tabor, Adhesion between Clean Surfaces at Light Loads, Proc. R. Soc. London Ser. A-Math. Phys. Eng. Sci. 340 (1974) 495-&.
[159] R.W. Carpick, D.F. Ogletree, M. Salmeron, A general equation for fitting contact area and friction vs load measurements, J Colloid Interf Sci 211 (1999) 395-400.
[160] G. Allan, Tight-Binding Methods as Applied to Transition-Metal Surfaces, Surf. Sci. 300 (1994) 319-331.
[161] W.A. Goddard, Handbook of nanoscience, engineering, and technology, CRC Press, Boca Raton, FL, 2007.
[162] V. Stolojan, Nanochemistry of grain boundaries in Iron, Doctor of Philosophy, University of Cambridge, 2000.
[163] A.W. Adamson, A.P. Gast, Physical chemistry of surfaces, Wiley, New York, 1997.
[164] K.X. Ma, C.H. Ho, F.R. Zhu, T.S. Chung, Investigation of surface energy for organic light emitting polymers and indium tin oxide, Thin Solid Films 371 (2000) 140-147.
[165] http://en.wikipedia.org/wiki/Hubbard_model.
[166] Z. Xu, Elastic theory, Education Press, Beijing, 1988.
[167] J.O. Smith, C.K. Liu, Stresses due to tangential and normal loads on an elastic solid with application to some contact stress problems, J. Appl. Mechanics-Transactions of the Asme 20 (1953) 157-166.
[168] www.webelements.com
[169] S. Harinipriya, M.V. Sangaranarayanan, Hardness of metals from electron transfer reactions at electrode surfaces, J. Chem. Phys. 117 (2002) 8959-8965.
[170] W. Li, D.Y. Li, A study on the kinetic response of the electron work function to wear, Wear 255 (2003) 333-340.
[171] A. Buch, Some relations between elastic and physical parameters of pure metals, Materialprufung 48 (2006) 286-288.
[172] H.M. Lee, W.J. Lee, Poisson Ratio of Pure Metals and Their Nonmetallic Compounds, Scripta Metallurgica Et Materialia 25 (1991) 965-968.
[173] L. Louail, D. Maouche, A. Roumili, F.A. Sahraoui, Calculation of elastic constants of 4d transition metals, Materials Letters 58 (2004) 2975-2978.

[174] M. Brajczewska, C. Henriques, C. Fiolhais, Dependence of metal surface properties on the valence-electron density in the stabilized jellium model, Vacuum 63 (2001) 135-138.
[175] U. Lundin, L. Fast, L. Nordstrom, B. Johansson, J.M. Wills, O. Eriksson, Transition-metal dioxides with a bulk modulus comparable to diamond, Phys. Rev. B 57 (1998) 4979-4982.
[176] R.G. Pearson, Maximum chemical and physical hardness, J. Chem. Educ. 76 (1999) 267-275.
[177] S.H. Jhi, J. Ihm, S.G. Louie, M.L. Cohen, Electronic mechanism of hardness enhancement in transition-metal carbonitrides, Nature 399 (1999) 132-134.
[178] M. Gajdos, A. Eichler, J. Hafner, Ab initio density functional study of O on the Ag(001) surface, Surf. Sci. 531 (2003) 272-286.
[179] A.A. Knizhnik, I.M. Iskandarova, A.A. Bagatur'yants, B.V. Potapkin, L.R.C. Fonseca, Impact of oxygen on the work functions of Mo in vacuum and on ZrO2, J. Appl. Phys. 97 (2005) 064911.
[180] S.Y. Liu, F.H. Wang, Y.S. Zhou, J.X. Shang, Ab initio study of oxygen adsorption on the Ti(0001) surface, Journal of Physics-Condensed Matter 19 (2007) 226004.
[181] I. Merrick, J.E. Inglesfield, H. Ishida, Electronic structure and surface reconstruction of adsorbed oxygen on copper(001), Surf. Sci. 551 (2004) 158-170.
[182] Y. Makino, S. Miyake, Estimation of bulk moduli of compounds by empirical relations between bulk modulus and interatomic distance, Journal of Alloys and Compounds 313 (2000) 235-241.
[183] Y. Makino, Empirical determination of bulk moduli of elemental substances by pseudopotential radius, Journal of Alloys and Compounds 242 (1996) 122-128.
[184] G.Y. Guo, H.H. Wang, Gradient-corrected density functional calculation of elastic constants of Fe, Co and Ni in bcc, fcc and hcp structures, Chinese Journal of Physics 38 (2000) 949-961.
[185] C.B. Li, M.K. Li, D. Yin, F.Q. Liu, X.J. Fan, First principles study on the charge density and the bulk modulus of the transition metals and their carbides and nitrides, Chinese Physics 14 (2005) 2287-2292.
[186] A. Mahmood, L.E. Sansores, J. Heiras, Bulk modulus calculations for group-IV carbides and group-III nitrides, Modern Physics Letters B 18 (2004) 1247-1254.

[187] Y. Song, R. Yang, D. Li, W.T. Wu, Z.X. Guo, Calculation of theoretical strengths and bulk moduli of bcc metals, Phys. Rev. B 59 (1999) 14220-14225.
[188] A. Kiejna, Stabilized jellium - simple model for simple-metal surfaces, Progress in Surface Science 61 (1999) 85-125.
[189] F. Perrot, M. Rasolt, A New Listing of the Effective R(S) Values for Metals, Journal of Physics-Condensed Matter 6 (1994) 1473-1482.
[190] W.D. Callister, Materials science and engineering: an introduction, John Wiley & Sons, New York, 2007.